



F-16 VENTRAL FIN BUFFET ALLEVIATION
USING PIEZOELECTRIC ACTUATORS

THESIS

Joseph S. Browning, Captain, USAF

AFIT/GAE/ENY/09-S01

DEPARTMENT OF THE AIR FORCE
AIR UNIVERSITY

AIR FORCE INSTITUTE OF TECHNOLOGY

Wright-Patterson Air Force Base, Ohio

APPROVED FOR PUBLIC RELEASE; DISTRIBUTION UNLIMITED.

Research sponsored in part by the United States Air Force Test Pilot School, Edwards Air Force Base, California. The United States Government is authorized to reproduce and distribute reprints notwithstanding any copyright notation thereon. The views expressed in this thesis are those of the author and do not reflect the official policy or position of the United States Air Force, Department of Defense, or the United States Government.

AFIT/GAE/ENY/09-S01

F-16 VENTRAL FIN BUFFET ALLEVIATION
USING PIEZOELECTRIC ACTUATORS

THESIS

Presented to the Faculty

Department of Aeronautics and Astronautics

Graduate School of Engineering and Management

Air Force Institute of Technology

Air University

Air Education and Training Command

In Partial Fulfillment of the Requirements for the
Degree of Master of Science in Aeronautical Engineering

Joseph S. Browning, B.S.M.E.

Captain, USAF

September 2009

APPROVED FOR PUBLIC RELEASE; DISTRIBUTION UNLIMITED.

F-16 VENTRAL FIN BUFFET ALLEVIATION
USING PIEZOELECTRIC ACTUATORS

Joseph S. Browning, B.S.M.E.
Captain, USAF

Approved:

Dr. Robert A. Canfield, (Chairman)

date

Dr. Richard G. Cobb, (Co-Chairmen)

date

LtCol. Christopher M. Shearer, PhD.
(Member)

date

Abstract

Buffet-induced vibrations can have a disastrous impact on aircraft structures. Early attempts at combating buffet vibrations included passive methods such as structural enhancements and leading edge fences used to minimize the strength of vortices. Active methods, however, have shown greater promise, including active airflow control, control surface modulation, and control systems employing piezoelectric actuators, the latter drawing much attention in recent years. Piezoelectric actuators, when mounted to the surface of the affected structure, impart directional strain reducing the negative effects associated with harmful vibration. The Block-15 F-16 ventral fin represents an aircraft structure prone to failure when subjected to the buffet field from the wake of a Low Altitude Navigation and Targeting Infrared for Night (LANTIRN) pod. However, ventral fin failures pose relatively little risk to the pilot or the aircraft within the nominal F-16 flight envelope, highlighting its potential as a platform for further investigation into the effectiveness of piezoelectric actuators. This research takes advantage of the susceptibility to buffet vibration of the Block 15 ventral fin as the subject of an effort to design an active control system to alleviate vibrations using piezoelectric actuators and sensors and to demonstrate its capability during flight test. The research was sponsored by the United States Air Force (USAF) Test Pilot School (TPS).

The development of an active control system began with the specification of piezoelectric actuators and sensors to be used in a collocated design to alleviate the vibrations of the first two modes of the ventral fin. A switching amplifier was designed and custom built to drive the actuators during all phases of testing. For the piezoelectric actuators to be effective, they needed to be located within the regions of highest strain energy and aligned with the principal strain vectors in those regions, the direction of principle strain was experimentally determined to ensure the proper

orientation of the piezoelectric hardware on the ventral fin's surface. Two control techniques were used in this research: positive position feedback and Linear Quadratic Gaussian compensator. Both algorithms were developed and optimized during laboratory simulations and bench testing with system hardware where as much as 15 dB peak magnitude reduction was achieved in the ventral fin mode 1, 2, and 3 response. The positive position feedback algorithms were implemented during aircraft ground and flight testing at the USAF TPS, Edwards Air Force Base, California. Ground testing showed as much as 14 dB and 8 dB peak magnitude reduction in the mode 2 and mode 3 response, respectively. As much as 4 dB peak magnitude reduction was recorded in the mode 2 response during flight testing proving the potential of piezoelectric actuators in a buffet alleviation system. Still, there exists many design considerations, such as piezoelectric actuator and sensor configuration, that could lead to system improvement.

Acknowledgements

This thesis has been the most demanding academic endeavor I have ever undertaken. Taking the initial concept of this research to flight test in only 18 months could not have been done with the support of many people. I would like to thank Dr. Bob Canfield who first intrigued me with this thesis and guided me to its completion, Dr Richard Cobb for his invaluable expertise in vibration control and tireless support through many grueling hours in the lab, and Mr Sean Miller of AFIT without whose resourcefulness and dedication the amplifier assembly would not have been built and the ground and flight testing would not have been realized. I would also like to thank Mr. Thomas Daue of the Smart Material Corp. for his guidance in the design of piezoelectric actuators and sensors and Maj Seo Yow Teo, Capt Chris Seager, Capt Lane Haubelt, and Capt Chris Buckely, the ACTIVE FIN flight test team at the USAF Test Pilot School, whose dedication saw the successful completion of the flight test portion of this research.

To My Parents

Thank you very much for your continual love and encouragement during the 15 months I was at AFIT and throughout the challenging year at TPS. Without you, I simply would not be who and where I am today.

Joseph S. Browning

Table of Contents

	Page
Abstract	iv
Acknowledgements	vi
List of Figures	ix
List of Tables	xii
List of Symbols	xiii
List of Abbreviations	xiv
I. Introduction	1
1.1 Problem/Scope	5
1.2 Approach/Methodology	6
II. Literature Review	8
2.1 History of the Buffet-Induced Vibration Problem	8
2.2 Piezoelectricity and its Application to Buffet Alleviation	10
2.3 Control Methodologies in Buffet Alleviation	16
2.3.1 Sensor Selection and Location	18
2.3.2 Control Methods	22
2.4 Drive Amplifier	24
III. Theoretical Background	27
3.1 Piezoelectric Actuator Placement, Sizing, and Orientation	27
3.1.1 Experimental Determination of Principle Strain Vectors	28
3.2 Piezoelectric Sensor Placement and Orientation	32
3.3 System Model Identification	33
3.4 Control Algorithm Development	35
3.4.1 Positive Position Feedback	36
3.4.2 Linear Quadratic Gaussian	39
3.4.3 Closed-Loop Stability	44
3.5 Implementation of Control Algorithms in Software	45

	Page
IV. Methodolgy	49
4.1 Piezoelectric Actuator and Sensor Design	49
4.1.1 Mode Selection	49
4.1.2 Actuator Design	50
4.2 Natural Frequency and Mode Shape Verification	53
4.3 Experimental Determination of the Principle Strain Vectors	54
4.4 Piezoelectric Actuators and Sensors Installation	56
4.5 Drive Amplifier Design	57
4.6 Transfer Function Model Realization	62
4.7 Closed-Loop Control Development and Optimization	65
4.7.1 Positive Position Feedback	66
4.7.2 Linear Quadratic Gaussian	67
4.7.3 Digital Implementation	68
4.8 Aircraft Installation and Ground Testing	69
4.9 ACTIVE FIN Flight Testing	72
V. Results and Analysis	76
5.1 Laboratory Simulations and Bench Testing	76
5.1.1 Positive Position Feedback	76
5.1.2 Linear Quadratic Gaussian	78
5.2 Aircraft Ground Testing	84
5.3 ACTIVE FIN Flight Testing	86
VI. Summary and Conclusions	94
6.1 Summary	94
6.2 Recommendations	97
Bibliography	100
Vita	105

List of Figures

Figure		Page
1.1.	LANTIRN Pod and Ventral Fin Locations [courtesy USAF] . . .	2
1.2.	Ventral Fin Failure Example [courtesy USAF]	3
2.1.	Comparison of Isotropic and Orthotropic Actuators [6]	12
2.2.	Modal Modification and Addition Techniques [1]	16
2.3.	Major Components of the F/A-18 BLA System [38]	19
2.4.	Affect of Pole-Zero Flipping on System Stability [40]	20
2.5.	Basic Design of a Piezo Switching Amplifier [10]	26
3.1.	Mode 1 (78 Hz) Strain Energy Plot and Recommended Patch Location [7]	28
3.2.	Mode 2 (96 Hz) Strain Energy Plot and Recommended Patch Location [7]	29
3.3.	Mode 1 (78 Hz) Principle Strain Vector Orientation and Recom- mended Patch Location [7]	29
3.4.	Mode 2 (96 Hz) Principle Strain Vector Orientation and Recom- mended Patch Location [7]	30
3.5.	Curvature Example	31
3.6.	Strain Rosette from Laser Vibrometer Scan Grid Points	31
3.7.	Simple Block Diagram	35
3.8.	Bode Plot for PPF of Various Damping Ratios	39
3.9.	LQG Control Block Diagram [5]	40
3.10.	Stability Margins from a Nichols Chart /citeogata.	45
3.11.	Compact RIO Control Unit Hardware Components	47
3.12.	Compact RIO Control Unit Block Diagram	47
4.1.	Mode 4 (233 Hz) Strain Energy Plot and Suggested Patch Loca- tion [7]	51
4.2.	Piezoelectric Actuator, Design 1	51

Figure		Page
4.3.	Piezoelectric Actuator, Design 2 (with embedded sensor)	51
4.4.	Piezoelectric Actuator Orientation on the Ventral Fin.	53
4.5.	Laser Vibrometer Scan Pattern	56
4.6.	Principle Strain Vector Fields	56
4.7.	Piezoelectric Patch Installation Using Surface Vacuum Bagging	57
4.8.	Piezoelectric Patches Installed on the Ventral Fin, AFIT Laboratory	58
4.9.	Piezoelectric Drive Amplifier Schematic (Simplified)	60
4.10.	Piezoelectric Drive Amplifier Transfer Function	60
4.11.	Bit-Selectable Adjustable Attenuation Circuit	61
4.12.	Amplifier Assembly	62
4.13.	System Block Diagram	63
4.14.	Open-Loop Block Diagram	63
4.15.	Forward Array Open-Loop Frequency Response, AFIT Laboratory	64
4.16.	Aft Array Open-Loop Frequency Response, AFIT Laboratory	64
4.17.	Experimental and ERA Model Transfer Function Comparison, Aft Array	65
4.18.	Bench Test Setup for Closed-Loop Performance, AFIT Laboratory	66
4.19.	Full-State vs. Reduced-State LQG Compensator	69
4.20.	Instrumented Ventral Fin Installed on the Test Aircraft, Edwards AFB	70
4.21.	System Hardware Installed in the Ammo Bay of the Test Aircraft, Edwards AFB	71
4.22.	OQO Handheld PC Mounted in Rear Cockpit, Edwards AFB .	71
4.23.	Test Aircraft System Diagram	72
4.24.	ACTIVE FIN Test Point Matrix [4]	73
4.25.	Flight Test Configuration, Edwards AFB	75

Figure		Page
5.1.	PPF Bench Test Results	79
5.2.	LQG Bench Test Results	79
5.3.	Forward Array PPF Design	80
5.4.	Aft Array PPF Design	80
5.5.	Forward Array LQG Design	81
5.6.	Aft Array LQG Design	81
5.7.	Forward Array Frequency Response, Ground Testing	84
5.8.	Aft Array Frequency Response, Ground Testing	85
5.9.	Forward Array Closed-Loop Response, Ground Testing	85
5.10.	Aft Array Closed-Loop Response, Ground Testing	86
5.11.	Sensor Voltage Level Comparison	88
5.12.	Flight Test Frequency Response, 10,000 feet Pressure Altitude, 0.90 Mach [4]	89
5.13.	Flight Test Mode 2 Peak Magnitude Response, 10,000 feet Pres- sure Altitude, Transonic [4]	89
5.14.	Flight Test Frequency Response, Powered Approach Configura- tion, 15,000 feet Pressure Altitude [4]	90
5.15.	Sensor and Amplifier Output Voltage, Flight Test, 15,000 feet, 0.30 Mach, 1g Level Flight, Powered Approach	92
5.16.	Sensor and Amplifier Output Voltage, Flight Test, 7,500 feet, 0.95 Mach, 1g Level Flight	92
5.17.	Amplifier Output Simulation Using Flight Test Sensor Input (7,500 feet, 0.95 Mach, 1g Level Flight) and Amplifier Transfer Function Model (Figure 4.10)	93

List of Tables

Table		Page
4.1.	Block 15 F-16 Ventral Fin Historical Modal Frequencies [7] . . .	50
4.2.	Piezoelectric Actuator/Sensor Specifications ¹	52
4.3.	Ventral Fin Test Article Natural Frequency Comparison	54
4.4.	Ventral Fin Mode Shapes	55
4.5.	Piezoelectric Sensor Output Configuration	61
4.6.	Frequency Spectrum Estimation Parameters	75
5.1.	Positive Position Feedback Laboratory Optimization	82
5.2.	Linear Quadratic Gaussian Laboratory Optimization	83
5.3.	Ventral Fin Natural Frequency Comparison [4]	87
6.1.	Summary of Test Results	96

List of Symbols

Symbol		Page
d_{33}	Transverse Piezoelectric Charge Constant	27
ε_1	Principle Strain	31
θ	Principle Strain Direction	32
Q	Charge	32
T	Stress	32
C	Capacitance	32
ε_{33}	Dielectric Permittivity	32
E	Young's Modulus	32
\mathcal{R}	Radius of Curvature	32
H	Hankel Matrix	34
$P(s)$	Plant Transfer Function	35
$G(s)$	Compensator Transfer Function	35
ω_n	Natural Frequency	36
ω_c	Compensator Frequency	36
ζ_n	Damping Ratio	36
ζ_c	Compensator Damping Ratio	36
g	Scalar Gain	36
ϕ	Phase Angle	37
K	Feedback Gain Matrix	41
Q	State Weighting Matrix	41
R	Control Penalty Matrix	41
P	Matrix of Proportionality	42
v	Voltage	50
q_n	State Weighting Constant	68
r	Control Penalty Constant	68

List of Abbreviations

Abbreviation		Page
USAF	United States Air Force	iv
TPS	Test Pilot School	iv
LANTIRN	Low Altitude Navigation and Targeting Infrared for Night	2
USAF	United States Air Force	3
BLA	Buffet Load Alleviation	4
ACROBAT	Actively Controlled Response of Buffet-Affected Tails	4
ASE	Aero-servoelastic	4
TPS	Test Pilot School	7
PZT	Lead Zirconate Titanate	12
PVDF	Polyvinylidene Fluoride	12
MFC	Macro-Fiber Composite	14
mm	millimeter	15
Hz	Hertz	15
SISO	Single-Input Single-Output	16
LQG	Linear Quadratic Gaussian	22
dB	Decibel	23
PSD	Power Spectral Density	23
PPF	Positive Position Feedback	23
IGBT	Isolated Gate Bipolar Transistors	25
mA	milliamps	25
uF	micro-Farad	26
FEM	Finite Element Model	27
ERA	Eigensystem Realization Algorithm	33
RMS	Root Mean Square	35
LQR	Linear Quadratic Regulator	39

Abbreviation		Page
cRIO	Compact Reconfigurable Input-Output	46
A/D	Analog-to-Digital	46
D/A	Digital-to-Analog	46
FPGA	Field Programmable Gate Array	48
PWM	Pulse Width Modulation	58
kHz	Kilohertz	58
EMI	Electromagnetic Interference	58
G	Load Factor	58
AFB	Air Force Base	69
DAS	Data Acquisition System	70
OQO	Hand-held personal computer model name	70
AOA	Angle of Attack	73
PA	Powered-Approach (landing gear down at approach speed)	87
KCAS	Knots Calibrated Airspeed	88

F-16 VENTRAL FIN BUFFET ALLEVIATION USING PIEZOELECTRIC ACTUATORS

I. Introduction

Active control of structural vibrations, a well explored topic in recent years, has seen application with flexible spacecraft structures [21], helicopter airframes [12], and even downhill skis [15] with some success. However, the challenge of suppressing structural vibrations in modern high performance aircraft has proven difficult for some time. The capability of modern fighter aircraft to sustain flight at high speeds, high angles of attack, and/or moderate angles of side slip often results in unsteady, vortical flow around parts of the aircraft's body. In most cases, this flow contains significant levels of energy over a frequency bandwidth common with structural vibration modes of wings, fins, and other surfaces [6]. The resulting unsteady pressures developed on these surfaces is referred to as buffet. Early fatigue and the generation of cracks result from prolonged exposure to buffeting. In order to sustain operational readiness of affected aircraft, resources must be spent analyzing, repairing, maintaining, and in some cases redesigning structures susceptible to buffet damage.

The most notable cases of buffet-induced vibration problems on high performance aircraft have been with twin-tailed aircraft such as the F-15, F/A-18, and F-22. Buffet loads imposed upon the vertical tails of the F/A-18, for example, led to premature failure of the tail assemblies which not only increased inspection and maintenance costs, but limited the operational capabilities of the aircraft when maneuvering at high angles of attack [45]. A study of F-15 vertical tail failures discovered that fatigue cracking caused by buffet induced vibrations led to undue moisture absorption and corrosion. As with the F/A-18 tails, F-15 buffet problems restricted mission availability and flight maneuvering at high angles of attack. Hanagud perceived an increase in maintenance costs in USAF F-15 operations by as much as \$5-6M per year [22].



Figure 1.1: LANTIRN Pod and Ventral Fin Locations [courtesy USAF]

Buffet induced vibrations affect more than just vertical tail assemblies. The ventral fin of the F-16 provides an example of an aircraft structure that suffers from this phenomenon. A pair of ventral fins, located on the underside of the fuselage forward of the jet exhaust nozzle as shown in Figure 1.1, were designed to provide enhanced lateral stability during supersonic flight. During early flights of the first F-16 production models (prior to Block 30 variants), the aircraft experienced partial or total ventral fin loss. In early investigations it was determined that credible analysis could not be achieved unless turbulence effects were accurately considered [51]. As a consequence, the main suspect to the failures was turbulence due to abrupt throttle retardations which induce spillage of air from the engine inlet creating oscillatory stress cycles on the ventral fin [51]. Furthermore, these stress cycles were found to be dependent on centerline store configurations. The introduction of the LANTIRN pod, mounted aft of the engine inlet and offset from the aircraft centerline aligned



Figure 1.2: Ventral Fin Failure Example [courtesy USAF]

with the ventral fins as shown in Figure 1.1, saw an increase in fin failures. Figure 1.2 shows a ventral fin failure following a flight with the LANTIRN pod.

Past attempts to solve buffet-induced vibration problems on various aircraft employed techniques that either altered the airflow around the structure or altered the structure itself. The former had been achieved by controlling blowing or sucking flow from ports on the aircraft's surface or by intruding an obstacle in the flow such as a leading edge extensions or fences [36]. Flow control techniques have seen limited success since these methods target only specific flight conditions. Passive methods, such as altering structural properties like damping or stiffness, have been more successful, but not without a price. Structural changes increase aircraft weight and some modifications can actually transfer damaging loads to weaker structural members.

Similar tactics have been applied to the F-16 ventral fin problem. Project HAVE PUFF at the Air Force Flight Test Center used synthetic jet actuators mounted inside a modified LANTIRN pod to disrupt the air flow around the pod. Unfortunately, testing concluded the synthetic jets had an insignificant affect on strain and pressure measured on the ventral fin [34]. The solution to ventral fin buffet adopted by the United States Air Force (USAF) in order to satisfy ventral fin life cycle requirements included several structural modifications implemented on Block 30 and later models of the F-16 [51]. Active control, however, presents an opportunity to arrive at the

same result by a potentially lighter and more efficient means. In fact, recent and ongoing research have explored various active control methods to help alleviate buffet vibrations on many different aircraft. Piezoelectric actuators, in particular, have shown great promise in the active control of buffet vibrations [22, 36, 45].

Significant research, accomplished by the multinational F/A-18 Buffet Load Alleviation (BLA) program, investigated multiple techniques in alleviating buffet loads on the aircraft's vertical tails including the use of piezoelectric actuators. Lazarus, Saarmaa, and Agnes [29] developed an analytical model using distributed, layered piezoelectric actuators bonded to the F/A-18 vertical tail that indicated a 50% reduction in the root-mean-square strain at the root of the tail during simulated flight conditions. Moses investigated active control on a 1/6-scale F/A-18 model in a wind tunnel as part of the Actively Controlled Response Of Buffet-Affected Tails (ACRO-BAT) program and found a reduction of root-mean-square values of tail root strain by as much as 19% [35].

Despite the promise of piezoelectric actuators, the active control of buffet vibrations using piezoelectric actuators has not been tested on actual aircraft structures beyond the wind tunnel. At the time of print, the only flight-demonstrated effort to employ piezoelectrics for the suppression of vibrations on an aircraft structure was that of the Air Force Research Laboratory in the suppression of acoustic vibrations on a skin panel of the B-1 aircraft [18]. The F-16 ventral fin presents an excellent test structure for research of active control in actual flight conditions. Fortunately, ventral fin damage does not affect flight safety for subsonic flight. In fact, during past cases, the pilot had no indication of fin failure during nominal flight conditions.

Captain Shawn Morgenstern began research [7] for the application of piezoelectric actuators to actively control buffet vibrations on the F-16 ventral fin in 2006. Using finite element and aero-servoelastic (ASE) analysis, Morgenstern arrived at design recommendations for piezoelectric actuators based on strain energy density and principle strain vectors for an optimized model. He used the ZAERO [54] ASE

software module and flight test data [34] to analyze the first six modes of vibration and highlighted the first, second, and fourth modes as the most critical to ventral fin failure. What remained was the implementation of Morgenstern's design recommendations and the development of a suitable autonomous control system to determine the effectiveness of piezoelectric actuators to alleviate buffet induced vibrations on the ventral fin

1.1 Problem/Scope

The research problem presented in this thesis was the development of an autonomous active control system using collocated piezoelectric actuators and sensors to alleviate the buffet response of the first and second vibration modes of an F-16 Block 15 ventral fin during ground and flight tests. It is important to note that this research is not to mitigate the failure of Block 15 ventral fins, but takes advantage of the susceptibility of Block 15 ventral fins to aerodynamic buffet in order to evaluate the effectiveness of closed-loop control of piezoelectric actuators.

The scope of this research included (a) the specification of piezoelectric actuators and sensors as elements in the active control system, (b) an investigation of the techniques used to define the frequency response of the ventral fin and its translation to the state-space, (c) the development of a closed-loop control algorithm using collocated piezoelectric actuators and sensors, and (d) the integration of the control system, including controller hardware, custom designed switching amplifiers, and user interfaces, onto an F-16 aircraft for flight evaluation. The two control algorithms explored were positive position feedback and Linear Quadratic Gaussian compensator designs. These algorithms were implemented in independent single-input single-output modal control schemes. In order to demonstrate the system in flight, an appropriate power amplifier capable of driving the capacitive load of piezoelectric actuators at high voltage was designed and built. Other hardware components used in the flight demonstration, such as the cockpit user interface and digital controller, were specified and purchased commercial-off-the-shelf.

This thesis is organized as follows. Chapter II presents the history of buffet-induced vibrations with emphasis on active control methods used to combat the problem. The development of piezoelectric actuators and their inclusion in closed-loop control is also explored, followed by a brief discussion on the importance of the power amplifier design and integration onto military aircraft. Chapter III provides an in-depth look at controller design used in this research, including stability and performance criteria, for active control using piezoelectric elements. The application of the eigensystem realization algorithm in development of a mathematical model of the fin and its relevance to controller development is also discussed. Chapter IV describes the practical design and specification of piezoelectric actuators and their placement on an actual ventral fin and the development of a customized switching amplifier. Chapter IV also summarizes the specification of hardware to be used during flight test of the active control system, including the digital controller, input/output modules, signal conditioners, and power supply. The last portion of Chapter IV introduces laboratory, ground, and flight test activities performed on an actual ventral fin with installed piezoelectric elements. Chapter V presents results from the ground and flight test portions of the project. Chapter VI summarizes the effort and lists several recommendations for future work.

1.2 Approach/Methodology

Seven distinct tasks were completed in the course of this research. First, Morgenstern's design recommendations [7] for piezoelectric actuators were applied in the specification of appropriate sensors and actuators for the ventral fin. Several deviations were necessary, including individual actuator size and orientation and the selection of piezoelectric feedback sensors versus acceleration feedback, to tailor the piezoelectric elements for practical application on the ventral fin. Second, a switching amplifier capable of supporting the unique reactive load of piezoelectric actuators was designed and built. Third, before being instrumented with piezoelectric hardware, the ventral fin was analyzed to verify principle strain directions and modal parameters.

Fourth, a National Instruments Inc. digital controller was programmed using the LabVIEWTM software package to implement control algorithms, cockpit user interfaces, and data recording functions for ground and flight test activities. Fifth, the entire control system, including controller hardware, switching amplifier, and ventral fin instrumented with all piezoelectric hardware was tested in the laboratory to verify total control system performance and stability. Finally, the control system was installed on a F-16, ground and flight tested, and critiqued by the USAF Test Pilot School (TPS), Class 08B.

II. Literature Review

The harmful impact of the aeroelastic phenomenon known as buffet on military aircraft is well documented [7, 14, 22, 35, 51]. Technology and techniques employed to prevent it have been equally extensive [1, 6, 29, 34, 36, 38, 45]. The following review discusses the history of the buffet problem of military aircraft and presents the applicability of piezoelectrics for an active control solution. An introduction to piezoelectric actuator development and research towards buffet vibration control is provided. Active control system design considerations, including control algorithm techniques and power amplifier design given the unique environment of military aircraft, are also explored.

2.1 History of the Buffet-Induced Vibration Problem

In order to carry out various missions, military aircraft are forced to operate in harsh environments within large flight envelopes. High performance fighter aircraft, in particular, operate regularly in multi-role missions that require high-g and high speed maneuverability. Moreover, today's militaries are often forced to use aging aircraft in growing roles relying on structural or aerodynamic modifications to meet new mission requirements. Operating in extreme conditions at such high performance with multiple modifications produces an ideal environment for the damaging effect of the aerodynamic problem known as buffet [14]. Buffet "occurs when turbulent airflow interacts with an aerodynamic structure, exciting the vibrational modes of that structure" [7]. Severe buffet often results in large amplitude vibrations that can severely damage the structure or limit its useful life.

The most notable cases of aerodynamic buffet in military aircraft is that which plague the vertical tails of high performance twin tailed aircraft such as the F-15, F/A-18 and F-22. The F-15 vertical tails have undergone three major redesigns in an effort to prevent fatigue cracking that was discovered only a year after its operational debut. Each design change was aimed at modifying stiffness properties of the tail. However, cracking continued because the structural modifications inevitably trans-

ferred damaging loads to weaker areas, depending on excitation frequencies [22]. Not until 1988, in an effort led by the Georgia Institute of Technology at the request of the USAF, was buffet finally understood as the likely cause of the fatigue cracking. Most severe at high angles of attack, tail buffet occurred when unsteady pressures associated with separated flow from the leading edge of the wings excited vibrational modes of the vertical tail assembly. Not only had these problems increased maintenance costs by requiring frequent inspections and repair, but they led to other problems such as internal corrosion and the limitation of the flight maneuver envelope.

Harmful buffet induced vibrations are not limited to vertical tails, but can affect antennas, skin panels and fins. The F-16 ventral fin, as shown in Figure 1.1, is an excellent example. Early F-16 models saw damage including total or partial loss of the ventral fin without pilot awareness. The problems were initially linked to inlet spillage turbulence during rapid decelerations [51]. Fortunately, damage to the fin was not a safety-of-flight concern as the fin was designed to enhance lateral stability during high speed flight, but continued failures elevated maintenance costs and affected mission availability. More failures occurred with the introduction of the LANTIRN pod, which is mounted aft of the engine inlet directly upstream from the ventral fin. Research conducted by the National Aerospace Laboratory in the Netherlands [51] pointed toward unsteady, separated flow downstream of the LANTIRN pod as a likely cause of elevated buffet loading in the fin. Several redesigns of the fin, centered around stiffness modifications, were attempted before a final design was accepted for Block-40 and later F-16 models.

Structural changes, in many cases, can lead to increased weight and cost, both a premium for high performance military aircraft. Although the redesigned ventral fins were able to meet life cycle requirements, other passive or active buffet alleviation techniques could provide a more efficient solution. For example, passive attempts for controlling buffet on the F/A-18, such as leading edge blowing/sucking or wing and fuselage fences, targeted vortex control as a way of influencing unsteady air flow around the vertical tails at high angles of attack. Leading edge fences used on the

F/A-18 were found to reduce the steady and unsteady pressures on the vertical tails where buffet problems occurred [35]. Still, these techniques provided limited success because they were only effective in specific flight conditions [36]. Also, there were concerns of detrimental effects to aircraft performance.

The use of smart materials in active control systems has shown great potential in buffet vibration problems. In 1995, a 1/6 scale F/A-18 model was tested in the Transonic Dynamics Tunnel at the NASA Langley Research Center as part of the ACROBAT program to assess the use of various active control systems in reducing vertical tail buffet [35]. The techniques explored included active rudder control, an actuated tip-vane, and piezoelectric ceramic wafer actuators attached to the tail's surface in areas of maximum strain density. The piezoelectric actuators, controlled by frequency domain compensation methods using strain gauges and accelerometers as feedback sensors, accounted for a 60% reduction in peak power spectral density values of the root bending moment of the wind tunnel model. In addition, the piezoelectric actuators maintained effectiveness during all tested flight conditions. Although the active rudder techniques appeared equally effective at low angles of attack, the rudder lost effectiveness as flow separated from the aircraft at higher angles of attack [36].

Since the tests of the ACROBAT program, piezoelectrics received much attention as a solution to buffet vibrations. The next section addresses the development of piezoelectric actuators and their application to buffet alleviation problems.

2.2 Piezoelectricity and its Application to Buffet Alleviation

Piezoelectricity, meaning pressure electricity, was first termed after the research of Pierre and Jaques Curie in 1880 who discovered that a weight placed on a crystal produced a charge proportional to the weight [40]. The Curies had, in fact, discovered the direct piezoelectric effect: the generation of an electric charge by a piezoelectric material when subjected to a mechanical strain. Subsequently, the Curies also discovered the reciprocal piezoelectric effect: when subjected to an electric charge, a piezoelectric material generates proportional strain. The presence of the direct and

reciprocal effects gives way to the ability of piezoelectric materials to function in many applications where the sensing or actuation of strain is desired [16].

There remain several other characteristics of piezoelectric materials pertinent to this research. First, dealing with the reciprocal piezoelectric effect, the elastic deformation in piezoelectric materials, whether they contract or elongate, depends on the sign and magnitude of the applied electric field. Second, the piezoelectric effect maintains a linear relationship between its electrical and mechanical properties [25]. For example, a piezoelectric sensor produces electric charges that are proportional to the change in deformation as long as the frequencies of deformations remain within the bandwidth of the sensor. Third, a piezoelectric material generally enjoys the advantage of a relatively short time constant, meaning it can respond to an applied electric field with little time delay. Finally, in order for the piezoelectric effect to occur, the material must be anisotropic and electrically poled [13], which means an electric field must be maintained throughout the material. This polarization, as well as the development of stress and strain within the material, is used to classify the response properties of piezoelectric materials and is denoted by the piezoelectric strain coefficient, d_{mn} , more commonly called the *charge constant*. The subscripts of the charge constant describe the application of the electric field and the corresponding strain or deflection within the material. In a d_{31} actuator, for example, the electric field is applied along the 1-axis where deflection occurs along the 3-axis. A visualization of the two piezoelectric actuation mechanisms is shown in Figure 2.1.

Since the Curies' discovery, piezoelectricity has aided advances in sonar technology, communication, crystal filters, high-frequency speakers, microphones, and accelerometers just to name a few [40]. Not until recently have research efforts extended piezoelectricity to the field of smart structures. The term 'smart structures' describes the integration of sensors and actuators, along with communication channels, processors, and other necessary components, into structural elements to obtain a state of desired static or dynamic control [13]. It is important to make the delineation between smart structures and smart materials, though the definitions may not be clear in the

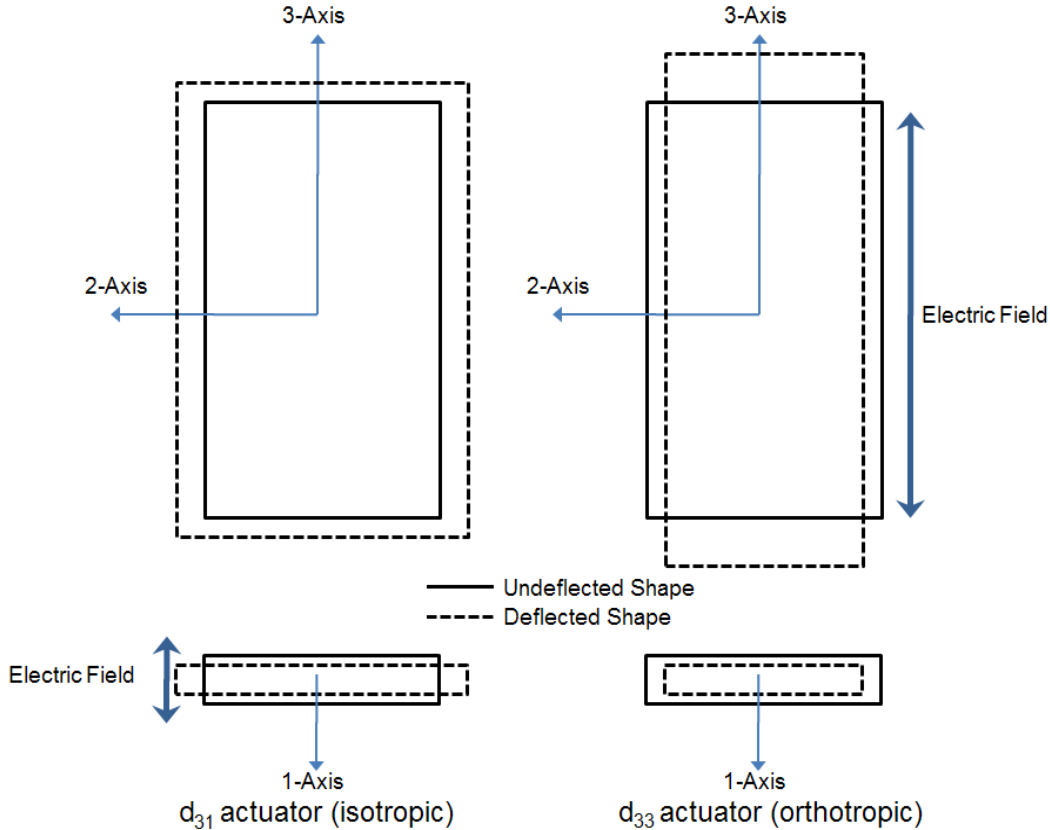


Figure 2.1: Comparison of Isotropic and Orthotropic Actuators [6]

literature. Smart structures use some type of feedback information to influence decisions according to desired future states or conditions where smart materials simply refer to the individual components used to provide feedback or actuation. The most common smart materials used today include piezoelectric materials, electrostrictive materials, and shape memory alloys.

Among the many piezoelectric materials, Lead-Zirconate-Titanate (PZT), a ceramic, and Polyvinylidene Fluoride (PVDF), a polymer, make up the two principal types used for sensing and actuation. Piezoelectric ceramics, arguably the most significant piezoelectric material when it comes to actuation [13], are composed of randomly oriented piezoelectric crystals. As further investigation into the properties of crystalline piezoelectrics can be found in the literature [13, 40], it is sufficient for this discussion to know that the vast majority of ceramic piezoelectrics used today are in

the PZT family chiefly because PZTs exhibit high piezoelectric activity and can be molded in a variety of arrangements tailored to specific applications.

Efforts to characterize or control aerodynamic vibrations with piezoelectric materials surfaced in the 1990s and included research in structural health monitoring [8], acoustic vibration control [18], and the alleviation of buffet-induced vibrations associated with high performance twin-tailed aircraft [22, 35]. Early on, PZT ceramic wafers were the most common piezoelectric actuator associated with vibration suppression [22]. However, PZT wafers presented several limitations when used with aircraft structures. First, their brittle nature led to disbondment or fracture in the presence of large-amplitude vibrations. Second, their rigid construction complicated installation on curved surfaces like those of modern aircraft. Finally, single PZT wafers typically employed the transverse d_{31} charge constant. In order to obtain sufficient control authority for most structural applications, large quantities of PZT ceramic wafers were arranged in stack configurations and oriented to collectively employ the stronger longitudinal d_{33} charge constant. Depending on design, these stacks could be bulky complicating installation within aircraft structures.

Nevertheless, in 1995, an effort at tail buffet alleviation on the F-15 led by Hanagud et al. [22] used piezoceramic stack actuators in an acceleration feedback control system with good results. During wind tunnel experiments using a scale model, the root-mean-square of vertical tail tip accelerations were reduced by as much as 30%. As mentioned previously, the ACROBAT program in 1995, an effort to control buffet induced vibrations on a wind tunnel model of the F/A-18 vertical tail, used piezoelectric ceramic wafers and arrived at as much as 60% reduction in peak power spectral density values of the tail root bending moment [35]. Piezoceramic wafers were also ground tested on a full scale F/A-18 vertical tail in 1997. The wafer actuators were effective at suppressing the vibration response of the vertical tail but several problems were identified, including insufficient control authority, which became apparent when conditions approached the maximum expected buffet load [20].

Piezoceramic composite actuators, like the macro-fiber composite (MFC) developed by the NASA Langley Research Center, presented a solution to the limitations of ceramic wafers. The following is an excerpt from the commercial brochure of Smart-Material Corporation which manufactures MFCs based on the NASA design.

The MFC is an innovative actuator that offers high performance and flexibility in a cost-competitive device. The MFC consists of rectangular piezoceramic rods sandwiched between layers of adhesive and electroded polyimide film. This film contains interdigitated electrodes that transfer the applied voltage directly to and from the ribbon shaped rods. This assembly enables in-plane poling, actuation, and sensing in a sealed, durable, ready-to-use package. When embedded in a surface or attached to flexible structures, the MFC provides distributed solid-state deflection and vibration control or strain measurements [47].

Made possible by its interdigitated electrodes, MFCs employ the stronger longitudinal d_{33} charge constant enabling greater electromechanical coupling than traditional PZT wafers. Burnham et.al. [6], who studied the use of piezoceramic composite actuators on the F/A-18 vertical tail, reported that actuators with interdigitated electrodes using the d_{33} charge constant outperformed those using the d_{31} constant by a factor of three for the same piezoelectric material. In addition, Burnham compared various piezoelectric actuators in production during the year 2000 and concluded that the MFC design produced by NASA exhibited the lowest ratio of required voltage to limit voltage, a favorable quality when accounting for high voltage sources required to drive piezoelectric actuators.

Macro-fiber composites also enjoy the advantage of flexibility over traditional PZT wafers. The use of piezo-fibers instead of wafers allow for greater damage resistance and simplified installation, especially on curved surfaces. The combination of the d_{33} charge constant and greater flexibility provides for larger forces and free displacements. For these reasons, also reflected in Morgenstern's design recommendations [7], only piezoelectric actuators of the MFC design using the d_{33} charge constant were considered in this research.

The most recent research for buffet-alleviation techniques using piezoelectric materials involved piezoceramic composite actuators with interdigitated electrodes. Moses, et.al. [43], as part of the Evaluation of New Actuators in a Buffet Loads Environment (ENABLE) program, investigated the performance of two interdigitated electrode actuators using the d_{33} charge constant, the MFC designed by NASA and the Active Fiber Composite actuator designed by the Continuum Control Corporation. The actuators were evaluated on the vertical tails of a 1/6 scale model F/A-18 in the Transonic Dynamics Tunnel at NASA Langley and “performed similarly and superbly in reducing structural responses caused by buffet” [43]. In 2000, Burnham et al. [6] showed that a 1.5 mm thick multilayered directional actuator having the same properties as the MFC outperformed other actuator designs in a finite element analysis. In 2003, after NASA modified manufacturing processes to enable affordable and repeatable construction of MFC actuators, the F/A-18 BLA program moved again to a full-scale ground test of an active control system, this time using the MFC design instead of piezoceramic wafers. The MFC actuators were attached to the surface of a full-scale vertical tail in an area of maximum strain density and used to control the first-torsion mode (45 Hz). Various control algorithms were evaluated during different load cases. Although not effective for all control algorithms evaluated, the MFC actuators showed encouraging levels of vibration suppression and an estimated increase in fatigue life at critical locations from 7,500 hours to 12,540 hours [38].

As shown in this discussion, the use of smart materials in an active control system can reduce the damaging effects of buffet vibration on military aircraft and extend the useful life of affected structures. The capability of MFC actuators, in particular, is promising, but success in past testing has often depended on total system performance to include control algorithms and power supplies. The following section provides design methodologies common in active structural control as well as pitfalls of power supply design.

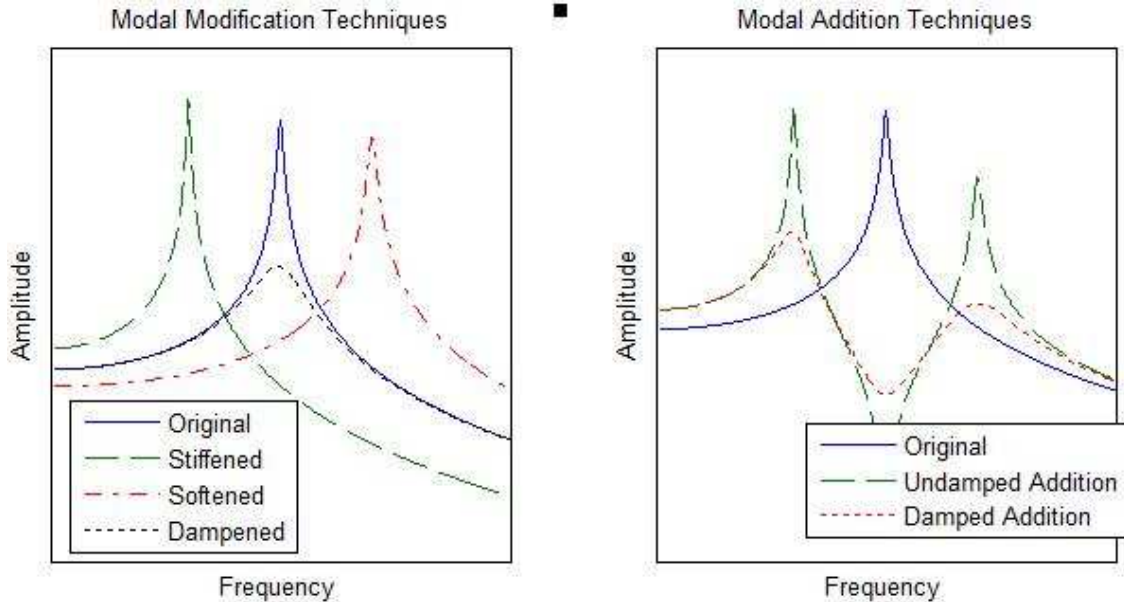


Figure 2.2: Modal Modification and Addition Techniques [1]

2.3 Control Methodologies in Buffet Alleviation

Traditional solutions to vibration control can be categorized by the intended modal response of the actively controlled system: that which directly change the modal properties of the system and that which introduce additional vibration modes to the system [1]. Figure 2.2 depicts the effect of these methods to a generic single-input single-output (SISO) frequency response function. Softening or stiffening acts to move the natural frequency of a system, which can be advantageous when trying to avoid specific narrow band inputs. For example, the unsteady airflow which causes buffet on the F/A-18 vertical tails is known to occur within a narrow-band of frequencies. Vertical tail stiffening could be tailored to move the tail's natural frequencies away from this narrow-band disturbance. If the natural frequency of the structure falls outside of the buffet disturbance, buffet would have much less of a damaging impact on the vertical tail. Modal addition essentially works the same as stiffening or softening except that, instead of moving an existing mode, a new mode is added before or after an existing mode, causing a shift in the existing mode away from a narrow band input. Modal damping can be used with either technique to lower the response of a

system at a particular frequency and may actually shift the natural frequency slightly. Damping is advantageous if the extent of the input is unknown or if its bandwidth is sufficiently wide making the previously mentioned techniques ineffective.

Passive attempts to alleviate buffet vibration on the ventral fin of the F-16 mentioned in the previous section included measures that increased the stiffness of the fin. Initially, modifications were made to strengthen areas prone to failure, such as the the attach bolts and the area surrounding the forward attach point. Although not the intent of the modifications, it was known that a stiffness change to an attach point or to that of the surrounding structure impacted modal frequencies [51]. Comparing Block-15 ground vibration data to Block-30 and Block-40 NASTRAN simulation data shows negligible change to mode 1 and 2 frequencies. Noticeable change occurs, however, with higher frequency modes, the largest reported being a 12 Hz change in Mode 6 between Block-15 and Block 40 designs [51].

Since the report of ventral fin failure analysis [51] did not account for the bandwidth of the buffet disturbance, it is unclear if the stiffness modifications were able to move any of the fin's modal frequencies outside of the damaging range of buffet vibrations. Morgenstern concluded, using an aeroelastic flutter analysis, that modes 1, 2 and 4 were the most critically influenced by buffet vibrations [7]. The stiffness modifications to the ventral fin did not move these modal frequencies more than a few Hertz; therefore, it can be assumed that the stiffness modifications did not move the modal frequencies beyond the buffet disturbance band. Damping, therefore, remains a viable option in affecting the frequency response of the fin.

Influencing the damping of a structure using piezoelectric actuators can be relatively straightforward. For example, the strain of the structure can be fed into a controller that applies a voltage to a piezoelectric actuator according to the sensed strain. The response of the actuator to an applied voltage is mechanical strain which can be designed to be equal and opposite to the detected strain, thus minimizing net vibration. There exist numerous control development methods that can accom-

plish this effect, such as strain rate feedback, acceleration feedback, positive position feedback, and other robust control techniques. However, the success of an active control system not only depends on the effectiveness of the control algorithm but on sensor/actuator selection and location.

2.3.1 Sensor Selection and Location. As previously stated, this research used Morgenstern's [7] macro-fiber composite actuator design recommendations. Morgenstern, however, did not specify a particular sensor for feedback control. Many sensors are available for vibration control including accelerometers, strain gauges, and piezoelectric sensors. Sensor selection, in many ways, drives control algorithm development. In the absence of additional performance feedback, control system sensors are often used to measure success. For example, many active control systems that employ acceleration feedback control use acceleration levels at the location of the sensor as a way to measure the effectiveness of the control system. Sensor placement can also greatly influence stability characteristics of the closed-loop system. Goh and Caughey [21] showed that the presence of observation spillover, a consequence of the interaction of sensor dynamics and uncontrolled or unmodeled modes within the bandwidth of the controller, had destabilizing effects, especially when controlling low frequency modes. They argued that careful selection and placement of sensors can help alleviate these effects.

The majority of past attempts at controlling buffet vibrations used acceleration feedback control. Hanagud [22] and Pototzky [38], researching buffet alleviation on the F-15 and F/A-18 vertical tails, respectively, positioned accelerometers at the tip of the tails near the leading edge to provide feedback. Placing accelerometers near the free end of a cantilevered beam or plate is common because displacement is greatest at the free end, enabling greater detectability of most vibration modes. Both Moses [35, 43] and a team from the National Research Council of Canada [9], in developing controllers for the F/A-18 vertical tail, evaluated two different types of feedback sensors in several control systems, some using accelerometers mounted at the

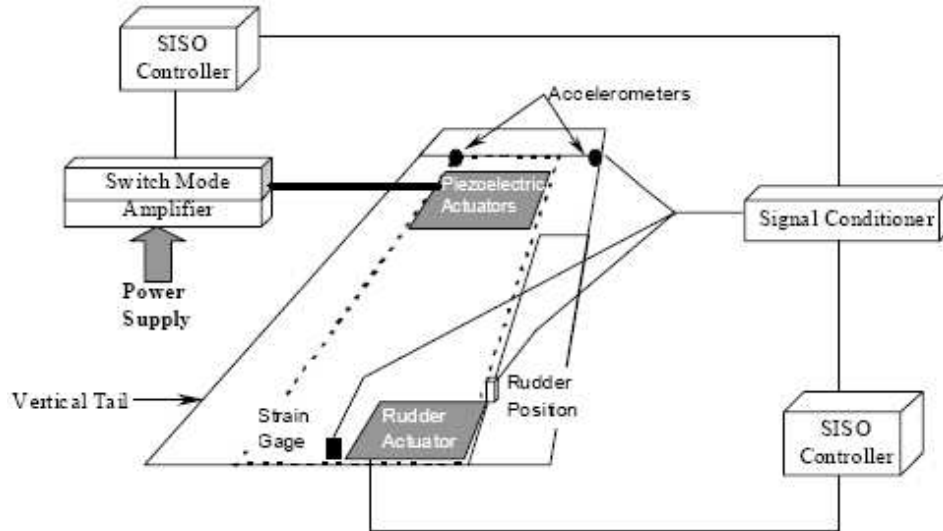


Figure 2.3: Major Components of the F/A-18 BLA System [38]

tips of the tails, which provided feedback for the first torsion mode, and others using strain gauges mounted at the root, which provided feedback for the first bending mode. The strain gauge, which measured bending moment, was placed at the root where the bending moment was maximum. Figure 2.3 depicts the location of actuators and sensors used for ground tests of F/A-18 vertical tail buffet alleviation. Unfortunately, each sensor targeted a separate vibration mode making it difficult to assess which performed better.

In most cases, the sensors and actuators are not collocated for various reasons. In the example of Figure 2.3, the areas of maximum strain energy for a particular mode, where actuators were located, did not necessarily coincide with the optimum location for a particular sensor. Several advantages exist, however, with collocated designs, including favorable closed-loop stability. Collocated sensors and actuators lead to symmetric transfer functions where poles and zeros appear in pairs for each natural frequency of the system. From the perspective of a root locus plot, the pole-zero pairs alternate near the imaginary axis. Preumont determined that this property “guarantees the asymptotic stability of a wide class of SISO control systems even if the system parameters are subject to large perturbations” because the root-loci remain entirely within the left-half plane [40]. In non-collocated control, the interlacing

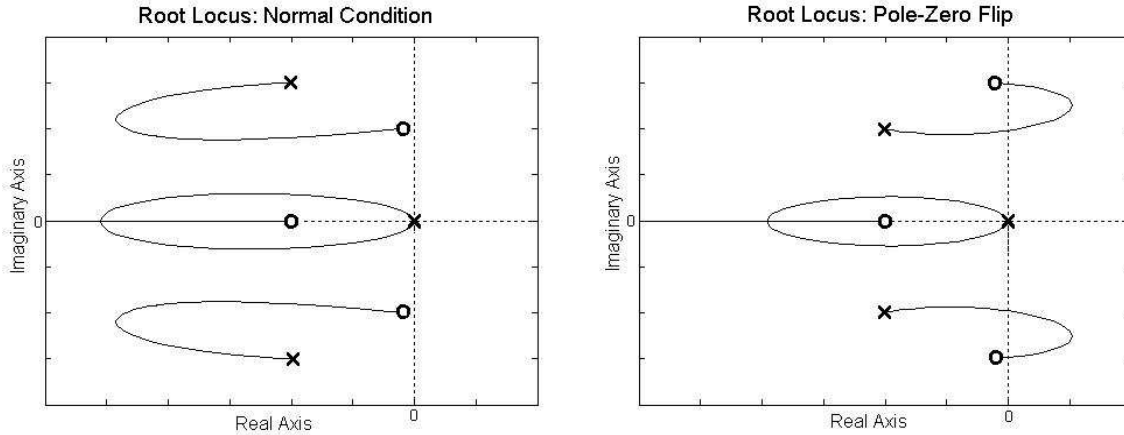


Figure 2.4: Affect of Pole-Zero Flipping on System Stability [40]

of pole-zero pairs breaks down and could result in pole-zero flipping, a potentially destabilizing condition. Damping, then, becomes an essential design variable for non-collocated systems in order to protect against instabilities [40]. Figure 2.4 shows how the stability of a system, when the root locus enters the right half plane, is affected by pole-zero flipping in an arbitrary system.

A number of active damping schemes have been developed and tested using various types of collocated actuators and sensors. What's interesting is that these control schemes can be implemented in a decentralized manner where collocated actuator and sensor pairs make up independent SISO systems whose stability can be verified by simple methods, such as root-locus. This means that control system design can be simplified where separate collocated sensor-actuator pairs are used to independently control individual vibration modes. Several efforts have also explored the optimization of sensor and actuator placement. Schultz and Heimbold [44] presented a method of maximizing dissipation energy by an optimal set of actuators and sensors and feedback gains. Kondoh et al. [28] used the linear quadratic optimal control method to optimize actuator and sensor placement and feedback gains. Interestingly enough, each of these optimization methods using distinct cost functions arrived at a common design recommendation: collocated sensors and actuators.

The benefits of collocated control are clear. Most research advocating for collocated control of piezoelectric actuators also modeled feedback sensors as piezoelectric materials. Although specifically designed for actuation, piezoelectric actuators such as the MFC have been shown to possess excellent strain sensing capability. Piezoelectric sensors are essentially strain rate sensors outputting charges proportional to displacements. Sodano et.al. [48] studied the use of MFCs for the specific use as a sensor in various applications. His results revealed that, compared to conventional piezo film (PVDF) or piezoceramic sensors, MFCs worked exceptionally well as a sensor in a modal-testing system, a structural health monitoring system, a feedback control system, and as a self-sensing actuator where a single MFC component acted simultaneously as a sensor and actuator.

Recent studies of self-sensing piezoelectric actuators have uncovered several advantages, the most obvious being true collocated control. A self-sensing actuator can also eliminate the closed-loop control problems arising from capacitive coupling between separate piezoelectric sensor and actuator elements [16]. Still, the separation of sensing and control signals shared in a common piezoelectric device, which often calls for the real-time estimation of the equivalent capacitance of the piezoelectric device, requires significant effort. Pourboghraat et al. [39] developed adaptive filters for the self-sensing piezoelectric actuator to eliminate the applied voltage to the actuator from the sensor signal and demonstrated its effectiveness on a cantilevered beam. Dosch et al. [16] developed a bridge circuit to enable measurement of strain or strain rate of a self-sensing piezoelectric actuator allowing for the implementation of a variety of control algorithms. Despite the advancements in self-sensing piezoelectric actuators, the application of the adaptive filters like that of Pourboghraat et al. and Dosch et al. are outside the scope of this research. Therefore, a near collocated approach where piezoelectric sensors are embedded within piezoelectric actuators will be explored as discussed in Section III.

2.3.2 Control Methods. There are many control methods available to vibration control problems including classical methods like pole placement and output feedback. Modern robust techniques, such as time domains specifications like Linear Quadratic Gaussian (LQG), H_2 , and H_∞ control, are commonly considered mostly due to stability guarantees associated with robust methods. As mentioned before, previous efforts to alleviate buffet vibrations employed acceleration feedback control; however, different techniques were used to arrive at suitable control algorithms. Hanagud et al. [22] used the H_2 optimal control method for F-15 tail buffet alleviation during full scale ground tests. Hanagud’s acceleration feedback controller resulted from “the minimization of the H_2 norm of the closed-loop impulse response, which [was] also the minimization of the closed-loop covariance of the displacement in the presence of unit white noise disturbance” [22]. Hanagud’s approach simplified the design in that damping was the only design variable necessary to define the controller.

Buffet alleviation efforts on F/A-18 vertical tails saw many different control approaches. Moses [35, 43] employed frequency domain compensation techniques in SISO control designs that used feedback from either accelerometers or strain gauges. The resulting control algorithms resembled low pass or band pass filters with peaks near the targeted natural frequency in order to concentrate control energy at those frequencies. In an additional effort on the F/A-18 buffet problem, Pototzky [38] and a team from the National Research Council of Canada [9] used the LQG optimal control method, which is a special formulation of the H_2 technique, to design acceleration feedback controllers. The LQG regulator has been popular in vibration control problems in that it balances performance and control effort while accounting for process and measurement noise.

The H_∞ method represents another robust control technique that has seen use in vibration problems. Falangas et al. [18] used H_∞ in designing an acceleration feedback control system using piezoelectric actuators in alleviating acoustic vibrations on a panel aft of the main engines of the B-1 bomber. The H_∞ method is similar to the H_2 method, except that the H_∞ formulation minimizes the H_∞ norm, or the worst

case energy transfer from plant input to output. The H_∞ method rejects bounded energy disturbances, tracks signals minimizing worst case errors, and accounts for a robust controller design. To implement an H_∞ controller, Falangas first arrived at a reduced order model of the surface panel careful to include all vibrations modes near those to be actively controlled, because the H_∞ method guarantees stability for all modes included in the design model. For example, Falangas wished to control the first symmetric mode at 430 Hz, but included modes at 570, 630, and 740 Hz because of their proximity to the first mode, and to the cross-over frequency of the accelerometer input. Next, Falangas applied an H_∞ synthesis model to arrive at a controller that stabilized the aircraft panel dynamic model. Shaping filters were also used to ensure low and high frequency disturbances did not interfere with the control algorithm. As much as a 13 dB reduction in acceleration power spectral density (PSD) measurements were recorded during a flight test of Falangas' control algorithm [18].

Despite the control methodology used, the goal of most vibration control algorithms is to directly control energy at or near the system's natural frequencies, or vibration modes, of interest. Thus, peaks appear in the controller's transfer function at points where the designer wishes to direct controller energy. An interesting technique following this concept surfaced in 1985, termed positive position feedback (PPF), when Goh and Caughey [21] studied stability problems caused by finite actuator dynamics in the collocated control of large space structures using piezoelectric actuators and sensors. Because they represent highly distributed parameter systems requiring high-order models, controlling vibration in large space structures presented a difficult problem. Goh and Caughey found that, when dealing with very high order models, optimal control methods were often plagued by observation spillover which tends to destabilize uncontrolled or unmodelled modes, specifically those at higher frequency. Direct velocity feedback was known to be unconditionally stable in the absence of actuator dynamics [21]; however, actuator dynamics cannot always be neglected. In light of this, Goh and Caughey worked to prove that PPF algorithms using collocated control were not destabilized by finite actuator dynamics. In fact,

they noted the most important advantage of PPF was that “unconditional global stability conditions [could] be derived analytically and easily satisfied” [21].

Overall, many control methods have been successfully implemented in vibration control problems. The control designer is forced to balance performance and stability requirements in order to meet system objectives. In modern robust techniques, the selection of design coefficients is often a trial and error affair until the desired response is achieved. Still, these concerns do not represent all a designer must consider when developing an active control system, especially when using piezoelectric actuators. Power amplifier design had largely been neglected until the realization in the early 1990’s that traditional linear power amplifiers were impractical for integration in real-world applications such as aircraft and small vehicles where space and weight are a premium. The next section discusses research surrounding switching amplifiers and their application toward piezoelectric control.

2.4 Drive Amplifier

Since piezoelectric actuators first saw use in vibration control, most research focused on the development of the actuators and their application potential. Few actually considered the wider problem of the control system as a whole, specifically efficient power supplies and drive amplifiers. Because the impedance of piezoelectric actuators is primarily reactive, their load imposed on a circuit regenerates a significant amount of power to the driving amplifier. The reactive impedance also implies that the driving amplifier must be able to handle significantly higher voltages and circulating currents than suggested by the real power requirements of the actuator [32]. Overall, a clear understanding of the electromechanical behavior of the piezoelectric actuator, as studied by Brennan & McGowan [3] and Warkentin & Crawley [53], is essential in the design of power amplifiers that drive them.

From the beginning, linear amplifiers were widely used to drive piezoelectric actuators due to their excellent frequency response to inputs signals, minimal ripple voltage noise, and favorable linearity. However, the size and weight of linear amplifiers

increase as voltage levels increase. Also, linear amplifiers cannot efficiently handle the bi-directional power flow found in driving large piezoelectric actuators, because piezoelectric devices consume almost zero real power but cause a large amount of reactive power to circulate between the source and the load [32]. This circulating reactive power is manifested as power losses in linear amplifiers and is dissipated as heat. Leo [30] found that the energy dissipated in a linear amplifier is a function of supply voltage to the actuators and drive-frequency. As supply voltage and drive frequency increase, so does dissipated energy.

The switching amplifier, like that patented by Joseph P. Savicki from AT&T Bell Laboratories [52], provided a novel design for driving capacitive loads. The switching amplifier recovers a substantial amount of stored energy during the discharge of a capacitive load as recycled power, which, when routed to series-connected capacitors, can be reused during subsequent load discharge cycles without causing circuit noise [52]. Switching amplifiers can follow many different topologies such as the half-bridge or full-bridge circuits or variations of multi-level topologies. Many use pulse width modulated (PWM) drive signals to control circuit switching. The majority of switching amplifiers designed to drive piezoelectrics placed inductors in series with the piezoelectric load, as shown in Figure 2.5. Doing so enables the control of current rate instead of the current into the load. “When a switching amplifier is used to control the average voltage across the inductor, and hence current rate, very little power is dissipated in the drive amplifier” [10]. Further study of switch-mode amplifier topologies and design considerations can be found in the literature [10, 32, 33].

Switching amplifier technology has been successfully applied to vibration control applications using piezoelectric actuators. Clingman and Gamble of Boeing Phantom Works designed a switching amplifier used to drive piezo-fiber composite actuators imbedded in a 1/6 scale CH-47 helicopter blade [10]. The multi-level amplifier, used to switch solid state Isolated Gate Bipolar Transistors (IGBT) according to a PWM drive signal, was tested at 4000 volts peak-to-peak, 750 mA with good results. Data

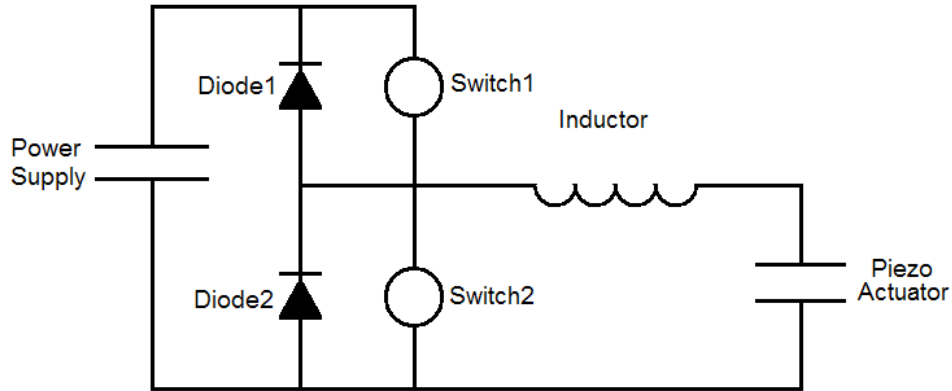


Figure 2.5: Basic Design of a Piezo Switching Amplifier [10]

showed nearly undistorted drive voltage from the amplifier with minimal noise due to switching. The F/A-18 BLA program also realized the need for more efficient power supplies and designed custom switch-mode amplifiers for use on the Air Vehicles Technology Integration Program during full scale ground tests of piezoelectric actuation systems [38]. The amplifiers provided ± 1500 volts to a nominal $4.5 \mu\text{F}$ piezoelectric load and dissipated less than half the energy of previously assessed linear amplifiers.

When piezoelectric actuators are used in buffet-induced vibration problems on modern aircraft, amplifiers and the entire control system must be designed to efficiently integrate onto an aircraft. Size and weight constraints, cooling air, and electrical system compatibility are some of the major concerns. More efficient piezoelectric actuators, such as the MFC, require voltages anywhere from 200 to upwards of 4000 volts, depending on design, to meet performance requirements of some vibration control problems. As stated before, high voltage translates to bulky linear amplifiers making them impractical for use on aircraft. The switching amplifier with its smaller profile seems naturally suited for use on aircraft to drive large capacitive loads at high voltages by the most efficient means possible.

III. Theoretical Background

This chapter presents a summary of the theoretical framework necessary in the development of elements required to realize a flight test of an F-16 ventral fin buffet alleviation system. These elements include the optimum placement of piezoelectric actuators and sensors, the experimental determination of principle strain vectors of the ventral fin, the frequency response estimation of the ventral fin, the development of appropriate closed-loop control algorithms, the development of an appropriate piezoelectric drive amplifier, and the implementation of the control algorithms in hardware.

3.1 Piezoelectric Actuator Placement, Sizing, and Orientation

The correct placement, sizing, and orientation of piezoelectric actuators is crucial to the success of a buffet alleviation system. The basic concept behind the function of the actuators is the cancelation of moments produced by outside forces [29]. In terms of this research, aerodynamic buffet causes moments which create stress in the ventral fin. MFC piezoelectric actuators, as described in Chapter II, using the transverse charge constant (d_{33}), impart strain in response to an electric charge in the direction of their actuation fibers. When mounted to a surface like the ventral fin, piezoelectric actuators can counteract the strain caused by aerodynamic buffet. As a result, it is preferred to locate the actuators in areas of elevated strain associated with a particular mode of vibration, since each mode has a unique mode shape and strain energy distribution.

Morgenstern [7] arrived at the same conclusion in his investigation into the effectiveness of piezoelectric actuators for the F-16 ventral fin. Morgenstern tuned and optimized a finite element model (FEM) to match published modal parameters for a Block 15 ventral fin and analyzed the results to determine strain energy profiles for the first five modes of vibration. He determined the three most critical modes for fin failure, modes 1, 2 and 4, through an evaluation of historical flight test data detailing the relative dominance of each mode and the amount of aeroelastic damping observed in flutter analysis. Morgenstern incorporated piezoelectric models for the critical

modes into an aeroelastic analysis placing them in areas of maximum strain energy density. Figures 3.1 and 3.2 illustrate the areas of maximum strain energy density for the first and second modes, respectively. The black lines indicate recommended piezoelectric actuator placement and size based on relative strain energy per unit area.

Morgenstern’s research showed that piezoelectric actuators specifically located in areas of elevated strain with the principle piezoelectric effect direction aligned with the principal strain vectors provided for the highest probability of success in improving aeroelastic damping. The orientation of the piezoelectric fibers define the principle piezoelectric effect direction for orthotropic actuators, those utilizing the d_{33} charge constant as shown in Figure 2.1. Thus, the fibers of orthotropic actuators should be aligned with the direction of principle strain for the targeted vibration mode. Morgenstern [7] provided an analytical prediction of the principle strain vectors as shown in Figures 3.3 and 3.4.

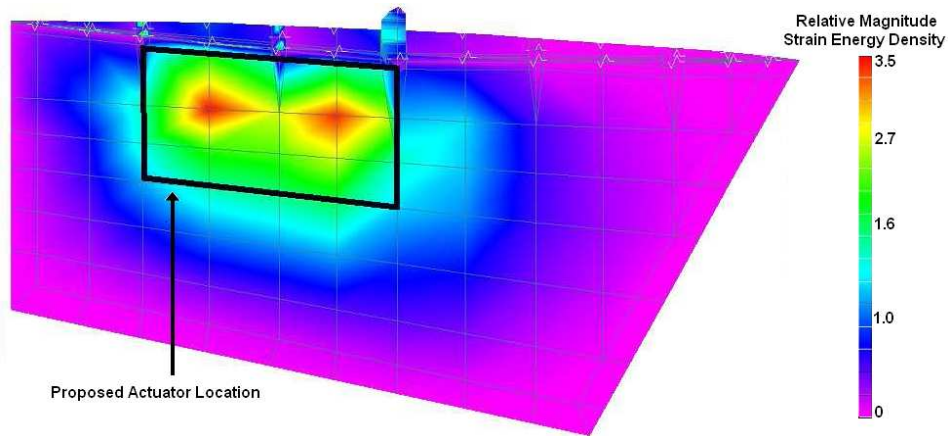


Figure 3.1: Mode 1 (78 Hz) Strain Energy Plot and Recommended Patch Location [7]

3.1.1 Experimental Determination of Principle Strain Vectors. The ventral fin used in flight testing of this research is a Block 15 F-16 ventral fin of unknown structural health. Therefore, the experimental determination of modal characteristics, including principle strain direction, is crucial prior to installation of piezoelectric hardware and control system development.

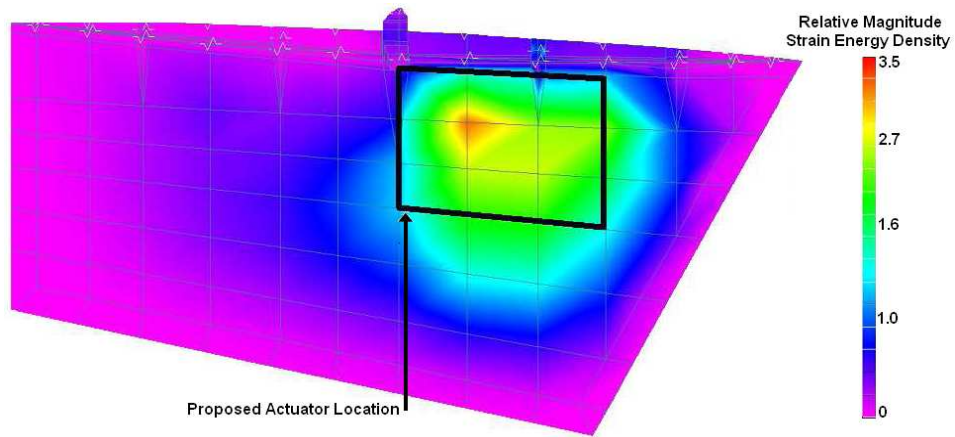


Figure 3.2: Mode 2 (96 Hz) Strain Energy Plot and Recommended Patch Location [7]

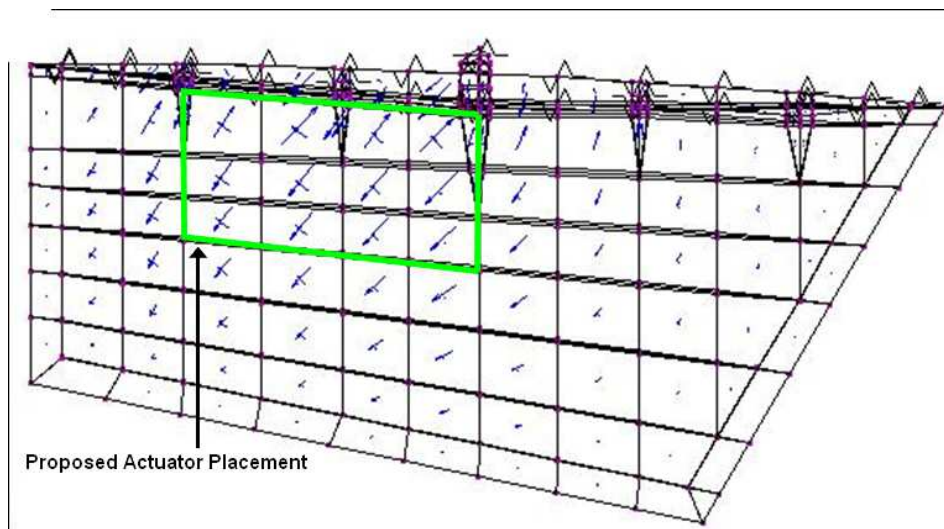


Figure 3.3: Mode 1 (78 Hz) Principle Strain Vector Orientation and Recommended Patch Location [7]

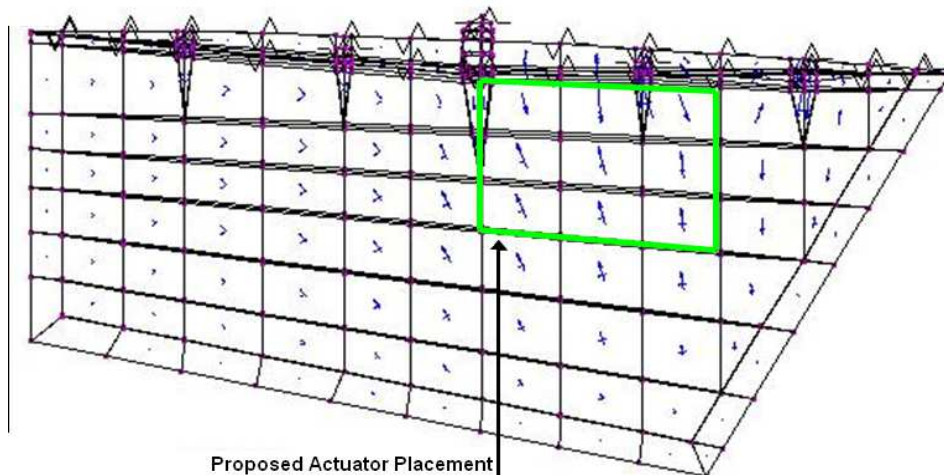


Figure 3.4: Mode 2 (96 Hz) Principle Strain Vector Orientation and Recommended Patch Location [7]

Strain gauges provide a straight-forward method of determining principle strain direction. However, strain gauges are limited in that multiple, precisely aligned strain gauges would be required to gather strain information over a large area. What's more, strain gauges require intensive installation and calibration procedures. Since strain is proportional to curvature and curvature is the second derivative of displacement, strain information can be obtained for a large area if surface displacements for a specific mode shape are known. A scanning laser vibrometer can measure vibration over a wide frequency band and large area and provide accurate natural frequency and mode shape data. Velocity information, taken from the Doppler shift of the laser beam due to the surface's motion, can be used to obtain surface displacements. If scan coordinates are defined properly, displacement data can be used to calculate curvature of the surface using a central difference method.

Take, for example, five points aligned at constant intervals along a straight line as shown in Figure 3.5. Given displacements w parallel to the beam of a laser vibrometer and perpendicular to the line of points along a surface, the slope and curvature of the line can be determined by Equations 3.1 and 3.2, respectively, where x_n is the location of point n . Axial strain is the curvature times the distance from



Figure 3.5: Curvature Example

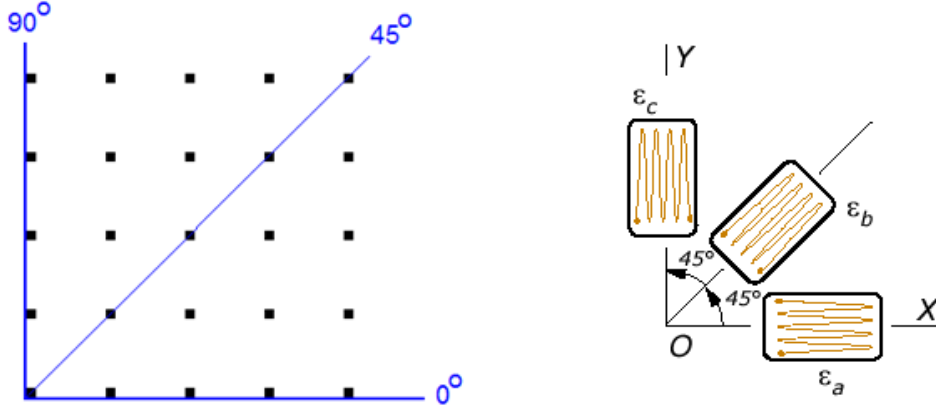


Figure 3.6: Strain Rosette from Laser Vibrometer Scan Grid Points

the neutral axis of bending.

$$\left(\frac{dw}{dx}\right)_n = \frac{w_{n+1} - w_{n-1}}{x_{n+1} - x_{n-1}} \quad (3.1)$$

$$\left(\frac{d^2w}{dx^2}\right)_n = \frac{\left(\frac{dw}{dx}\right)_{n+1} - \left(\frac{dw}{dx}\right)_{n-1}}{x_{n+1} - x_{n-1}} \quad (3.2)$$

This method can be expanded to find curvature over a two-dimensional surface given a grid of known points. If the grid is designed with constant interval points aligned square to one another, curvature can also be calculated at a 45 degree angle along the grid, as shown in Figure 3.6. As a result, principle strain magnitude and direction can be found using the equations for principle strain, ϵ_1 , for a 45 degree strain rosette, as shown in Equation 3.3 below.

$$\epsilon_1 = \frac{1}{2}(\epsilon_a + \epsilon_c + \sqrt{2(\epsilon_a - \epsilon_b)^2 + 2(\epsilon_b - \epsilon_c)^2})^2 \quad (3.3)$$

where ε_a , ε_b , and ε_c are measured strain along the 0° , 45° , and 90° directions of the grid. Principle strain direction, θ , is given in Equation 3.4 measured from the 0° reference axis.

$$\tan 2\theta = \frac{\varepsilon_a - \varepsilon_c}{2\varepsilon_b - \varepsilon_a - \varepsilon_c} \quad (3.4)$$

3.2 Piezoelectric Sensor Placement and Orientation

The advantages of collocated sensor and actuator designs for feedback control were discussed in Chapter II. Areas of elevated strain energy do not necessarily coincide with the optimal location for an acceleration feedback sensor, ruling out accelerometers for this collocated design. Conversely, a piezoelectric sensor, which employs the reverse piezoelectric effect, is best suited for feedback control in a collocated piezoelectric actuator design. As verification, Chandrasekaran and Linder [31] provide us with a relationship between piezoelectric sensor output voltage v_o , charge Q , and stress T :

$$v_o = \frac{Q}{C} - \frac{d_{33}}{\varepsilon_{33}} T d \quad (3.5)$$

where C is capacitance, d_{33} is the transverse piezoelectric charge constant, ε_{33} is the dielectric permittivity, and d is the thickness of the piezoelectric material. Equation 3.5 shows that the voltage across the sensor is a result of the direct capacitive effect and mechanical stress. Stress in a plate can be shown as

$$T = E \frac{y}{\mathcal{R}} \quad (3.6)$$

where E is Young's Modulus, y is half the plate's thickness, and \mathcal{R} is the radius of curvature of the plate. Assuming small distortion in the plate, the radius of curvature is

$$\frac{1}{\mathcal{R}} = \frac{\partial^2 w}{\partial x^2} \quad (3.7)$$

Equations 3.5, 3.6, and 3.7 show that sensor output voltage is proportional to curvature. Therefore, piezoelectric sensors placed in areas of maximum curvature, or strain, will provide the largest voltage signal for feedback control. Given that piezoelectric sensors are constructed in the same manner as actuators, it follows that the main piezoelectric fiber direction should be oriented with the principle strain vectors as described in the previous section.

3.3 System Model Identification

Mathematical models that adequately describe a system's response are necessary in the design of closed-loop control algorithms for that system. FEM analysis has long been the accepted method for constructing analytical models in the structures field. However, in terms of a vibration control system and in light of the actual Block 15 ventral fin's age and unknown structural health, a realization from experimental results would provide a more accurate model for control algorithm development. The eigensystem realization algorithm (ERA) offers an efficient means to experimentally determine a system model.

The eigensystem realization algorithm was first proposed by Juang and Pappa [26] for modal parameter identification and model reduction of linear dynamical systems from test data. A detailed description of the ERA algorithm can be found in the literature [26,27], but it can be summarized as a reduced system model based on the singular value decomposition of the block Hankel matrix. Take for example the linear, discrete time system represented by

$$\begin{aligned} x(k+1) &= A_{[n \times n]}x(k) + B_{[n \times p]}u(k) \\ y(k) &= C_{[q \times n]}x(k) + D_{[q \times p]}u(k) \end{aligned} \tag{3.8}$$

where x is an n -dimensional state vector, u is a p -dimensional input vector, and y is a q -dimensional output vector with k as the discrete time sample. Matrices A , B , C , and D define the system model where matrix A represents the dynamics of the system

including its mass, stiffness, and damping properties. The time domain description of the free pulse response of the system in Equation 3.8 are known as the Markov parameters given by

$$Y(k) = CA^{(k-1)}B \quad (3.9)$$

The ERA builds the block Hankel matrix H in terms of the Markov parameters, shown as

$$H(k-1) = [Y(k)...Y(k+n_c)...Y(k+n_r)...Y(k+n_r+n_c)] \quad (3.10)$$

where r and c are arbitrary integers satisfying the inequalities $rq \geq n$ and $cp \geq n$ [11]. The block matrix of Equation 3.10, which acts to minimize the distortion caused by measurement noise, is then factored using single value decomposition at $k = 1$ into

$$H(0) = PDQ^T \quad (3.11)$$

where the matrices P and Q are orthonormal and \mathcal{D} is diagonal containing the singular values. The number of states in Equation 3.11 can be truncated to obtain optimal signal-to-noise characteristics of the system model [27]. Juang and Pappa [27] provide an optimization method for computing the appropriate singular value cutoff for this truncation using the covariance of the measurement noise. The result is a reduced-order dimension- n realization formulated as

$$\begin{aligned} A^k &= \mathcal{D}_n^{-1/2} P_n^T H(k) Q_n \mathcal{D}_n^{-1/2} \\ B &= \mathcal{D}_n^{1/2} Q_n^T [I_p, 0] \\ C &= [I_q, 0] P_n \mathcal{D}_n^{1/2} \\ D &= Y(0) \end{aligned} \quad (3.12)$$

where $[I, 0]$ is the identity matrix of stated dimension appended with a zero matrix.

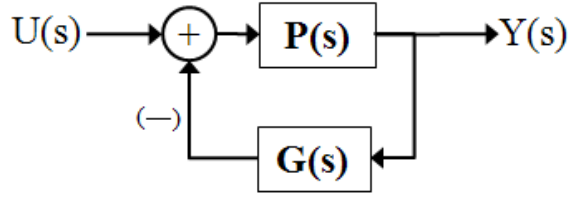


Figure 3.7: Simple Block Diagram

Thus, the eigensystem realization algorithm provides a system model using matrix definitions in Equation 3.12 with Equation 3.8 for the development of closed-loop control algorithms.

3.4 Control Algorithm Development

The foundation to determine a state-space realization of a dynamic system was introduced in the previous section. That realization is applied to an overall system architecture in order to develop closed-loop control algorithms. Figure 3.7 illustrates a nominal feedback system where $P(s)$ represents the plant and $G(s)$ represents the control algorithm coded in the controller hardware. For this research, the plant model, constructed from the ERA, includes all components of the buffet alleviation system, such as the ventral fin, the piezoelectric actuators and sensors, the drive amplifier, and the digital control hardware. Grouping all components of the system together in the plant model simplifies development of the control algorithm. However, it is important to define the performance objectives for the controlled system prior to development of the control algorithm.

Since we have chosen piezoelectric sensors for feedback, it is convenient to use those sensor signals as a measure of performance. The output of a piezoelectric sensor is voltage. The root mean square (RMS) voltage and the power spectral density of the voltage time history can provide a measure of vibration intensity and frequency dependent vibration magnitude, respectively. In terms of controller design, these measures of performance translate into a disturbance rejection problem. This research

focuses on two control techniques well suited for this type of problem: positive position feedback and the Linear Quadratic Gaussian compensator.

3.4.1 Positive Position Feedback. As presented in Chapter II, positive position feedback (PPF) was first introduced by Goh and Caughey [21] in 1985 who desired a second-order dynamic feedback technique that did not require an analytical model of the system or plant to be controlled. Because PPF filters are essentially a second-order compensator, they possess roll-off at high frequency, making them resistant to spillover and residual mode excitation. What's more, closed-loop stability depends only on the structure's natural frequencies which can be easily measured. Inman [24] describes the PPF formulation and its stability characteristics by beginning with a single degree-of-freedom system (Equation 3.13) and a second-order compensator of the same form (Equation 3.14).

$$\ddot{x} + 2\zeta_n\omega_n\dot{x} + \omega_n^2x = bu \quad (3.13)$$

$$u = \frac{g}{b}\omega_c^2\eta$$

$$\ddot{\eta} + 2\zeta_c\omega_c\dot{\eta} + \omega_c^2\eta = g\omega_c^2 \quad (3.14)$$

where x is the structural modal coordinate, η is the compensator coordinate, ω_n and ω_c are the structural and compensator natural frequencies, respectively, ζ_n and ζ_c are the structural and compensator damping ratios, respectively, b is the input coefficient and g is the scalar gain ($g > 0$). Combining the two equations into matrix form, assuming zero outside force, yields

$$\begin{bmatrix} \ddot{x} \\ \ddot{\eta} \end{bmatrix} + \begin{bmatrix} 2\zeta_n\omega_n & 0 \\ 0 & 2\zeta_c\omega_c \end{bmatrix} \begin{bmatrix} \dot{x} \\ \dot{\eta} \end{bmatrix} + \begin{bmatrix} \omega_n^2 & -g\omega_c^2 \\ -g\omega_c^2 & \omega_c^2 \end{bmatrix} \begin{bmatrix} x \\ \eta \end{bmatrix} = \begin{bmatrix} 0 \\ 0 \end{bmatrix} \quad (3.15)$$

$$K = \begin{bmatrix} \omega_n^2 & -g\omega_c^2 \\ -g\omega_c^2 & \omega_c^2 \end{bmatrix}$$

where K is the stiffness matrix. An inspection of the stiffness matrix reveals that the two coordinates x and η are coupled, meaning that an increase in compensator damping adds damping to the structure. Also, by definition, if the symmetric stiffness matrix is positive definite, that is, if its determinant is greater than zero, the closed-loop system is stable. This is possible when

$$g^2\omega_c^2 < \omega_n^2 \quad (3.16)$$

showing that closed-loop stability of the PPF controlled system depends only on the natural frequency of the structure. Thus, the design of the PPF controller resides in the selection of g and w_c that satisfy Equation 3.16 and the selection of ζ_c that adds sufficient damping to the structural mode [24]. The question remains, however, how to make the appropriate choices for the characteristics of the PPF compensator.

Song et.al. [49] provide an excellent analysis of how compensator frequency and damping ratio should be selected. Using the same single degree-of-freedom example from before, the steady state output of the PPF compensator from Equation 3.14, assuming closed-loop stability, is

$$\eta(t) = \beta e^{i(\omega_c t - \phi)} \quad (3.17)$$

where β is the magnitude and ϕ is the phase of the output. The phase angle ϕ is given as

$$\phi = \arctan \left[\frac{2\zeta_c(\omega_n/\omega_c)}{1 - (\omega_n^2/\omega_c^2)} \right] \quad (3.18)$$

Three conditions arise in the relation between compensator and structural natural frequency. When the compensator frequency is much lower than the structural frequency, ϕ approaches zero. When the compensator and structural frequencies match, ϕ approaches $\pi/2$. When the compensator frequency is much greater than the structural frequency, ϕ approaches π . Each of these cases have different effects on the

structural dynamics of Equation 3.13, as shown below.

$$\begin{aligned}
\text{Case 1: Active Flexibility:} \quad & \phi \rightarrow 0, \quad \ddot{x} + 2\zeta_n\omega_n\dot{x} + (\omega_n^2 - g\beta\omega_n^2)x = 0 \\
\text{Case 2: Active Damping:} \quad & \phi \rightarrow \pi/2, \quad \ddot{x} + (2\zeta_n\omega_n + g\beta\omega_n)\dot{x} + \omega_n^2x = 0 \\
\text{Case 3: Active Stiffness:} \quad & \phi \rightarrow \pi, \quad \ddot{x} + 2\zeta_n\omega_n\dot{x} + (\omega_n^2 + g\beta\omega_n^2)x = 0
\end{aligned}$$

In Case 1 and 3, the structural stiffness term was decreased and increased, respectively, whereas in Case 2, the structural damping was increased. Thus, the compensator frequency should closely match the structural frequency in order to meet the PPF design goal of achieving maximum damping. However, any structural frequency below ω_c will experience an increase in flexibility, as shown in Case 1. Structural modes higher than ω_c , as long as they are well separated from ω_c , will be less affected due to the magnitude roll-off characteristic of a second-order filter at higher frequencies.

Damping ratio selection is less intuitive. Let's start with the transfer function of the nominal PPF controller.

$$\frac{\eta(s)}{X(s)} = \frac{g\omega_c^2}{s^2 + 2\zeta_c\omega_c s + \omega_c^2} \tag{3.19}$$

Figure 3.8 shows the Bode plot of Equation 3.19 with $\omega_c = 1$ rad/sec and varying damping ratios ζ_c . A larger damping ratio results in a less steep magnitude and phase response at the target frequency, effectively increasing the region of active damping and thereby increasing the robustness of the compensator [49]. However, as the magnitude response ‘flattens,’ the compensator becomes less effective at the target frequency. As stated before, higher damping values lead to an increase in flexibility for modes of lower frequency than ω_c . Therefore, damping ratio selection becomes a tradeoff between compensator robustness, low frequency mode flexibility, and target mode damping effectiveness. The above technique will be implemented as described in Chapter IV.

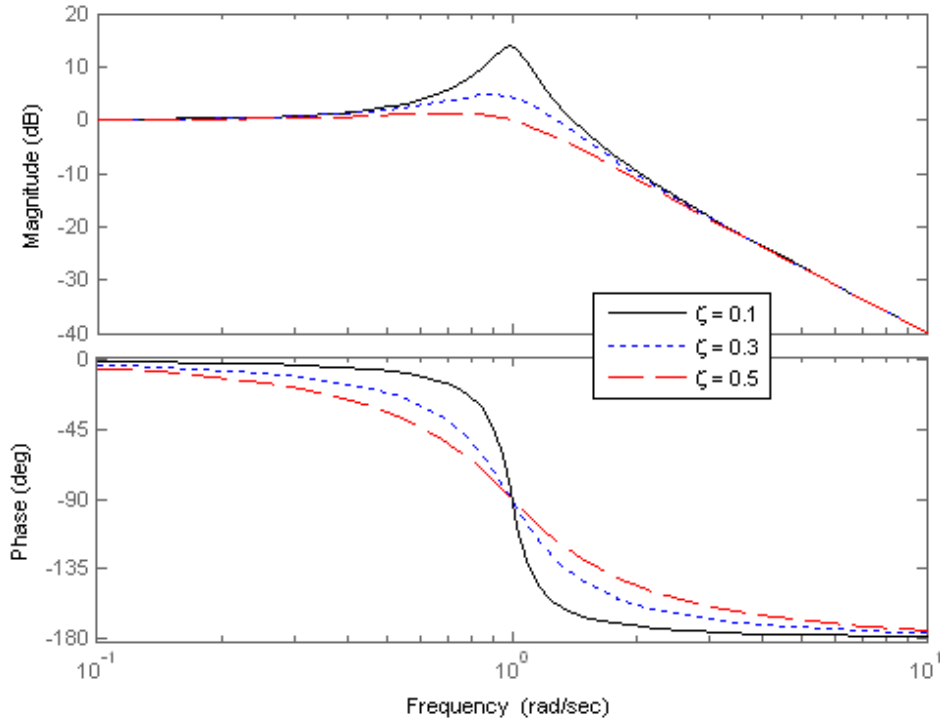


Figure 3.8: Bode Plot for PPF of Various Damping Ratios

3.4.2 Linear Quadratic Gaussian. The second control technique used in this research involves the Linear Quadratic Gaussian (LQG) compensator. The LQG compensator is attractive for vibration control problems because it generates a feedback controller that can handle noisy, partial state measurements to control a plant whose initial state is random and is subject to white noise disturbances. This is possible with the LQG optimal controller because it is the combination of a Kalman filter and a Linear Quadratic Regulator (LQR). This separation of design components, known as the separation principle, which states that the eigenvalues of the LQR and Kalman filter solutions are independent, allows the designer to develop each component independently.

The Linear Quadratic Regulator uses a quadratic cost function allowing the designer to balance performance criteria and desired control influence. This flexibility becomes invaluable when dealing with high-order systems where classical methods lose capability. However, the main limitation with LQR is the need for exact mea-

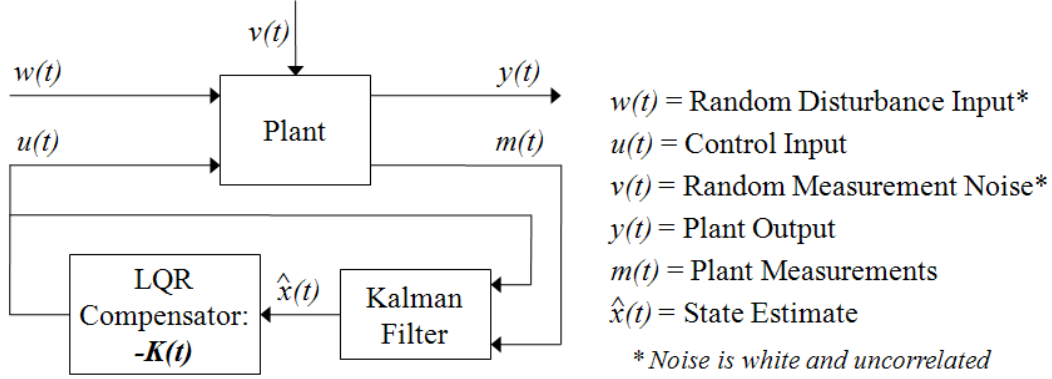


Figure 3.9: LQG Control Block Diagram [5]

surement of the entire state, a potentially expensive requirement for complex systems. Some states in complicated systems can not be measured exactly or they can not be measured at all depending on sensor configuration. A Kalman filter added to the LQR allows the compensator to overcome this limitation by estimating the entire state from partial state measurements. The Kalman filter is an optimal estimator of the state because it minimizes the mean square estimation error [5]. What remains is an optimal controller design that has minimized the LQR quadratic cost function, provided the estimated states perform closely to the actual states.

To formulate an LQG compensator, first consider the generic LQG optimal control system block diagram shown in Figure 3.9 which also includes the definitions of variables used in the formulation. The plant from Figure 3.9 is described by the following linear state-space equations.

$$\begin{aligned}
 \dot{x}(t) &= Ax(t) + B_u u(t) + B_w w(t) \\
 y(t) &= C_y x(t)
 \end{aligned}
 \tag{3.20}$$

where the plant measurements $m(t)$ are

$$m(t) = C_m x(t) + v(t)
 \tag{3.21}$$

According to Burl [5], the LQG optimal control is obtained from the LQR feedback gain matrix K operating on the state estimate $\hat{x}(t)$, discussed in the next section, generated by the Kalman filter.

$$u(t) = -K(t)\hat{x}(t) \quad (3.22)$$

As stated previously, we can divide the formulation of the LQG controller into two parts due to the separation principle: the Linear Quadratic Regulator and the Kalman filter.

3.4.2.1 The Quadratic Cost Function. The goal of any optimal control system is to drive the desired output (or output errors, depending on design criteria) to zero while using the least amount of control input. The LQR compensator accounts for this relationship with the quadratic cost function, $J(x(t), u(t))$, written here in terms of the state and control coordinates.

$$J(x(t), u(t)) = \frac{1}{2}x^T(t_f)Hx(t_f) + \frac{1}{2} \int_0^{t_f} (x^T(t)Qx(t) + u^T(t)Ru(t)) dt \quad (3.23)$$

where H is positive semi-definite and sets the importance of the final condition of the states, Q is positive semi-definite and sets the importance of each state, and R is positive definite and sets the penalty of excess control input $u(t)$. If the system under control is assumed to be time-invariant, the LQR and Kalman gains approach a constant value as the final time, t_f , is increased. If the time intervals are long, the design can be simplified with the use of constant state feedback gains, simplifying the cost function to

$$J(x(t), u(t)) = \frac{1}{2} \int_0^{\infty} (x^T(t)Qx(t) + u^T(t)Ru(t)) dt \quad (3.24)$$

Thus, the designer needs only to define Q and R . For example, if the designer is more concerned with the first two states of the system, the values in Q that affect

those two states would be defined with higher magnitudes than the values affecting the remaining states. The same is done for R in reference to control inputs. Note that LQR and Kalman discussions that follow assume time-invariant, steady-state.

3.4.2.2 The Linear Quadratic Regulator. For the time invariant, constant gain LQG compensator, the LQR feedback gain matrix is defined as

$$u(t) = -Kx(t) = -R^{-1}B_u^T Px(t) \quad (3.25)$$

Matrices R and B_u are known; what's left to define is P , the matrix of proportionality between the costate and state. Burl [5] presents two methods of determining P . The first method deals with determining the state-transition matrix for the Hamiltonian system which can be a very tedious process. Because we are concerned with the steady-state solution, a more elegant method is found in the solution of the algebraic Riccati equation, a nonlinear matrix equation shown below.

$$0 = -PA - A^T P - Q + PB_u R^{-1} B_u^T P \quad (3.26)$$

Many software applications, such as MATLABTM, are often used to solve for the LQR gain matrix. By defining the system in Equation 3.20 and the weighting matrices Q and R , these software applications solve the Riccati equation, assuming a time invariant system, and calculate the LQR gain matrix while satisfying the quadratic cost function, Equation 3.24.

3.4.2.3 The Kalman Filter. As shown in Figure 3.9, the Kalman filter provides an estimate of the state of the plant, $\hat{x}(t)$, which is driven by the control input $u(t)$ and plant noise $w(t)$ and whose measurements $m(t)$ are influenced by measurement noise $v(t)$. The Kalman filter equation in state model form is

$$\dot{\hat{x}}(t) = [A - LC_m]\hat{x}(t) + B_u u(t) + Lm(t) \quad (3.27)$$

where L is the Kalman filter gain matrix. The filter gain matrix can be found using the same methods described for the LQR gain matrix because the filter gain matrix is defined similarly as

$$L = \Sigma_e C_m^T S_v^{-1} \quad (3.28)$$

The matrix Σ_e is the solution to steady-state Riccati equation shown below.

$$\begin{aligned} 0 &= \Sigma_e A^T + A \Sigma_e + B_w S_w B_w^T - \Sigma_e C_m^T S_v^{-1} C_m \Sigma_e & (3.29) \\ S_v \delta(\tau) &= E[v(t)v^T(t + \tau)] \\ S_w \delta(\tau) &= E[w(t)w^T(t + \tau)] \end{aligned}$$

where S_v is the spectral density of the measurement white noise, $v(t)$, S_w is the spectral density of the disturbance input noise, $w(t)$, and E is the expected value operator [5].

Again, computer software is often used to apply the Kalman filter to a control design where the designer defines the system matrices, A , B_u and C_m and assumes a time-invariant system and white noise disturbances to obtain the filter gain matrix. In most software applications, such as MATLABTM, the designer can specify the noise covariance data, represented by S_v and S_w above, to tailor the estimator behavior.

3.4.2.4 The Linear Quadratic Gaussian Compensator. The Linear Quadratic Regulator and the Kalman filter can then be combined, assuming that the model in Equation 3.20 is the true model of the plant, to form the Linear Quadratic Gaussian optimal controller that minimizes the cost function in Equation 3.24 and accounts for process noise shown in Figure 3.9. The resulting system of equations in steady-state form, now incorporating the estimated states from the Kalman filter, are

$$\hat{\dot{x}}(t) = [A - LC_m - B_u K] \hat{x}(t) + Lm(t) \quad (3.30)$$

$$u(t) = -K(t) \hat{x}(t) \quad (3.31)$$

3.4.3 Closed-Loop Stability. Feedback control can introduce additional dynamics into a system which may or may not drive the system to an unstable state. Thus, one of the most important characteristics of closed-loop control is stability prediction and verification. A well-accepted method to determine system stability is the Nyquist stability criterion. To illustrate this method, take the closed-loop transfer function from Figure 3.7, expressed in the Laplace domain.

$$\frac{Y(s)}{U(s)} = \frac{P(s)}{1 + P(s)G(s)} \quad (3.32)$$

The denominator of the right side of Equation 3.32 constitutes the characteristic equation of the system in the form $1 + P(s)G(s) = 0$. It can be shown that the system in Figure 3.7 is stable if and only if all of the solutions of the characteristic equation have negative real parts [5], that is, if all the poles of the characteristic equation fall within the left half-plane. This quality leads us to the Nyquist stability criterion developed by Harry Nyquist in 1932 as a method to determine the closed-loop stability of a system from the open-loop frequency response [37].

Two important design characteristics can be obtained from evaluating the open-loop frequency response according to the Nyquist criterion and plotting that response on a Nyquist plot. First, as mentioned, the stability of the closed-loop system can be determined.

A feedback system is stable if and only if the image of a closed contour encircling (in the clockwise direction) the right half-plane as mapped through $[P(s)G(s)]$, the open-loop transfer function, encircles the point minus one N_p times in the counterclockwise direction, where N_p is the number of poles of $[P(s)G(s)]$ in the right half-plane. [5]

Second, the gain and phase stability margins can be readily obtained from the Nyquist plot of the open-loop frequency response. Gain margin is defined as the minimum gain increase that results in the closed-loop system becoming unstable. Phase margin is defined as the minimum amount of phase shift that results in the closed-loop

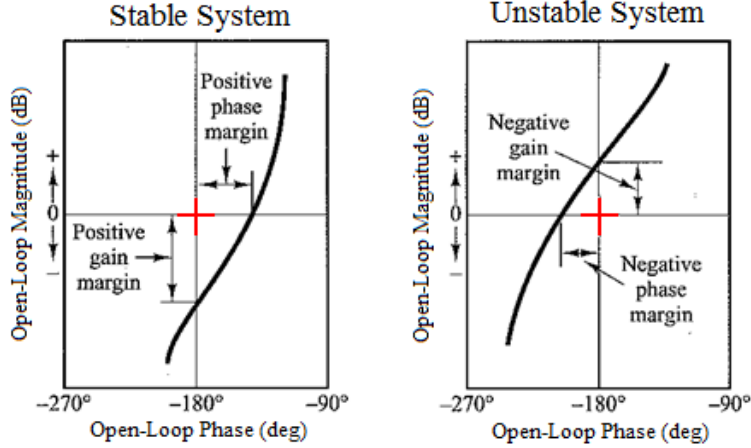


Figure 3.10: Stability Margins from a Nichols Chart /citeogata.

system becoming unstable. A positive gain or phase margin indicates stability where a negative gain or phase margin indicates instability.

System stability and stability margins can be obtained from other plotting tools that use the Nyquist stability criterion, including the Bode plot and Nichols chart. To assess closed-loop stability and stability margins, this research employs the Nichols chart, which is a combination of the magnitude and phase components of a Bode presentation. Figure 3.10 illustrates examples of a stable and unstable closed-loop system according to their stability margins. Using these tools to predict and verify system stability and stability margins, the design of an appropriate control algorithm can begin.

3.5 Implementation of Control Algorithms in Software

In order to implement the control algorithms in digital hardware, the continuous system models must be converted to discrete time form. The transfer function given in Equation 3.32 can be represented as a continuous transfer function in the form

$$\frac{P(s)}{1 + P(s)G(s)} = \frac{b_m s^m + b_{m-1} s^{m-1} + \dots + b_o}{s^n + a_{n-1} s^{n-1} + \dots + a_o} \quad (3.33)$$

which can be discretized using the impulse response function and a convolution summation. However, this type of discrete time simulation carries the burden of lengthy input histories and heavy computational burden from the convolution summation. The finite difference equation provides a more efficient alternative. For digital simulation, Reid [41] presents a convenient formulation of an approximate difference equation for the continuous time model of Equation 3.33 that, when solved for the output $y_T(k)$, takes the form

$$\begin{aligned}
 y_T(k) = & - a_{T_{n-1}}y_T(k-1) - a_{T_{n-2}}y_T(k-2) - \cdots - a_{T_0}y_T(k-n) \\
 & + b_{T_m}u_T(k-1) + b_{T_{m-1}}u_T(k-2) \cdots + b_{T_0}u_T(k-m)
 \end{aligned} \tag{3.34}$$

The coefficients $[a_{T_{n-1}}, \cdots, a_{T_0}]$ and $[b_{T_m}, \cdots, b_{T_0}]$ are similar to those in Equation 3.33 except they are dependent on the sample time T . To solve for the current output $y_T(k)$, Equation 3.34 requires the past n values of the output ($y_T(k-n)$) and the past n values of the input ($u_T(k-n)$), assuming that the original continuous time model was not improper ($m \leq n$).

Implementing Equation 3.34 in digital software is fairly simple. The sample time T refers to the sample rate of the digital controller and the coefficients a_{T_n} and b_{T_n} can be obtained from existing software applications, such as MATLABTM, once the compensator in Equation 3.33 and the sample time are defined.

The National Instruments Inc. Compact Reconfigurable Input-Output (cRIO) digital controller using the LabVIEWTM software package was chosen to implement digital feedback control algorithms and to serve as an interface to the piezoelectric drive electronics. Figure 3.11 shows the actual hardware components of the cRIO control unit. As shown in Figure 3.12, the controller analog-to-digital (A/D) input module receives piezoelectric sensor signals from the amplifier after signal conditioning. The signal is then routed through the field programmable gate array and computer module (if required) before the digital-to-analog (D/A) output module sends the feedback signal to the amplifier to drive the actuators.



Figure 3.11: Compact RIO Control Unit Hardware Components

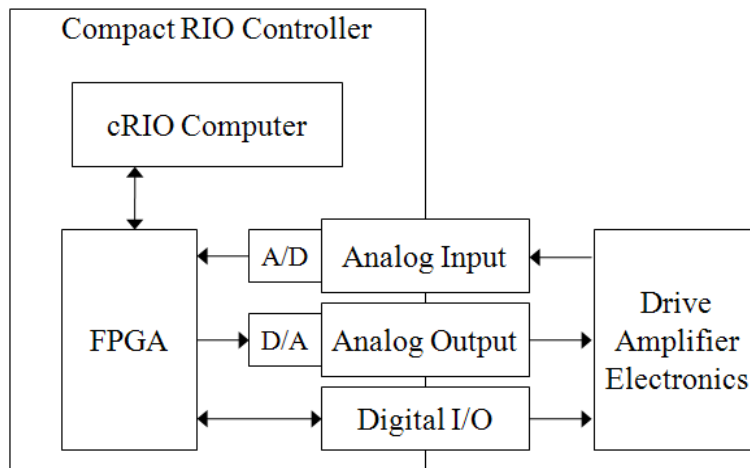


Figure 3.12: Compact RIO Control Unit Block Diagram

The cRIO controller utilizes a field programmable gate array (FPGA) to interface between the input and output modules and the computer module responsible for the operation of the digital control unit. The FPGA can be programmed directly to handle various types of operations; for example, the control algorithm itself can be programmed directly onto the FGPA, enabling faster sample rates and fixed-step computation times and ensuring deterministic control of the plant. The control techniques described above can be realized in a transfer function as small as second-order, like the PPF algorithm, or as a more complicated algorithm, like an LQG compensator. Regardless of the number of states in the compensator, the digital controller must be able to maintain the desired data rate. The FPGA offers a vehicle to achieve this goal.

IV. Methodolgy

The overall objective of this research was to develop and test a buffet alleviation system for a Block 15 F-16 ventral fin. Several steps were accomplished toward that objective. The piezoelectric actuators and sensors were specified and acquired based on several factors discussed in this chapter to alleviate vibrations of the first two modes of the ventral fin. The natural frequencies, mode shapes, and principle strain vector orientations of the Block 15 ventral fin were experimentally determined prior to installation of the piezoelectric hardware. A custom switch-mode amplifier was designed and built to drive the piezoelectric actuators. The system transfer function of the instrumented ventral fin was determined in the laboratory and control algorithms were optimized to alleviate vibrations in the first two modes. Finally, the system was installed on an F-16 aircraft and ground and flight tested at the USAF TPS.

4.1 Piezoelectric Actuator and Sensor Design

As stated in Chapter II, MFC piezoelectric actuators and sensors were used in this research. Morgenstern [7] concluded that the most critical vibration modes for ventral fin failure were modes 1, 2, and 4. Morgenstern asserted that, due to principle strain vector magnitude and orientation, vibration suppression of mode 1 and 2 could be accomplished with one layer of piezoelectric actuators. However, modes 3 and 4 would require two layers of actuators due to the magnitude of the minor principle strain of those modes. He recommended orienting the actuation fibers of each layer with the major and minor axis of principle strain, respectively. Table 4.1 lists the characteristics of the first four modes according to Morgenstern's research.

4.1.1 Mode Selection. The buffet alleviation system developed in this research targets only modes 1 and 2 for two reasons. First, as the number of piezoelectric actuator layers increase, so does the real power requirement. Brennan and McGowan [3] provide an approximation for the power consumption of piezoelectric

Table 4.1: Block 15 F-16 Ventral Fin Historical Modal Frequencies [7]

	<i>Mode Number</i>			
	1	2	3	4
FEM Natural Frequency	69.1 Hz	88.6 Hz	140.6 Hz	208.2 Hz
Recommended Actuator Layers	1	1	2	2
Recommended Actuation Fiber Direction, 1st Layer*	140 deg	15 deg	110 deg	155 deg
Recommended Actuation Fiber Direction, 2nd Layer*	N/A	N/A	20 deg	65 deg

* See Reference [7] for axis orientation

actuators as

$$P = \frac{1}{2}\omega V^2 C \quad (4.1)$$

where ω is the actuator drive frequency, v is the drive voltage, and C is the actuator capacitance. Equation 4.1 shows that actuation of higher frequency modes or the use of actuators with higher capacitance would increase the real power requirement. For layered piezoelectric actuators, the total capacitance is the sum of the capacitance of each actuator. Thus, the real power requirement increases for layered configurations. Second, the areas of maximum strain, that is the areas where piezoelectric actuators would be installed, overlap for mode 2 and 4, as shown in the Figures 3.2 and 4.1. Therefore, due to the power requirement and installation complications of multi-layered piezoelectric actuators for modes 3 and 4, only modes 1 and 2 are addressed in this research.

4.1.2 Actuator Design. In order to lower acquisition costs, the piezoelectric actuators and sensors used for modes 1 and 2 were designed to be identical. Still, due to the need for a collocated sensor, two piezoelectric patch designs were specified. The first design, Figure 4.2, was a 12 by 4 inch MFC actuator whose actuation fibers were aligned along the length of the patch. The second design, Figure 4.3, was of the same size and fiber orientation, but included an embedded piezoelectric sensor

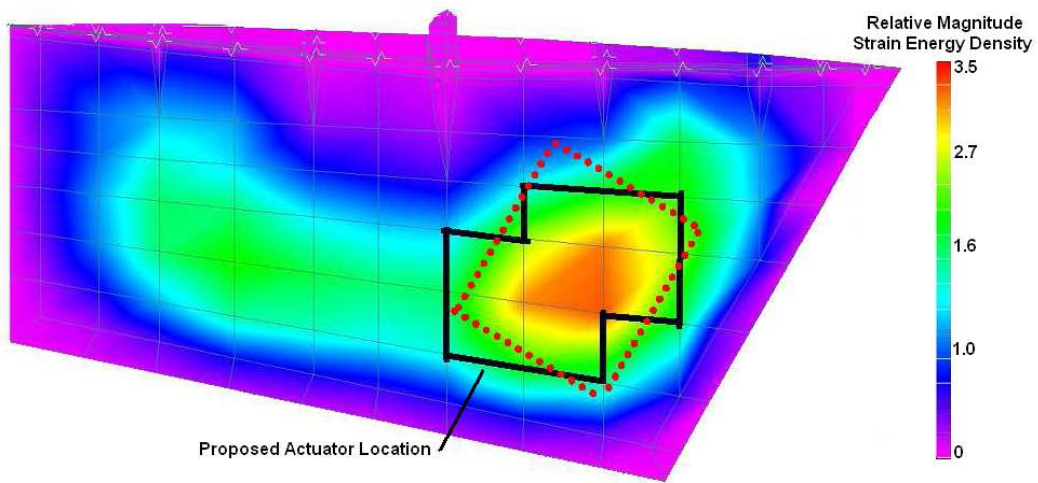


Figure 4.1: Mode 4 (233 Hz) Strain Energy Plot and Suggested Patch Location [7]

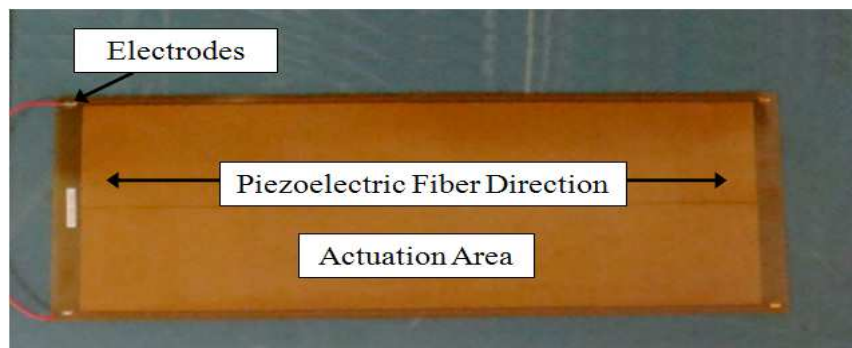


Figure 4.2: Piezoelectric Actuator, Design 1

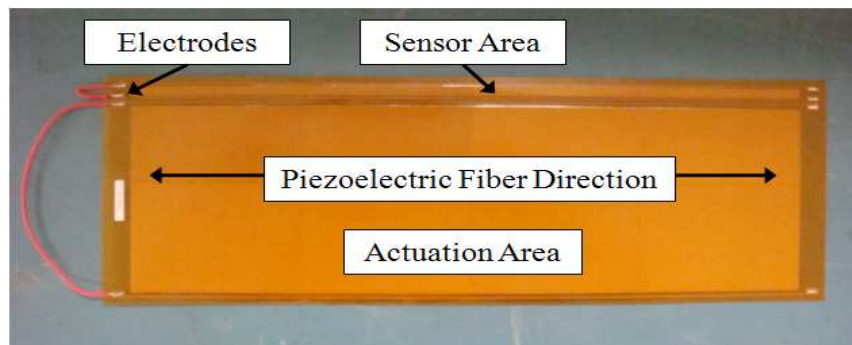


Figure 4.3: Piezoelectric Actuator, Design 2 (with embedded sensor)

Table 4.2: Piezoelectric Actuator/Sensor Specifications¹

High-field ($E > 1kV/mm$), biased voltage operation piezoelectric constants:	
d_{33} ²	4.6E+02 pC/N
Low-field ($E < 1kV/mm$), unbiased voltage operation piezoelectric constants:	
d_{33} ²	4.0E+02 pC/N
Free-strain* per volt (low-field - high-field)	0.75 - 0.9 ppm/V
Free-strain hysteresis ²	0.2
DC poling voltage, V_{pol}	+1500V
Poled capacitance at 1kHz, room temp, C_{pol}	2.7nF/in ²
Operational Parameters:	
Operation voltage range	-500V to +1500V
Maximum operational tensile strain	4500ppm
Peak work-energy density	1000in - lb/in ³
Maximum operating temperature	150°F
Operational Bandwidth	< 10kHz

¹ Taken from Smart-Material Corporation commercial literature, www.Smart-Material.com

² Fiber-direction

running the length of the patch along one side. The MFC piezoelectric patches were custom manufactured by the Smart-Material Corporation and their specifications are listed in Table 4.2.

Two actuator patches and one actuator/sensor patch adequately covered the areas of maximum strain energy for each mode. The piezoelectric fibers were oriented along the length of the patch and the patches were oriented on the fin's surface as shown in Figure 4.4 to align the fibers with the principle strain directions of each mode. Figure 4.4 shows the inboard side of the ventral fin and illustrates how three patches were configured for each mode actuation area. The outboard side has the same configuration. Thus, both arrays accounted for twelve patches in total. The six piezoelectric patches targeting mode 1 mounted on the aft end of the ventral fin were referred to as the 'aft' array and the six piezoelectric patches targeting mode 2 mounted on the forward end of the ventral fin were referred to as the 'forward' array.

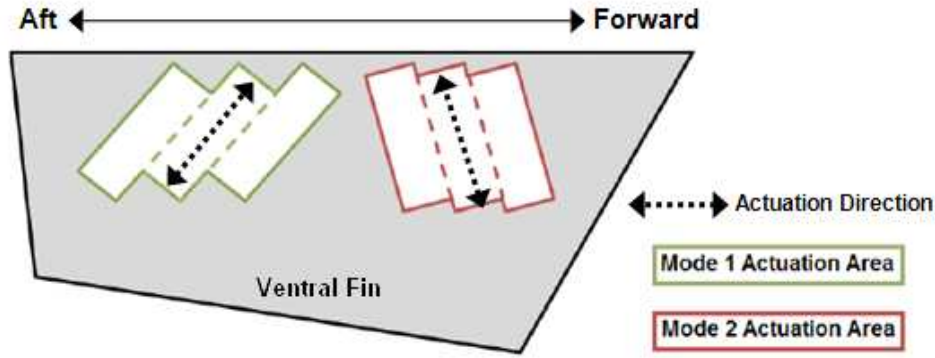


Figure 4.4: Piezoelectric Actuator Orientation on the Ventral Fin.

4.2 Natural Frequency and Mode Shape Verification

The Block 15 F-16 ventral fin used in this research was manufactured in the early 1980's and was carried on an unknown number and type of missions during its operational life. It was not certain how closely the test fin's frequency response would match that of published Block 15 ventral fin data. Thus, it was important to verify the frequency response prior to piezoelectric hardware installation and control law development.

To verify the natural frequency and mode shapes of the test fin, a scanning laser vibrometer using PolyTec[®] software version 8.6¹ was used to measure and analyze the frequency response of the fin. The scanning laser was programmed to take measurements at each point of a pre-defined grid across the entire inboard surface of the fin. The PolyTec[®] software application recorded and processed the measurements of the laser vibrometer and provided the natural frequencies and mode shapes with relative modal displacement and velocity magnitude. An electromagnetic shaker attached to the outer edge of the fin was used to excite the test fin during the vibrometer scan. A pseudo-random white Gaussian noise excitation signal was chosen to drive the electromagnetic shaker due to its favorable coherence over other excitation waveforms. The results of the laser vibrometer test are included in Tables 4.3 and 4.4.

¹PolyTec Inc., Waldbronn, Germany

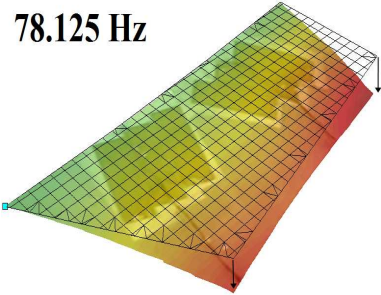
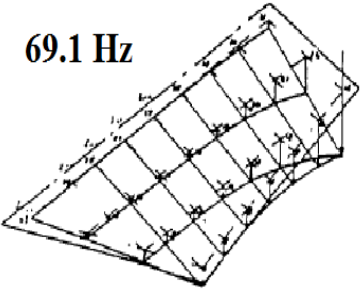
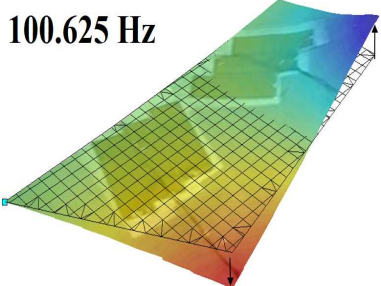
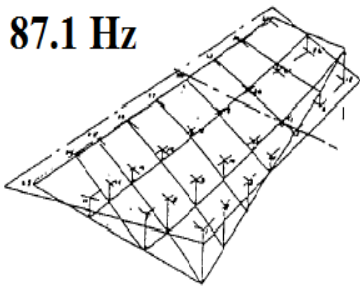
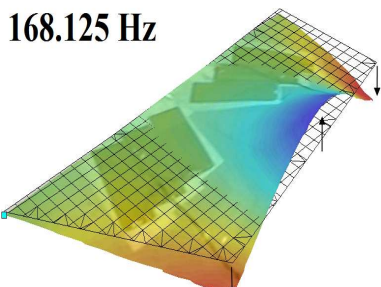
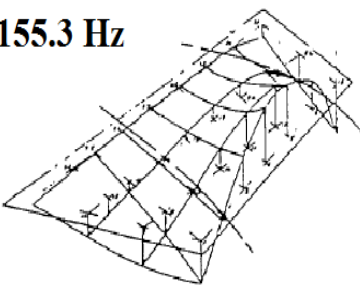
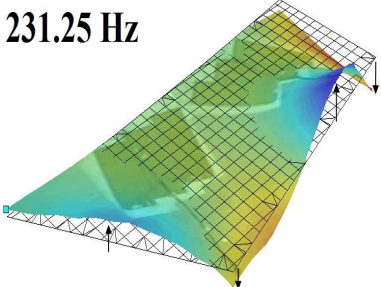
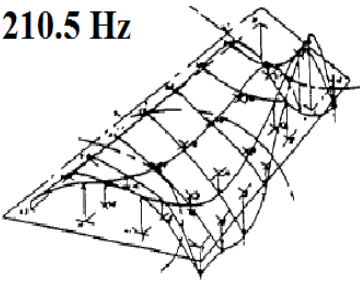
Table 4.3: Ventral Fin Test Article Natural Frequency Comparison

Mode Number and Name	FEM Frequency (Hz) [7]	ALC Flight Test Frequency (Hz) [34]	Laser Vibrometer Measured Frequency (Hz)
Mode 1: 1st Symmetric	69.1	78.0	78.1
Mode 2: 1st Anti-Symmetric	88.6	94.0	100.6
Mode 3: 2nd Symmetric	140.6	167.0	168.1
Mode 4: 2nd Anti-Symmetric	208.2	233.0	231.3

4.3 Experimental Determination of the Principle Strain Vectors

As explained in Chapter III, piezoelectric actuator and sensor fibers must be aligned with the principle strain vectors of the mode of interest for the highest probability of success. A scanning laser vibrometer was used to verify the orientation of the principle strain vectors on the surface of the ventral fin the same way as described in the previous section. The laser was programmed to take measurements at each point along a grid, shown in Figure 4.5, over the areas defined as the location of maximum strain energy for mode 1 and 2. Again, an electromagnetic shaker provided the excitation. Velocity magnitude information, which was equivalent to displacement magnitude as discussed in Chapter III, from each grid point was used to compute strain according to Equation 3.2. Principle strain magnitude and direction was then computed using Equations 3.3 and 3.4 where ε_a was strain along the 0° grid direction, ε_b was strain along the 45° grid direction, and ε_c was strain along the 90° grid direction. Figure 4.6 shows the experimentally determined principle strain vector fields which were no more than five degrees different than the FEM predictions. Note that the vector magnitudes are not drawn to scale in order to illustrate their directional relationship.

Table 4.4: Ventral Fin Mode Shapes

Mode	Laser Vibrometer	FEM Analysis [51]
1st Symmetric	<p data-bbox="574 436 711 485">78.125 Hz</p> 	<p data-bbox="1005 457 1117 499">69.1 Hz</p> 
1st Anti-symmetric	<p data-bbox="574 793 721 835">100.625 Hz</p> 	<p data-bbox="992 793 1122 835">87.1 Hz</p> 
2nd Symmetric	<p data-bbox="574 1140 721 1182">168.125 Hz</p> 	<p data-bbox="980 1140 1110 1182">155.3 Hz</p> 
2nd Anti-symmetric	<p data-bbox="574 1497 704 1539">231.25 Hz</p> 	<p data-bbox="987 1497 1117 1539">210.5 Hz</p> 

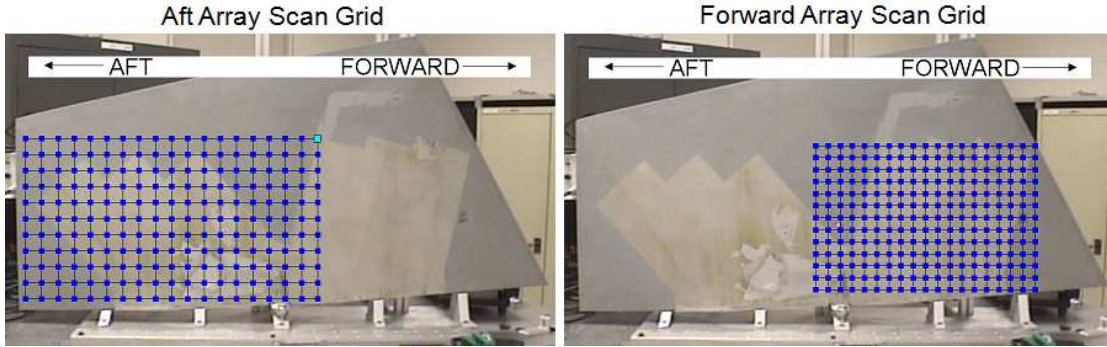


Figure 4.5: Laser Vibrometer Scan Pattern

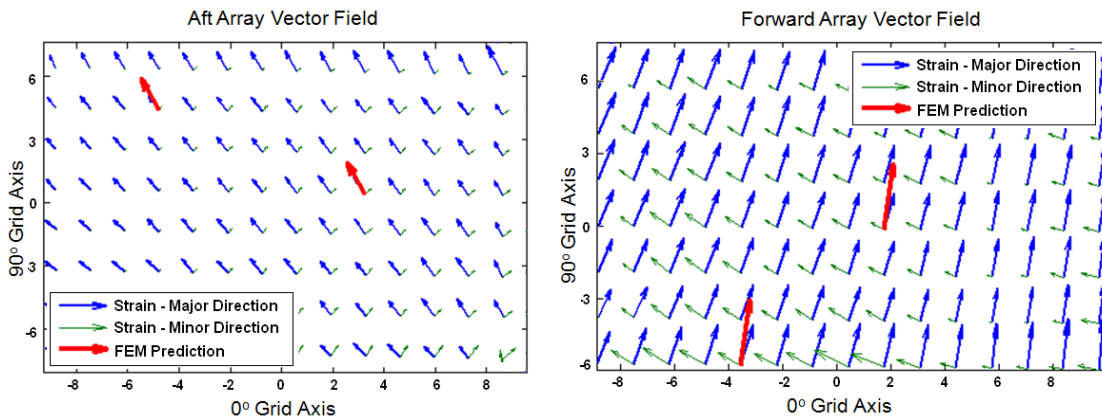


Figure 4.6: Principle Strain Vector Fields

4.4 Piezoelectric Actuators and Sensors Installation

The piezoelectric patches were installed using a surface vacuum bagging technique. First, the fin surface was stripped of paint and cleaned with a 5 percent phosphoric acid solution¹ and isopropyl alcohol. Next, the patch location and orientation was verified according to areas of maximum strain energy and experimentally determined principle strain vectors. Once oriented properly on the fin surface, a thin film of epoxy was applied to the fin and patches. Loctite[®] M-121HPTM Hysol[®], a high viscosity, no-sag two-part epoxy ideal for bonding dissimilar materials, was used due to its high impact resistance, high peel strength, and convenient low temperature cure. The next step involved layering vacuum bagging materials around the patches to provide an adequate seal and allow for the wicking of excess epoxy away from the

¹M-Prep Conditioner A from Vishay Micro-Measurements, Raleigh, North Carolina

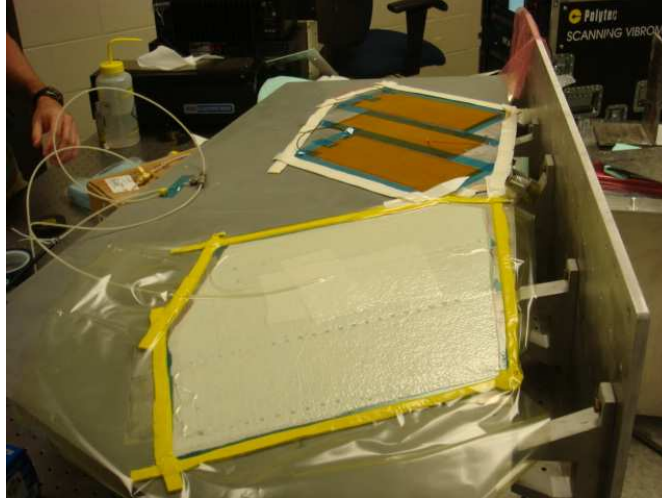


Figure 4.7: Piezoelectric Patch Installation Using Surface Vacuum Bagging

patches. The vacuum was maintained on the apparatus for the entire 24-hour cure time of the epoxy. Figures 4.7 and 4.8 show the installation process and the ventral fin with installed piezoelectric hardware, respectively.

4.5 Drive Amplifier Design

As stated in Chapter II, the primarily reactive load of piezoelectric actuators regenerates a significant amount of power to the driving amplifier and implies that the driving amplifier must be able to handle considerably higher voltages and circulating currents than suggested by the real power requirements of the actuators. Thus, a switching amplifier topology was chosen because of its ability to recover stored energy with minimal circuit noise. Since a suitable off-the-shelf switching amplifier was not available, a custom amplifier was designed and built.

The primary consideration for the amplifier design was power efficiency. A switching topology, also known as a ‘Class-D’ amplifier, was chosen for its characteristically low heat dissipation stemming from the use of fully ‘on’ or fully ‘off’ output transistors. The output stage of a Class-D amplifier can be a half- or full-bridge design which typically employs Metal-Oxide-Semiconductor Field Effect Transistors (MOSFET) or an Isolated Gate Bipolar Transistors (IGBT). The more stable full-bridge

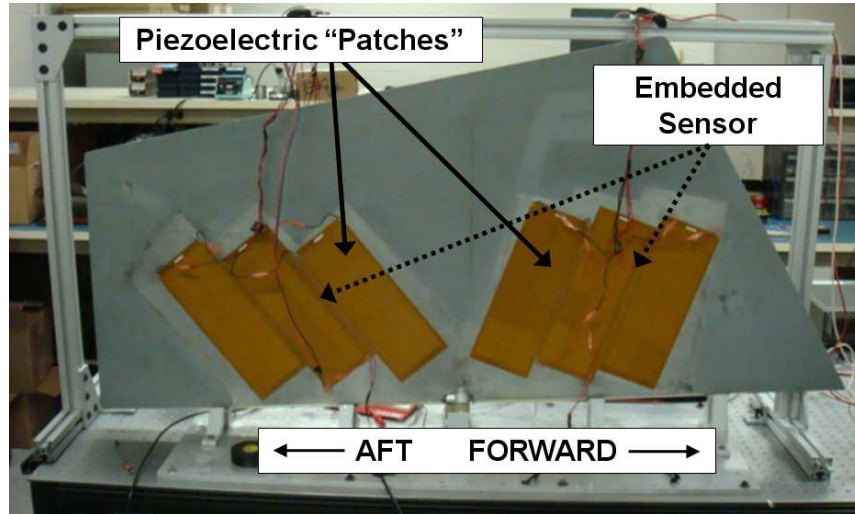


Figure 4.8: Piezoelectric Patches Installed on the Ventral Fin, AFIT Laboratory

design using IGBT's, summarized in Figure 2.5, was used in this design. Off-the-shelf Semikron driver circuits were used to control circuit switching but required pulse width modulated (PWM) drive signals; therefore, additional circuitry was developed to convert the analog control signal from the digital controller to a suitable PWM signal. The PWM generation was accomplished by comparing a 20 kHz triangle waveform, the 'switching' portion of the amplifier, to the analog input signal. An electromagnetic interference (EMI) filter was added to the power input stage to offset circuit noise caused by the 20 kHz switching frequency or other sources.

The MFC piezoelectric actuators used in this research were capable of +1500 to -500 volts. To simplify the control algorithm and drive amplifier design, the actuators were limited to ± 500 volts. Because the system was flight tested on an F-16D aircraft, the amplifier was made compatible with 28 volt DC (18VDC - 32VDC range) aircraft power and able to operate up to a load factor (G) of 6 G up to 30,000 feet pressure altitude. Analog inputs from the cRIO digital controller used to drive the amplifier output were specified at ± 5 volt DC.

Each 12 by 4 inch piezoelectric actuator possessed a nominal capacitance of 0.216uF at 100 Hz as seen by the amplifier output stage. Each actuator array, for-

ward and aft, were comprised of six total actuators wired in parallel resulting in an estimated 1.3 μF capacitance. DC bus ‘fill’ capacitors rated at ten times the piezoelectric load were used to complete the circuit. The amplifier was rated at twice the aircraft DC bus voltage to enhance system robustness. The entire amplifier assembly included two individual switching amplifier circuits allowing for independent control of each piezoelectric array on the ventral fin. The block diagram for the entire amplifier is shown in Figure 4.9. The frequency response for one channel shown in Figure 4.10 illustrates the 400 Hz bandwidth and natural resonance at 300 Hz in each amplifier.

Of the four piezoelectric sensors installed on the ventral fin, only two were used for feedback control. The remaining two were used for data collection and analysis. Nevertheless, each sensor signal input to the amplifier assembly were conditioned by anti-alias filters comprised of analog butterworth filters prior to being output to the digital controller and outside data recording hardware. Due to phase lag problems encountered with the digital control input/output modules, the cutoff frequency for the butterworth filters was set at 7.0 kHz to enhance phase properties of the drive amplifier near the frequencies of interest (50-200 Hz). An adjustable attenuation circuit was also designed to enable the selection of a range of feedback gains for the piezoelectric sensor signals prior to output from the amplifier assembly to the digital controller. These levels could be adjusted to ensure the sensor signal was kept at maximum sensitive during testing. Table 4.5 lists the specifications for each sensor signal output from the amplifier assembly and Figure 4.11 illustrates the adjustable attenuation circuit design. Note that an additional attenuation was added to the circuit following initial flight testing as discussed in Chapter V. The attenuation values listed in Table 4.5 and Figure 4.11 include the modification. The amplifier electronics also incorporated bit selectable system operation commands that controlled the power state of the high voltage convertors and PWM driver circuits. The completed amplifier assembly is shown in Figure 4.12.

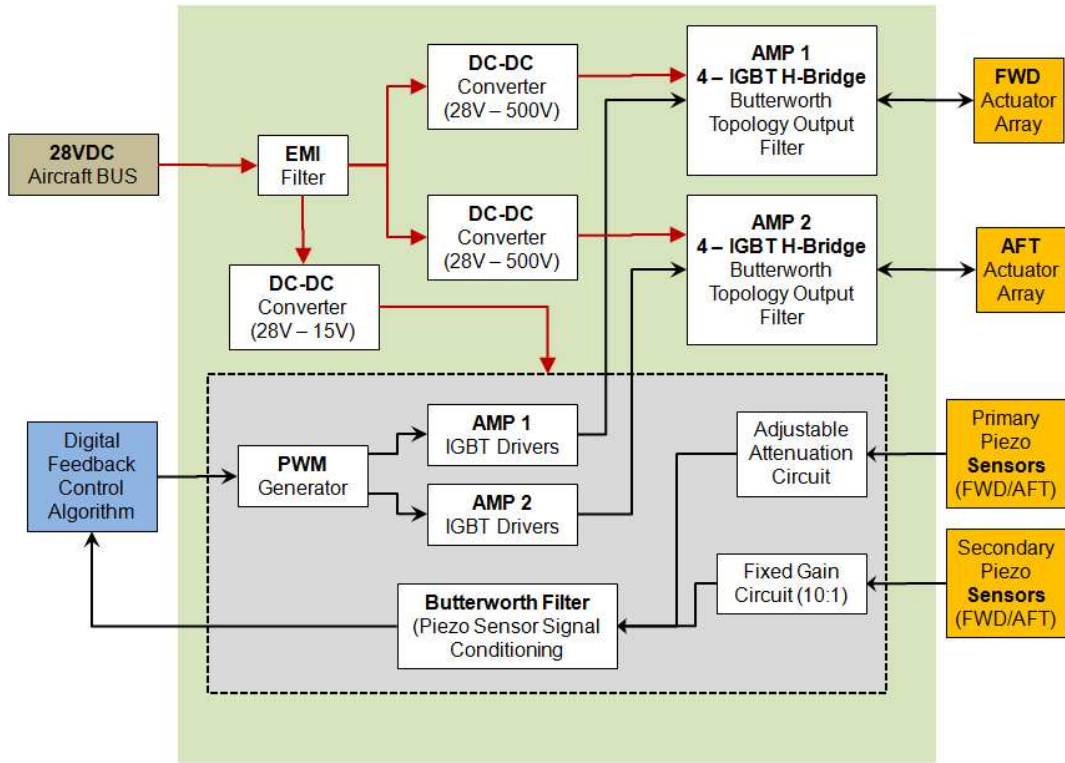


Figure 4.9: Piezoelectric Drive Amplifier Schematic (Simplified)

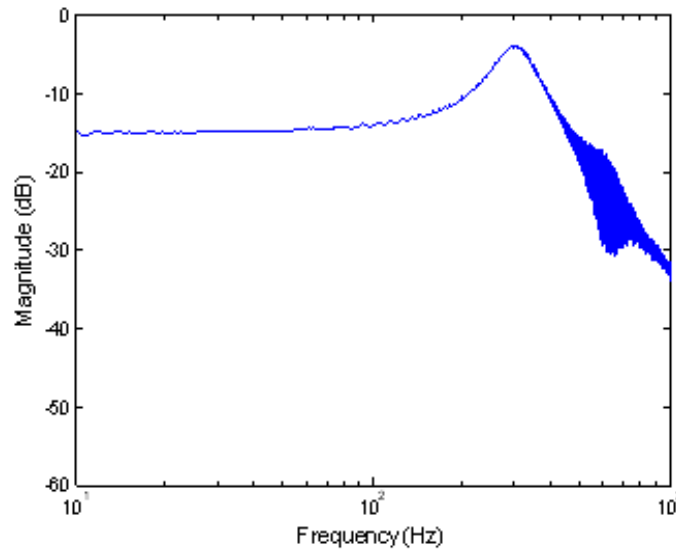


Figure 4.10: Piezoelectric Drive Amplifier Transfer Function

Table 4.5: Piezoelectric Sensor Output Configuration

Sensor	Sensor Location	Purpose	Signal Description
1	Forward Array Inboard Fin Surface	Feedback to digital controller for the forward amplifier	$\pm 10V$ Adjustable Attenuation ¹
2	Aft Array Inboard Fin Surface	Feedback to digital controller for the aft amplifier	$\pm 10V$ Adjustable Attenuation ¹
3	Forward Array Outboard Fin Surface	Data recording/ redundancy	$\pm 5V$ 15:1 Attenuation
4	Aft Array Outboard Fin Surface	Data recording/ redundancy	$\pm 5V$ 15:1 Attenuation

¹ 11:1 to 4.18:1 attenuation levels in 16 discrete increments were available in the adjustable attenuation circuit

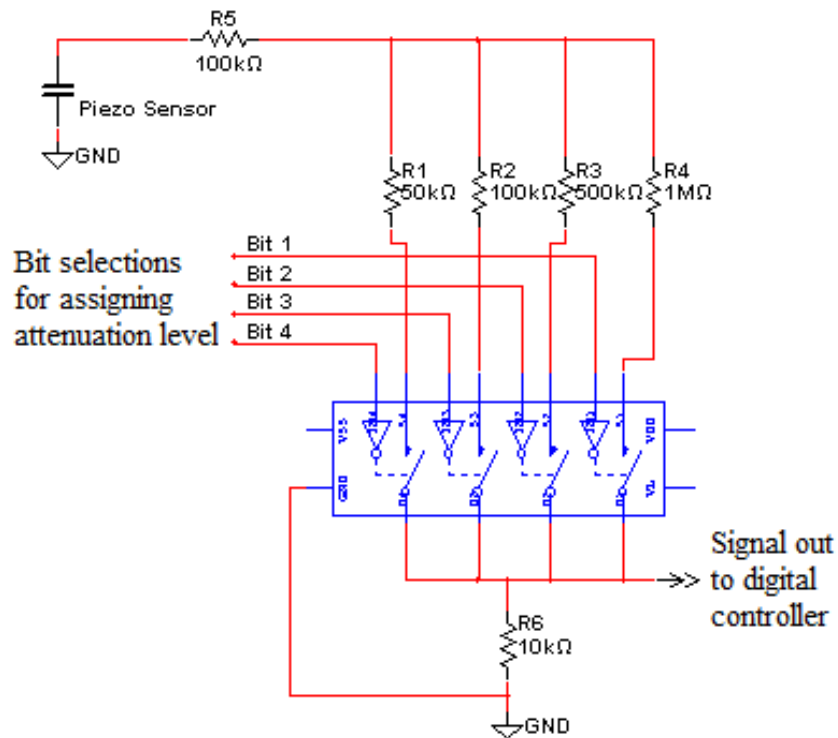


Figure 4.11: Bit-Selectable Adjustable Attenuation Circuit



Figure 4.12: Amplifier Assembly

4.6 *Transfer Function Model Realization*

An accurate system model was needed to develop effective control algorithms. First, the system was described according to the block diagram in Figure 4.13. The input $U(s)$, introduced in Figure 3.7, equals zero in Figure 4.13 and was included for completeness for the calculation of the plant, $P(s)$. Thus, the compensator and plant components of the block diagram can be put in terms of the closed-loop transfer function

$$\frac{Y(s)}{U(s)} = \frac{P(s)}{1 + P(s)G(s)} \quad (4.2)$$

where $G(s)$ was the digital control unit including its D/A and A/D functions and the control law coded in the cRIO and $P(s)$ was the plant including the drive amplifier, the ventral fin with installed piezoelectric hardware, and the signal conditioning electronics housed in the amplifier assembly. Defining the system in this way separated the digital controller from the rest of the system simplifying experimental determination of the transfer function for the plant, $P(s)$.

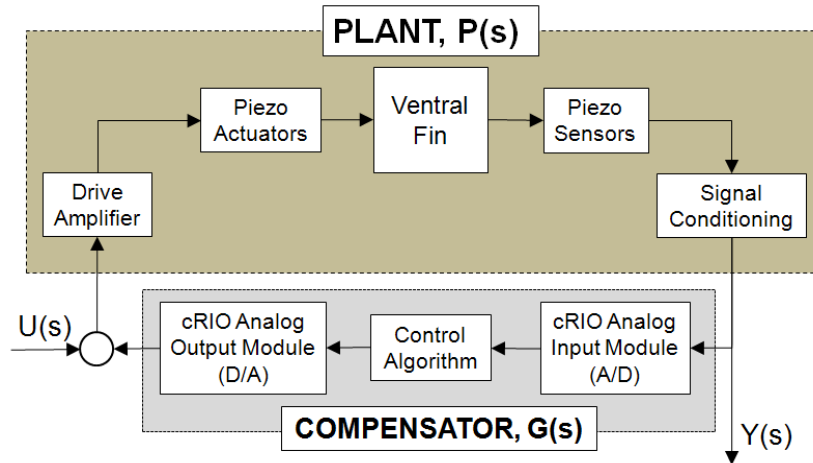


Figure 4.13: System Block Diagram

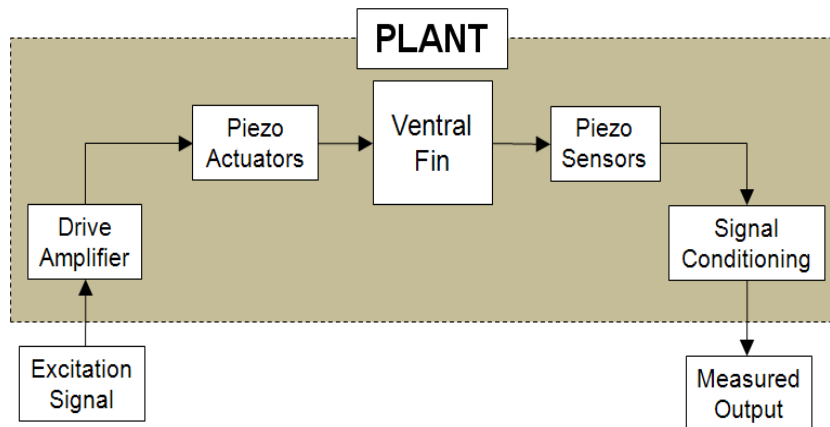


Figure 4.14: Open-Loop Block Diagram

Because two piezoelectric actuator arrays were designed to independently target a separate vibration mode, two transfer functions were needed: one for the forward array and the other for the aft array. In each case, a periodic chirp excitation signal was input to the amplifier to drive the actuators and the output was measured from the same array's piezoelectric sensors as illustrated in Figure 4.14. The magnitude response of each transfer function are shown in Figures 4.15 and 4.16. Note the presence of alternating poles and zeros indicative of a collocated system.

The transfer function data was then imported into the MATLABTM ERA Toolbox developed by Cobb [11] for state-space model identification from frequency re-

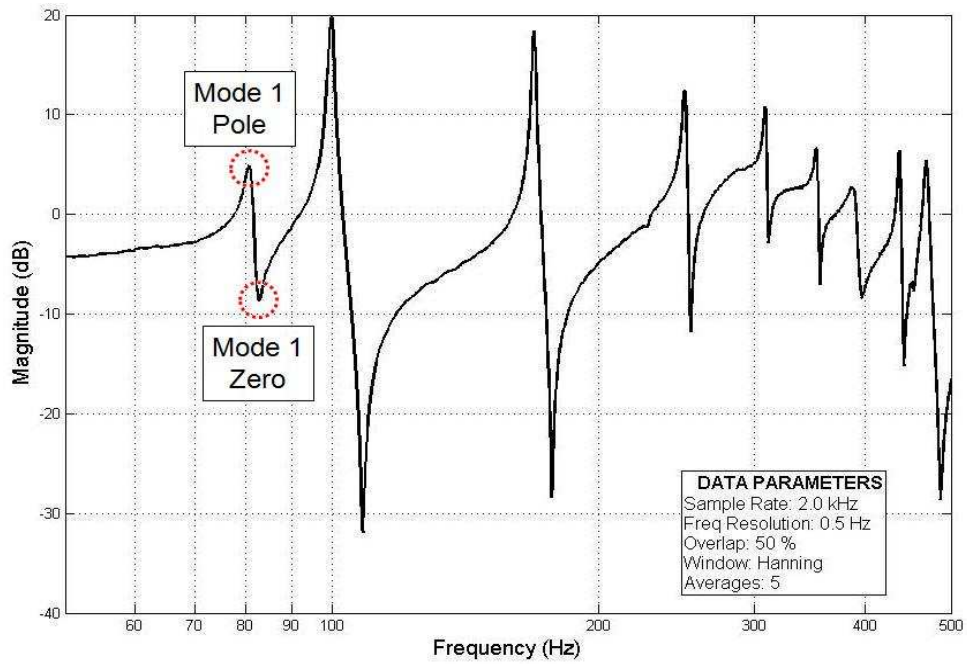


Figure 4.15: Forward Array Open-Loop Frequency Response, AFIT Laboratory

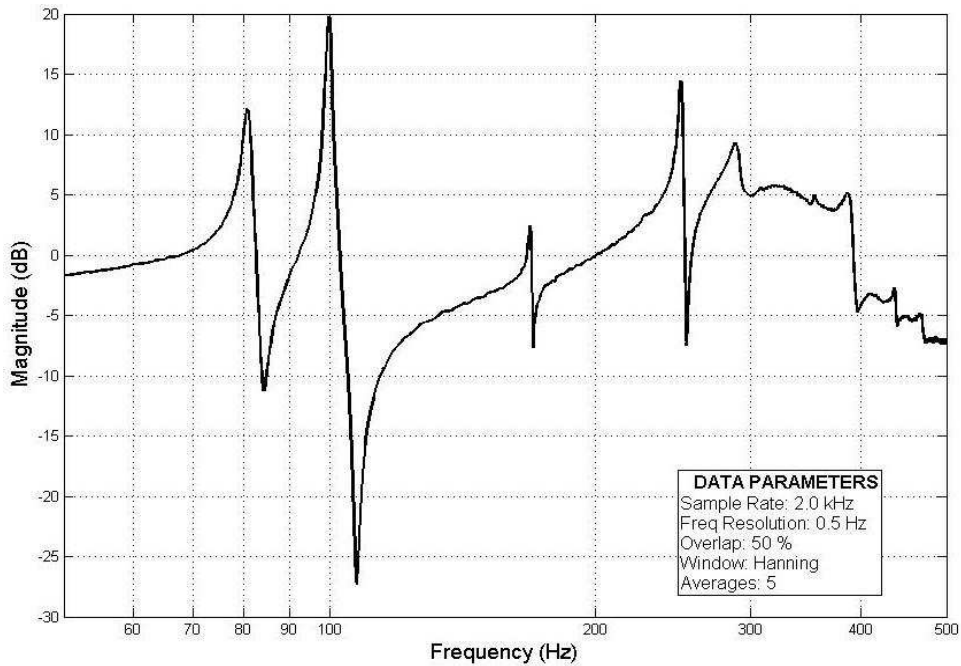


Figure 4.16: Aft Array Open-Loop Frequency Response, AFIT Laboratory

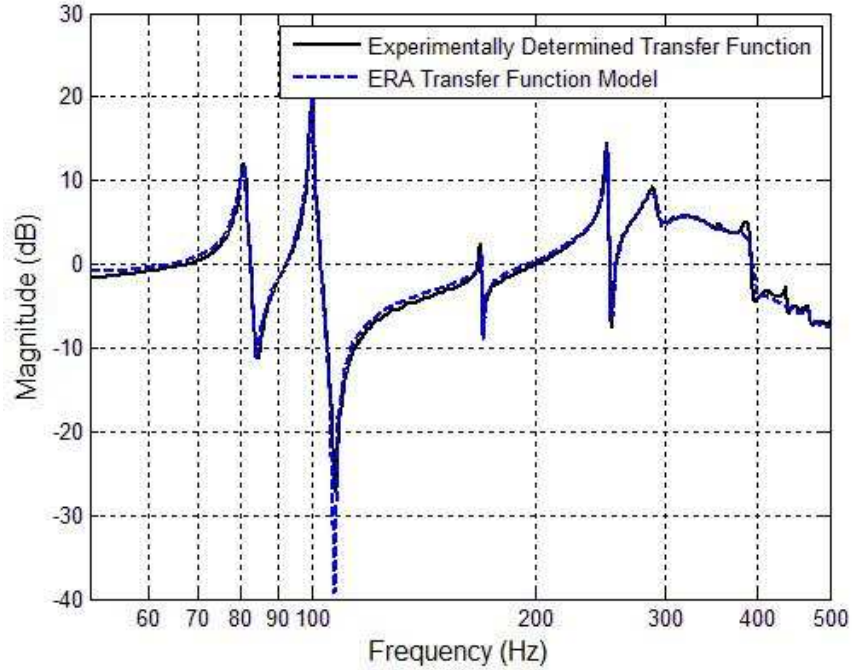


Figure 4.17: Experimental and ERA Model Transfer Function Comparison, Aft Array

sponse data. The ERA toolbox, which used the formulation of the ERA presented in Chapter III, was used to generate up to a 30 state, single-input single-output continuous state-space model for each array's transfer function. This state-space model, compared with an experimentally measured transfer function in Figure 4.17, provided an accurate model for the development of control algorithms.

4.7 Closed-Loop Control Development and Optimization

Control algorithm development and optimization was accomplished in two steps: MATLABTM simulation and laboratory bench testing. The design goals during these steps included maximum peak magnitude reduction of the vibration modes of interest and closed-loop stability with at least 6 dB of gain margin and 45 degrees or 10 milliseconds of phase or delay margin, respectively. The delay margin specification was based on the capabilities of the cRIO digital controller. If during control algorithm development the 45 degree phase margin was not obtainable at all frequencies, the

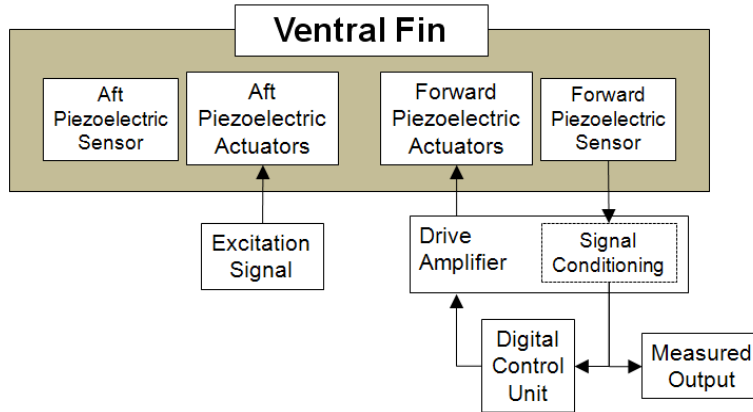


Figure 4.18: Bench Test Setup for Closed-Loop Performance, AFIT Laboratory

delay margin specification would be used in order to meet performance objectives. A frequency magnitude response, like that of a Bode plot, was used to assess peak magnitude reduction and a Nichols chart was used to assess closed-loop stability.

During the MATLABTM simulations, the closed-loop response using the state-space model defining the system plant as described in the previous section and the control algorithm was evaluated against the design goals. Laboratory bench testing followed with the verification of simulation results and refinement of the controller characteristics. Laboratory bench testing used all system hardware including the amplifier, instrumented ventral fin, and digital control unit. The software application SignalCalc 730² was used as a signal generator for the excitation source and signal analysis tool. When the forward piezoelectric array was bench tested, for example, the aft array actuators were used to excite the ventral fin, and vice versa, instead of the electromagnetic shaker. Figure 4.18 shows the laboratory bench test setup for the forward piezoelectric array.

4.7.1 Positive Position Feedback. Positive position feedback control development consisted of selecting the frequency ω_c and damping ratio ζ_c of the second-order filter in Equation 3.19 that generated the desired closed-loop response. To begin, the

²Data Physics Corporation, San Jose, California

frequency of the filter was matched with the measured natural frequency of the vibration mode of interest. The damping ratio, however, was selected as a tradeoff between compensator robustness, low frequency mode flexibility, and target mode damping effectiveness. Consequently, damping ratio selection became a trial-and-error process in order to achieve the design goals. As stated in Chapter III, PPF controllers carry several characteristics that complicate design. First, PPF controllers perform best when modes are well separated, especially those modes of higher frequency than the target. Second, an increase in flexibility occurs for modes of lower frequency than the target. These two factors significantly influenced the selection of damping ratio because the first four modes were relatively close together in frequency.

Multiple PPF filters can also be placed in parallel to effect multiple modes simultaneously [19, 42, 49]. Doing so retains the second-order qualities of a single PPF filter while effectively increasing the region of active damping without losing effectiveness at the target frequencies. The same design considerations apply to the multi-modal case as to the single-mode filter, that is, frequency and damping ratio selection.

4.7.2 Linear Quadratic Gaussian. The development of an LQG compensator was less intuitive and relied more on simulations to find an appropriate control law. As presented in Chapter III, construction of the LQG compensator can be separated into the Linear Quadratic Regulator and a Kalman filter. Still, the LQG compensator relied on the accuracy of the system model developed from the Eigenstructure realization algorithm, which, during this research, consisted of up to 30 states. A compensator of the same size can be computationally cumbersome to a digital controller. Therefore, it became necessary to reduce the order of the compensator.

The LQR was tailored to effect a specific set of modes of the system. To appropriately weight each mode in the specification of the state weighting matrix, Q , a modal form of the system model was required. Fortunately, Cobb's ERA Toolbox

utility for MATLABTM [11] could output a state-space model of the system in block diagonal form making the identification of specific modes within the system matrices much easier. Customizing the weighting matrix Q from Equation 3.24 resulted in a reduced LQR that targeted a smaller set of desired modes. Given that the closed-loop system was SISO, Equation 3.24 reduced to

$$J = \frac{1}{2} \int_0^{t_f} \left(\begin{bmatrix} x_1 & x_2 & \cdots & x_n \end{bmatrix} \begin{bmatrix} q_1 & 0 & \cdots & 0 \\ 0 & q_2 & \cdots & 0 \\ \vdots & \vdots & \ddots & \vdots \\ 0 & 0 & \cdots & q_n \end{bmatrix} \begin{bmatrix} x_1 \\ x_2 \\ \vdots \\ x_n \end{bmatrix} + u^2 r \right) dt \quad (4.3)$$

where q_n was the state weighting constant and the control penalty matrix R simplified to the constant r for the SISO case. Note that, for each mode, there were two states in the model; therefore, two state weighting constants pertained to each mode.

Considering the bandwidth and frequency response of the amplifier, which had a natural resonance at 300 Hz, the first three modes (up to 170 Hz) were included in the final LQG formulations for this research. That is, all state weighting constants that did not correspond to the poles and zeros of the first three modes of vibration were made zero. The constant r was arbitrarily set to 100 to penalize control input. The Kalman filter was specified by setting the noise covariance data for the measurement noise and disturbance input to unity. Figure 4.19 provides an example of a reduced order LQG compensator that targets the first three modes only, compared to a full order compensator where the state weighting matrix was set to the identity matrix of the original model size.

4.7.3 Digital Implementation. As mentioned, the larger the compensator order, the more cumbersome it becomes to the digital controller, especially when using the finite difference method presented in Chapter III. However, due to schedule constraints, the finite difference method of programming a discrete control law onto the FPGA of the cRIO control unit was the only method available. Implementing a

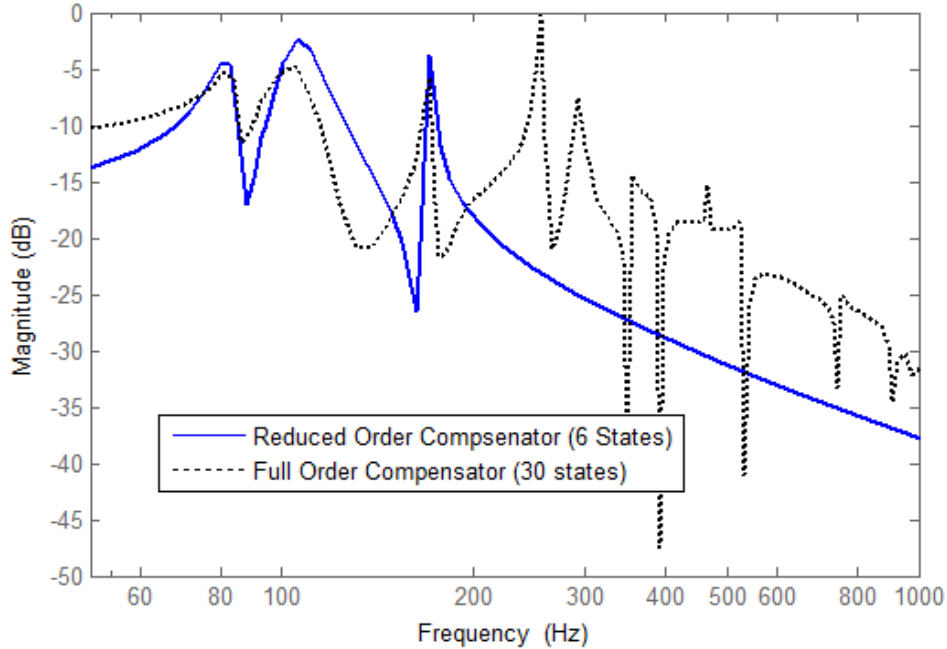


Figure 4.19: Full-State vs. Reduced-State LQG Compensator

second-order PPF discrete filter was not problematic. On the other hand, programming an LQG compensator proved more difficult.

It was determined that the smallest, most effective LQG compensator that included the first three modes of the ventral fin required an 8th order design. Extending an 8th order design with the finite difference method caused larger than expected numerical errors in the feedback loops of the FPGA code. Therefore, the LQG compensator was abandoned for use in the cRIO digital controller. Fortunately, the LQG designs could be bench tested in the laboratory using a dSPACE digital controller. These results are presented in Chapter V.

4.8 Aircraft Installation and Ground Testing

Once the control algorithms were optimized in the laboratory, the system hardware was validated for flight testing on an F-16D. It was then installed on the test aircraft, serial number 86-0050 Block 30 F-16D, at Edwards Air Force Base (AFB), and made ready for ground testing. All ground and flight testing of the ventral fin



Figure 4.20: Instrumented Ventral Fin Installed on the Test Aircraft, Edwards AFB

buffet alleviation system was accomplished as part of the ACTIVE FIN test management project at the USAF TPS. Figure 4.20 shows the instrumented Block 15 ventral fin used in laboratory testing painted and installed on the right fin station of the test aircraft.

The drive amplifier and cRIO digital control unit was installed in the ammo bay aft of the rear cockpit along the aircraft spine as shown in Figure 4.21. The existing data acquisition system (DAS) onboard the test aircraft was modified to record the piezoelectric sensor signals as well as system function parameters and flight condition data. A hand-held personal computer, OQO Model 02 configured with LabVIEWTM 8.6, was custom programmed and mounted in the rear cockpit as shown in Figure 4.22 to provide the aircrew with overall system control including the power state of each amplifier and the activity of each control law. A system diagram is provided in Figure 4.23. The aircrew could also command gain changes for each control law using the adjustable attenuation circuit housed in the amplifier assembly as part of the sensor feedback loop. Gain changes from 0 to -8.4 dB from the nominal level programmed in the digital controller were available.

Ground testing provided a benchmark for flight testing and was accomplished in three steps. First, system functionality was verified. Second, the transfer function of each piezoelectric array was measured and used in MATLABTM simulations to assess

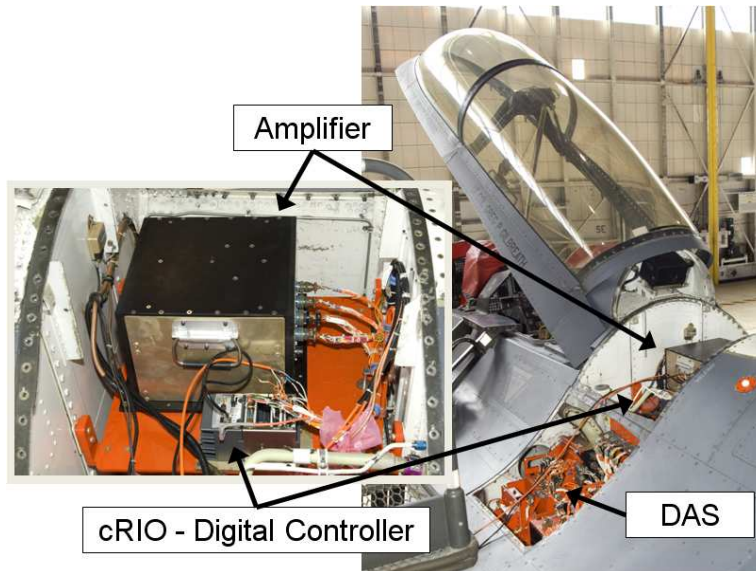


Figure 4.21: System Hardware Installed in the Ammo Bay of the Test Aircraft, Edwards AFB



Figure 4.22: OQO Handheld PC Mounted in Rear Cockpit, Edwards AFB

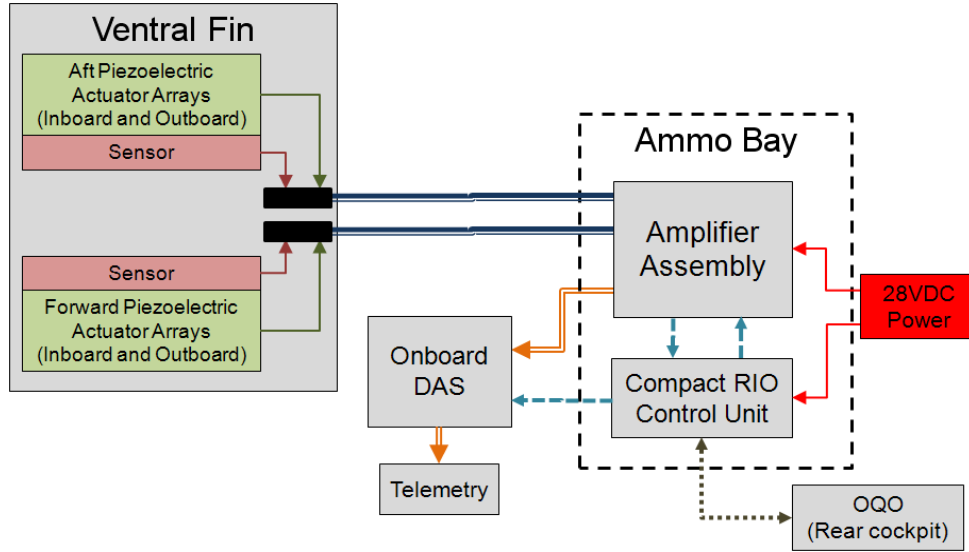


Figure 4.23: Test Aircraft System Diagram

stability and predict performance. Finally, closed-loop control of the actuator arrays was validated and optimized. Optimization occurred in much the same way as in the laboratory. For example, to assess the closed-loop performance and optimize the PPF control for the aft piezoelectric array, the forward array served to excite the fin using a periodic chirp excitation signal. The filter frequency, damping ratio, or gain could then be modified to meet the design goals.

Because the LQG algorithms could not be implemented in the cRIO digital controller, only PPF control algorithms were tested during the ACTIVE FIN project.

4.9 ACTIVE FIN Flight Testing

Flight testing of the F-16 ventral fin buffet alleviation system occurred from March 18 to April 1, 2009 as part of the ACTIVE FIN test project at the USAF TPS [4]. Flight test points were selected based on conclusions of the Aeroelastic Load Control [17] flight test project in 2005 which found the highest level of vibration in the transonic region (0.85 to 0.95 Mach) and high dynamic pressures. The ACTIVE FIN test point matrix, shown in Figure 4.24, was designed to target this area, while at

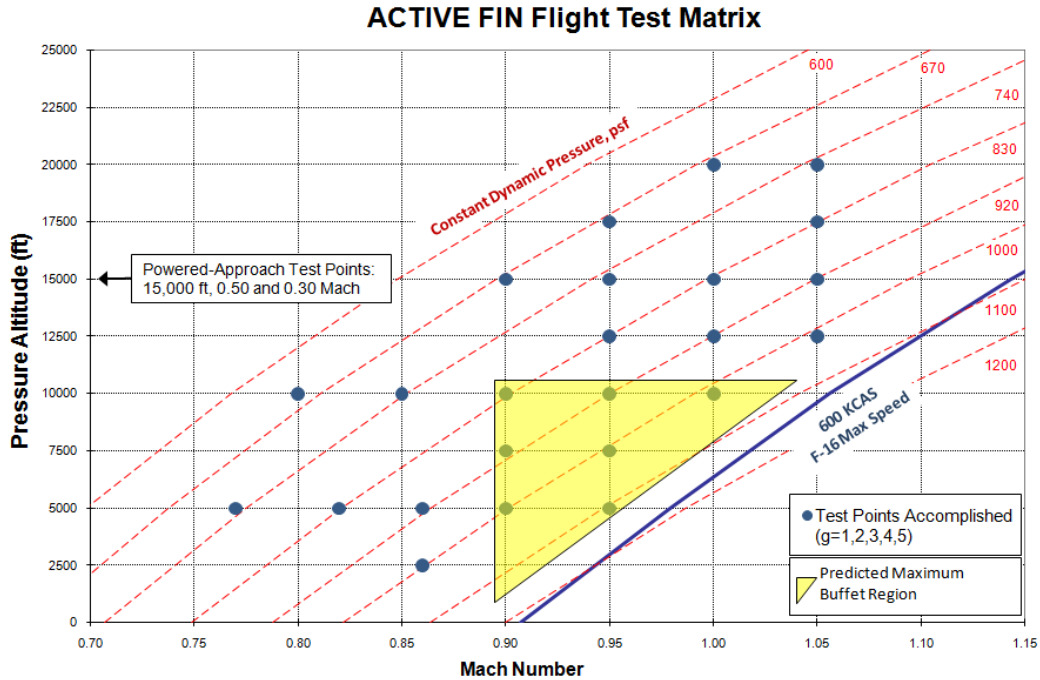


Figure 4.24: ACTIVE FIN Test Point Matrix [4]

the same time, isolating Mach number, dynamic pressure, and angle of attack (AOA) in order to assess their individual effects on ventral fin buffet.

Test points were flown at constant Mach number, constant altitude, and constant load factor. Figure 4.24 does not show variation in AOA that was accomplished at every point in the matrix by changing load factor from 1 to 5 G during constant speed, constant altitude turns. The test aircraft was configured with wing fuel tanks and a LANTIRN pod on station 5R directly upstream of the instrumented ventral fin. The LANTIRN pod was used because of its known influence on ventral fin buffet. Some test points were also flown with the landing gear down for reasons discussed later. A view of the aircraft in flight with the LANTIRN pod is shown in Figure 4.25.

Flight testing included two phases. Phase 1 consisted of open-loop tests to determine the baseline structural response of the ventral fin using real-time measurements from the piezoelectric sensors on the fin's surface. Power was not applied to the actuators during Phase 1. Data collected during Phase 1 were used to verify closed-loop stability predictions and control law suitability. Phase 2 evaluated the closed-loop

structural response where feedback control was activated in three different scenarios: forward array active, aft array active, and both arrays active simultaneously.

At least five seconds of stabilized data were collected at each test point and recorded by the onboard DAS at a sample rate of 6.9 kHz after being filtered by the signal conditioning circuit in the amplifier. For data processing efficiency and to control file size during post processing, the test data were re-sampled at 2.3 kHz by extracting every third data sample from the flight test recording prior to frequency spectrum analysis. Since the control algorithms were limited to vibration modes below 200 Hz, a Nyquist frequency of 1.15 kHz was adequate for data analysis.

Two measures of performance were obtained from flight data: mean vibration reduction and modal peak magnitude reduction. The mean vibration of the ventral fin was determined from the RMS voltage of a sensor during a data set from

$$V_{RMS} = \sqrt{\frac{1}{n} \sum_{i=1}^n V_i^2} \quad (4.4)$$

where n was the number of samples and V_i was the measured voltage of the piezo-electric sensor sample. Peak magnitude reduction was determined by comparing the open-loop and closed-loop frequency spectrum from the same flight condition. The MATLABTM *pwelch* algorithm, which follows Welch's averaged, modified periodogram power spectral estimation method, was used to estimate the frequency spectrum. The Welch method was chosen due to its favorable noise reduction characteristics over other estimation techniques. Parameters used in the frequency spectrum estimation are listed in Table 4.6. The number of averages and data segment length (a subset of the total data sample) was defined as a function of total sample size, frequency resolution, and overlap.

Table 4.6: Frequency Spectrum Estimation Parameters

Sample Frequency	2314.8 Hz
Frequency Resolution	0.5 to 1.0 Hz
Window	Hanning
Overlap	50% to 80%
Data Sample Size	> 5 seconds



Figure 4.25: Flight Test Configuration, Edwards AFB

V. Results and Analysis

This chapter presents the results of the research conducted in support of this thesis and is divided into three sections: laboratory simulations and bench testing, aircraft ground testing, and flight testing. Each section included three distinct activities: ventral fin frequency response estimation, control law optimization, and buffet alleviation performance assessment. The two control techniques evaluated in the laboratory were a positive position feedback and Linear Quadratic Gaussian compensator. Only the PPF algorithm was used during ground and flight testing due to programming limitations in the digital controller.

5.1 Laboratory Simulations and Bench Testing

The open-loop frequency response of the forward and aft arrays measured during laboratory testing are shown in Figures 4.15 and 4.16, respectively. System models generated from these transfer functions with ERA enabled the optimization of compensator designs using MATLABTM simulations. Candidates were selected from these simulations for bench testing based on performance and stability criteria discussed in Chapter IV. Laboratory bench testing incorporated all system hardware including the custom amplifier, digital control unit, and instrumented Block 15 ventral fin. The compensator designs were further optimized with additional simulations or bench testing, as needed.

5.1.1 Positive Position Feedback. During preliminary attempts at an effective PPF compensator, single filter elements were configured for each array with the filter frequency matched to the measured frequency of the mode of interest. The filter damping ratio, ζ_c , typically between 0.2 and 0.3 for PPF compensators [42], was initially set to 0.2. Simulations of compensators with these characteristics produced promising results for each array, listed as *trial 1* of Table 5.1. However, problems arose when these candidates were bench tested using the actual system hardware. For example, bench tests for aft array PPF compensators revealed that a filter element at the mode 1 frequency (78 Hz) could not produce closed-loop results that

met stability margin goals due to control spillover from mode 2. The spillover was caused by a decrease in damping in the mode 2 response due to the small spacing between mode 1 and mode 2 frequencies, which, when coupled with the larger mode 2 open-loop response compared to mode 1, as shown in Figure 4.16, made the otherwise favorable magnitude roll-off quantities of the PPF filter ineffective.

Fanson [19] recommended a method for performance recovery when modes were closely spaced by altering the closed-loop zeros or poles changing the root locus. According to Equation 3.19, the PPF filter elements contained no zeros. Changing the plant zeros meant moving the physical location of the sensors, which would affect the collocated properties of the system. Thus, in subsequent simulations, the filter frequency was increased altering the filter poles and, consequently, the closed-loop root locus. As an additional measure, filter damping was decreased in order to shrink the range of active damping and to direct filter effectiveness at a single vibration mode in the fin. These changes incorporated in the forward array PPF filter targeting mode 2 produced better results indicated as *trial 2* of Table 5.1. The same changes improved the aft array PPF control during simulations, but subsequent bench testing proved that neither technique solved the instability problems. Therefore, a single filter element targeting mode 1 was abandoned for the aft array. Instead, a single filter element targeting mode 2 was designed and optimized in simulation and was effective during bench testing in reducing mode 2 vibrations, listed as *trial 3* of Table 5.1.

A compensator consisting of three PPF filters placed in parallel was attempted for each array, listed as *trial 4* in Table 5.1, in an attempt to reduce vibration in multiple modes simultaneously. Three parallel filters for modes 1, 2, and 3 configured for the forward array effectively attenuated the response of those modes. However, a single filter element remained the best candidate for the aft array. The compensators that produced the best results during bench testing are shown in Figures 5.3 and 5.4. Bench test results using these PPF compensators are shown in Figure 5.1.

5.1.2 Linear Quadratic Gaussian. Simulations and bench tests were also accomplished for LQG designs. The first three modes of the ventral fin were included in LQG compensator designs by making the state weighting constants in the state weighting matrix equal to 1 for those modes. The control penalty constant was set as 100. Effort was made to adjust the state weighting constants for each mode to optimize performance during simulations and bench testing, but peak reduction did not improve as to warrant further investigation. Thus, for simplicity, the state weighting constants were kept equal to 1. The noise covariance data for the Kalman filter design was not changed during optimizations and were also kept equal to 1. The compensators that produced the best results during bench testing are shown in Figures 5.5 and 5.6. Bench test results using these LQG compensators are shown in Figure 5.2. It is important to note that bench testing the LQG compensators was accomplished using a MATLABTM based digital controller not fit for flight testing. Therefore, bench test results listed in Table 5.2 do not account for the cRIO digital controller interface.

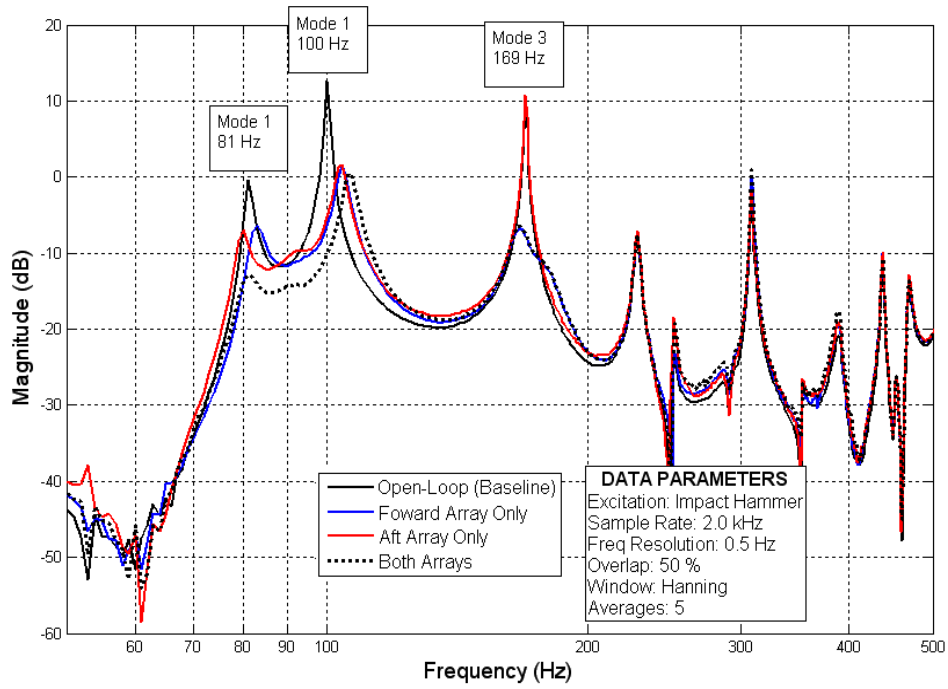


Figure 5.1: PPF Bench Test Results

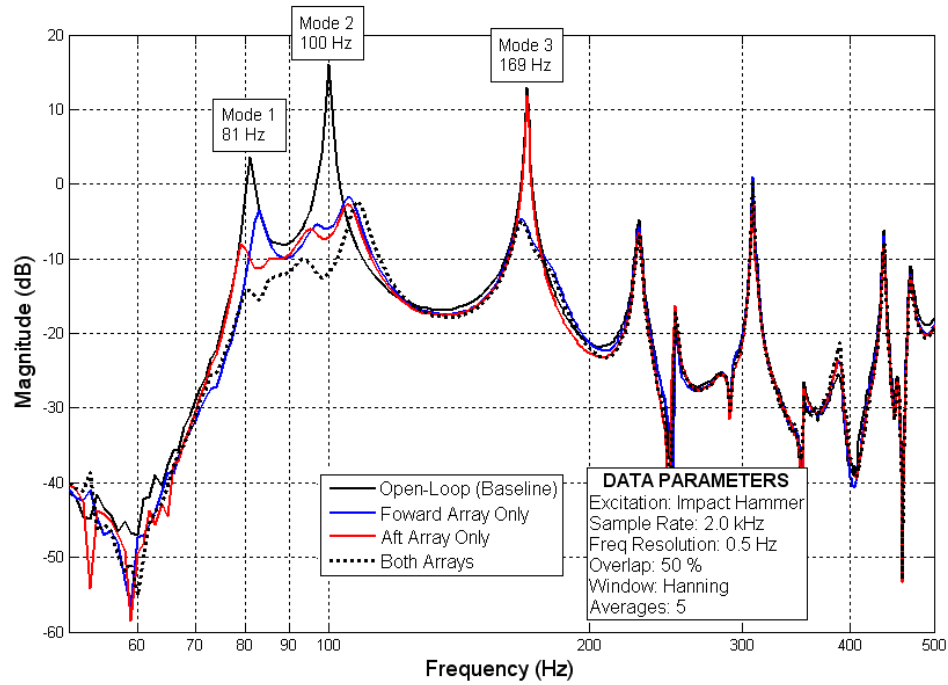


Figure 5.2: LQG Bench Test Results

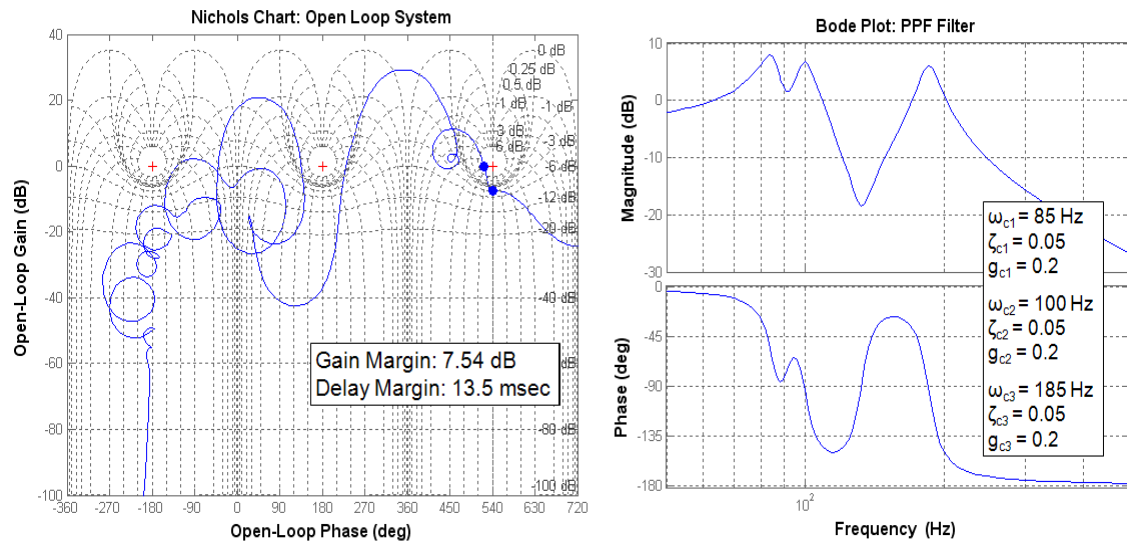


Figure 5.3: Forward Array PPF Design

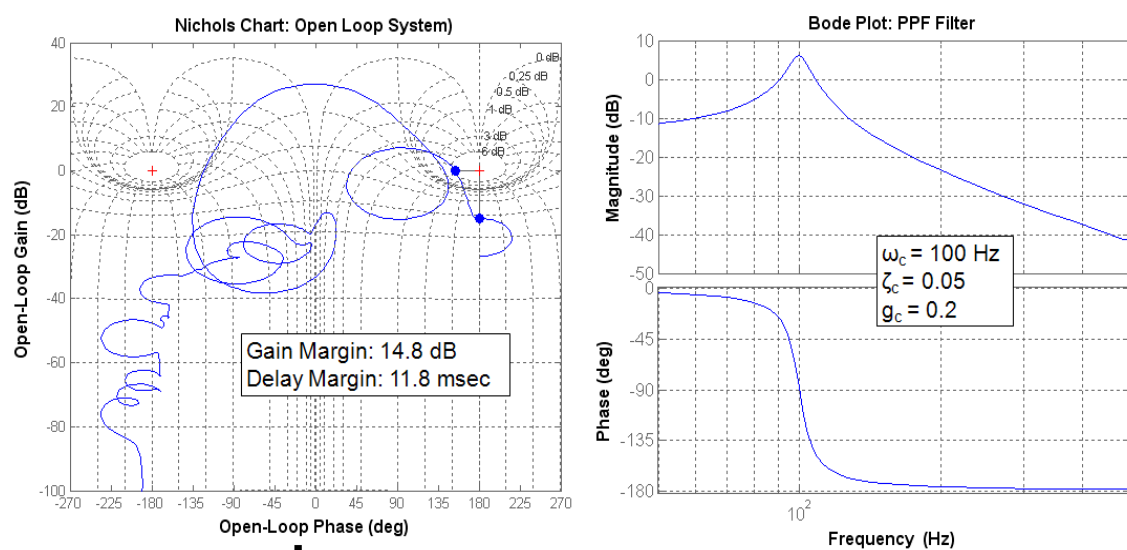


Figure 5.4: Aft Array PPF Design

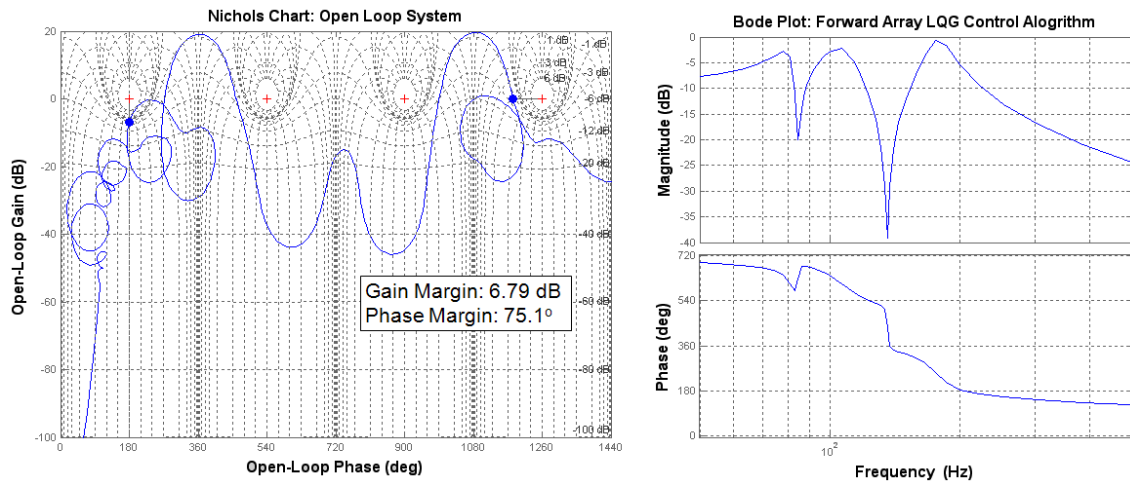


Figure 5.5: Forward Array LQG Design

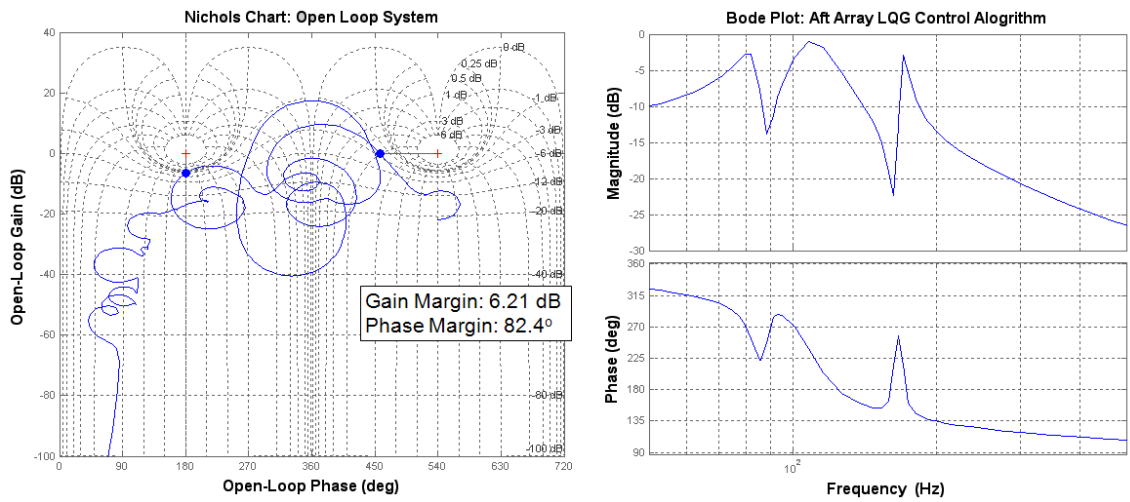


Figure 5.6: Aft Array LQG Design

Aft Array Positive Position Feedback Laboratory Optimization

Trial	Test*	Filter Characteristics			Performance ¹			Estimated Stability		
		[Filter Frequency (Hz), Filter Damping, Scalar Gain]	Filter 1	Filter 2	Filter 3	Mode 1	Mode 2	Mode 3	Gain Margin (dB)	Phase Margin (degrees)
1	Sim	78, 0.20, 0.38	-	-	-	7	5	-	9.3	45.8
2	Sim	78, 0.05, 0.10	-	-	-	8	-3	-	20.7	44.2
2	Sim	85, 0.20, 0.47	-	-	-	8	15	-	7.4	46.1
2	Sim	85, 0.05, 0.07	-	-	-	-30	-6	-	23.9	45.0
3	Sim	-	96, 0.20, 0.37	-	-	-12	18	2	9.4	46.6
3	Sim	-	96, 0.05, 0.10	-	-	2	17	-	20.8	46.2
3	Sim	-	100, 0.20, 0.35	-	-	-10	20	-	10.0	45.5
3	Sim	-	100, 0.05, 0.12	-	-	3	23	-	19.3	44.5
3	Bench	-	100, 0.05, 0.12	-	-	6	12	-	19.3	44.5
3	Bench	-	100, 0.05, 0.20	-	-	9	14	5	14.8	11.8 msec
4	Sim	85, 0.05, 0.05	100, 0.05, 0.05	185, 0.05, 0.05	185, 0.05, 0.05	5	15	5	18.8	43.7

Table 5.1: Positive Position Feedback Laboratory Optimization

Forward Array Positive Position Feedback Laboratory Optimization

Trial	Test*	Filter Characteristics			Performance ¹			Estimated Stability		
		[Filter Frequency (Hz), Filter Damping, Scalar Gain]	Filter 1	Filter 2	Filter 3	Mode 1	Mode 2	Mode 3	Gain Margin (dB)	Phase Margin (degrees)
1	Sim	-	96, 0.20, 0.34	-	-	2	17	6	12.4	45.6
2	Sim	-	96, 0.05, 0.09	-	-	2	17	7	24.5	44.2
2	Sim	-	100, 0.20, 0.31	-	-	2	19	10	13.2	46.2
2	Sim	-	100, 0.05, 0.14	-	-	3	25	3	20.5	45.6
4	Sim	85, 0.05, 0.08	100, 0.05, 0.08	185, 0.05, 0.08	185, 0.05, 0.08	6	20	15	15.9	45.1
4	Bench	85, 0.05, 0.10	100, 0.05, 0.10	185, 0.05, 0.10	185, 0.05, 0.10	6	11	16	13.6	11.6 msec
4	Bench	85, 0.05, 0.20	100, 0.05, 0.20	185, 0.05, 0.20	185, 0.05, 0.20	15	14	18	7.5	13.5 msec

* Sim = MATLABTM simulations using ERA system models

* Bench = Laboratory bench testing with all system hardware

¹ Performance during simulations was estimated, performance during bench testing was measured

Table 5.2: Linear Quadratic Gaussian Laboratory Optimization

Linear Quadratic Gaussian Laboratory Optimization

Test*	Actuator Array	Scalar Gain	LQG Characteristics			Performance ¹			Estimated Stability	
			State Weighting Constants (q_1, q_2, q_3)	Control Penalty Constant (r)	Peak Reduction (dB)	Mode 1	Mode 2	Mode 3	Gain Margin (dB)	Phase Margin (degrees)
Sim	Aft	1.9	1	100	6	17	-	6.2	82.4	
Bench	Aft	1.5	1	100	4	13	2	7.8	83.7	
Sim	Forward	2.2	1	100	3	20	17	6.8	75.6	
Bench	Forward	1.5	1	100	3	15	11	7.9	78.1	

* Sim = MATLABTM simulations using ERA system models

* Bench = Laboratory bench testing with all system hardware

¹ Performance during simulations was estimated, performance during bench testing was measured

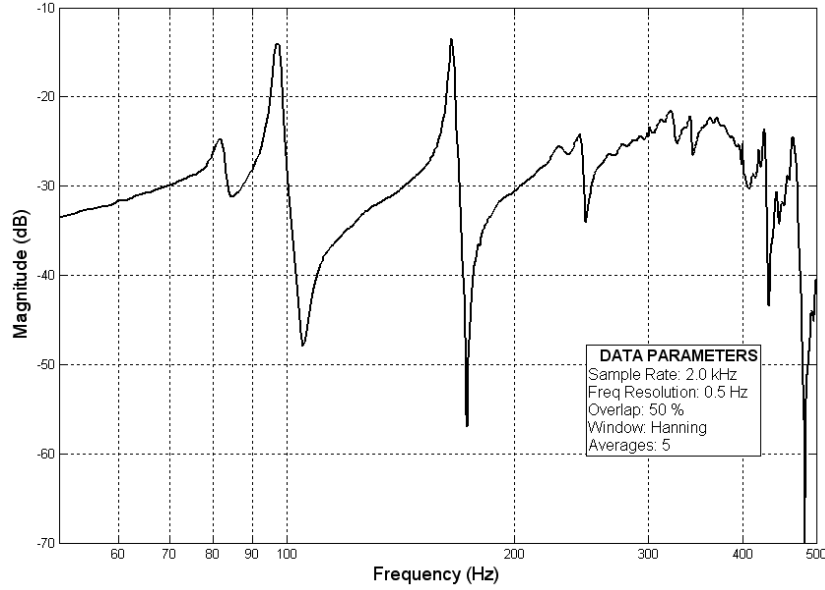


Figure 5.7: Forward Array Frequency Response, Ground Testing

5.2 Aircraft Ground Testing

The buffet alleviation system was ground tested at Edwards AFB once all hardware was installed on the test aircraft. Since the digital controller was limited to second-order finite difference formulations, only PPF algorithms were used during ground and flight testing. The first step during ground testing involved verifying the frequency response of the ventral fin. This was accomplished in the same manner as done during laboratory testing according to Figure 4.14. The open-loop frequency response of the forward and aft arrays, shown in Figures 5.7 and 5.8, respectively, reveal that modal frequencies were nearly identical to laboratory measurements. Thus, the controllers developed in the lab could be ground tested with confidence.

Each actuator array configured with PPF controllers selected from laboratory bench testing were evaluated independently. The tests revealed a peak magnitude reduction of 14 dB in mode 2 for each array and 8 dB in mode 3 for the forward array. Open and closed-loop responses are shown in Figures 5.9 and 5.10.

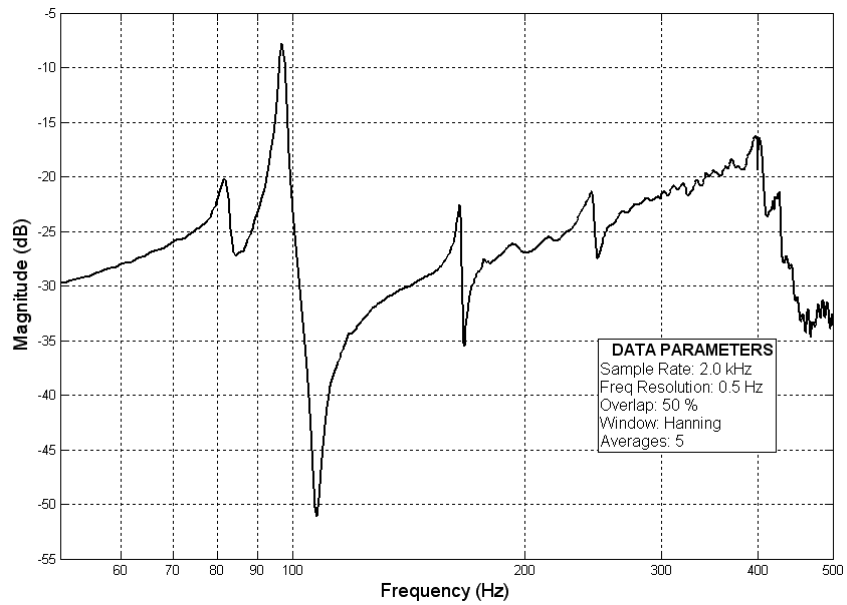


Figure 5.8: Aft Array Frequency Response, Ground Testing

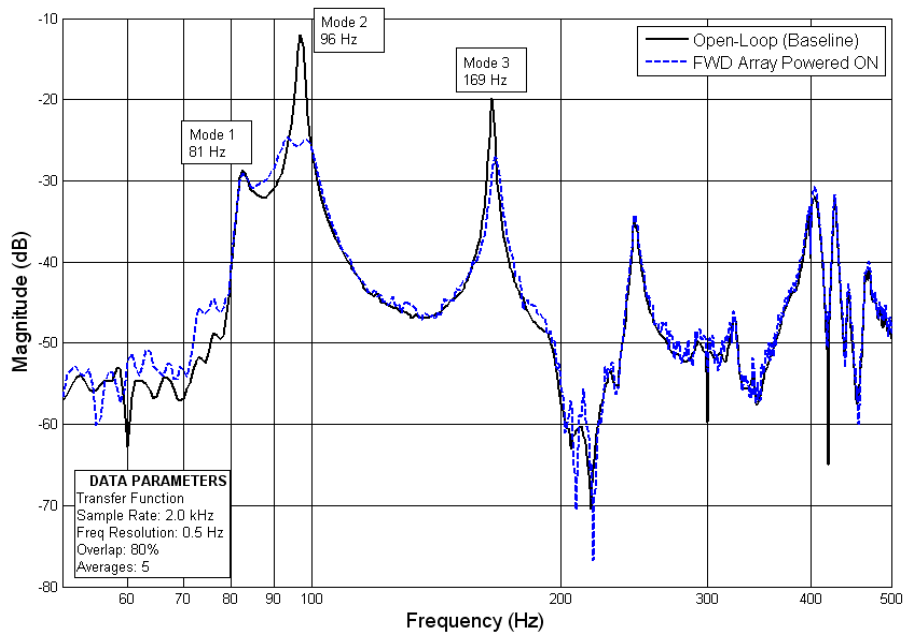


Figure 5.9: Forward Array Closed-Loop Response, Ground Testing

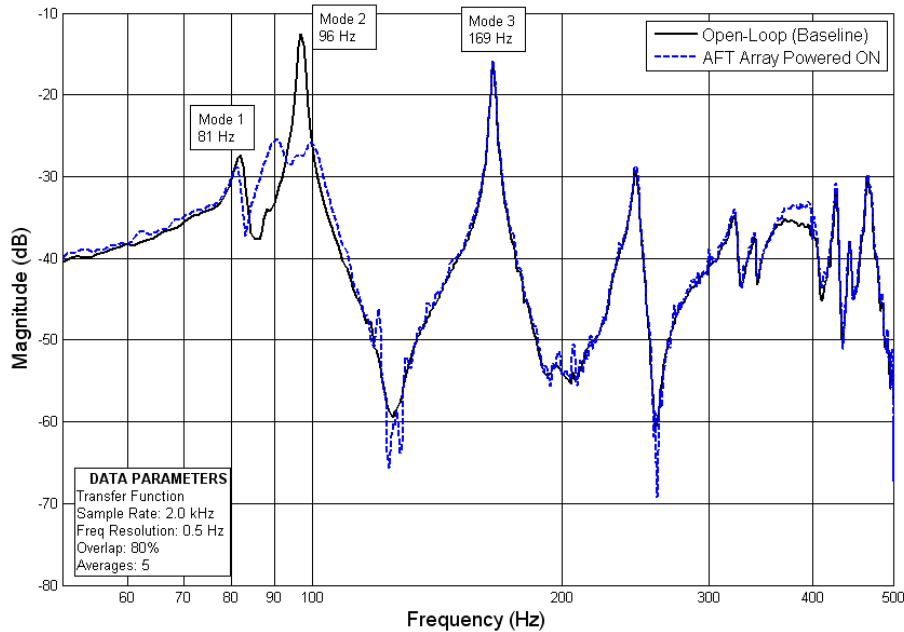


Figure 5.10: Aft Array Closed-Loop Response, Ground Testing

5.3 ACTIVE FIN Flight Testing

Flight testing occurred in two phases. Open-loop data gathered during Phase 1 was used to characterize the frequency response of the ventral fin and to determine the flight conditions where sufficient levels of vibration existed to allow for a conclusive demonstration of the effect of closed-loop control. Four important findings surfaced from Phase 1 flight testing. First, the modal frequencies of the ventral fin matched closely with those from previous tests of the same ventral fin, as shown in Table 5.3. Also, frequency measurements exhibited no statistical differences from changes in flight condition [4], showing that the test fin had not been damaged or structurally compromised since HAVE PUFF flight testing in 2005.

The next finding confirmed that the highest buffet levels occurred at high dynamic pressure (low altitudes), between 0.90 and 0.95 Mach, and at low angles of attack (level flight) [4]. Therefore, flight testing during Phase 2 was focused at high dynamic pressures, low angles of attack, and transonic speeds according to the test matrix (Figure 4.24).

Table 5.3: Ventral Fin Natural Frequency Comparison [4]

Data Source		Mode 1	Mode 2	Mode 3	Mode 4
HAVE PUFF [34]		78	95	167	232
ACTIVE FIN ¹	<i>Mean</i>	80.4	94.0	162.5	236.4
	<i>Standard Deviation</i>	1.3	1.8	2.3	3.8
	<i>95% Confidence Interval²</i>	±0.36	±0.51	±0.60	±0.98

Note: data in Hertz

¹ Open-loop data; Cruise and PA configuration; 1.0 to 5.0 load factor, 5k to 20k pressure altitude

² 95% confidence interval for the population mean with sample size = 57

The third finding involved the piezoelectric sensor signal levels from the primary sensors on the ventral fin. Fin vibration was not expected to exceed a magnitude that produced 50 volts peak-to-peak in the sensor output. Sensor signal attenuation circuits housed in the amplifier assembly were designed around this expected signal level. This assumption was based on laboratory measurements of sensor signal level versus ventral fin tip deflections when the fin was excited at the mode 2 frequency driven with an output voltage from the amplifier of 220 volts. The resulting ventral fin tip deflections were subjectively considered dangerous to exceed; thus, it was assumed such a level would not be exceeded in flight. Unfortunately, there was no data from previous testing to support or verify this assumption. Figure 5.11 illustrates the difference between sensor voltage during ground and flight testing. Recall that ventral fin excitation was accomplished by driving one of the actuator arrays with a swept sine wave input designed not to exceed the previously determined 50 volt peak-to-peak. Nevertheless, fin vibrations produced sensor outputs as much as 80 volts peak-to-peak during the highest levels of buffet encountered. As a consequence, additional attenuation was added to the primary sensor signals prior to Phase 2 flight testing by installing series connected resistors to the sensor signal inputs. Note that subsequent ground testing and Phase 2 flight testing was conducted with the inboard sensor attenuation level set at 11:1.

The final finding from Phase 1 flight testing involved an unexpected increase in the mode 2 response relative to other mods while the test aircraft was in the powered-approach (PA) configuration (landing gear extended) during an approach-to-landing.

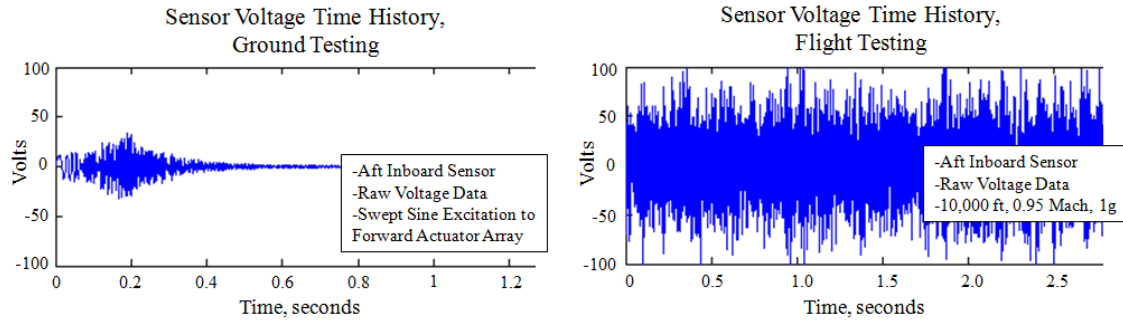


Figure 5.11: Sensor Voltage Level Comparison

Although the relative vibration magnitude, as measured by sensor RMS voltage, was 40 percent lower at approach speed (0.5 Mach, 250 KCAS), turbulent air shed from the landing gear caused a significant increase in the mode 2 response of the fin relative to vibration at other frequencies. To exploit the increase in mode 2 vibration, additional test points were planned and flown in the PA configuration giving the test matrix two categories: transonic (0.77 to 1.05 Mach) in the cruise configuration and PA test points.

Phase 2 flight testing compared the frequency response of the ventral fin during four cases: open-loop (baseline), forward array active, aft array active, and both arrays active simultaneously. Specific flight conditions targeted during Phase 2 included those conditions discovered during Phase 1 that resulted in the highest level of buffet response in the first 3 modes, specifically, powered approach test points and cruise test points near 0.95 Mach, low altitude, and 1g level flight. Very little change in peak magnitude was measured between the open and closed-loop responses during test points in the transonic region. Figure 5.12 shows the frequency response of the four test cases estimated from a data sample at 10,000 feet pressure altitude, 0.90 Mach, and 1g level flight. Although a slight change (1 dB) in the mode 1, 2, and 3 peak magnitudes occurred in the data sample, such a small deviation from the open-loop response was considered insignificant. The same indeterminate effect was concluded throughout the transonic test points, illustrated in Figure 5.13 showing data at 10,000 feet pressure altitude and 1g level flight.

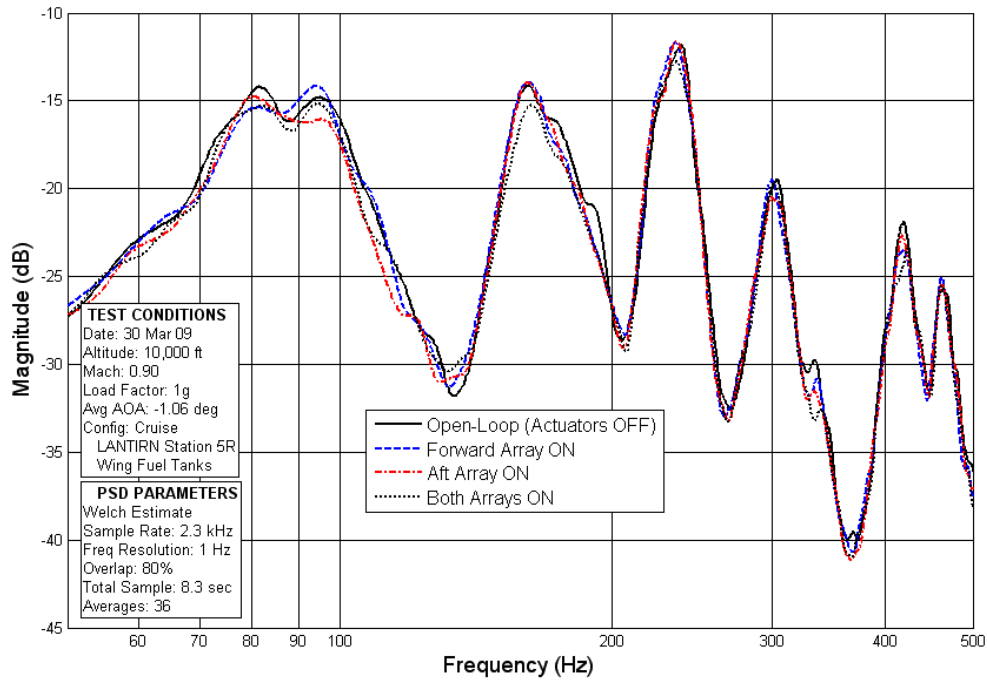


Figure 5.12: Flight Test Frequency Response, 10,000 feet Pressure Altitude, 0.90 Mach [4]

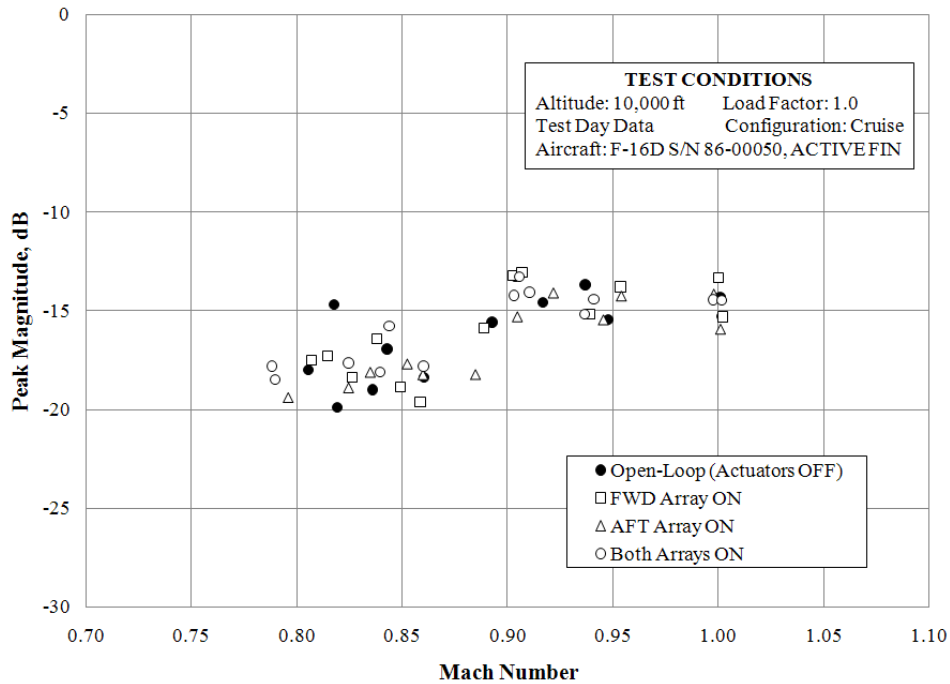


Figure 5.13: Flight Test Mode 2 Peak Magnitude Response, 10,000 feet Pressure Altitude, Transonic [4]

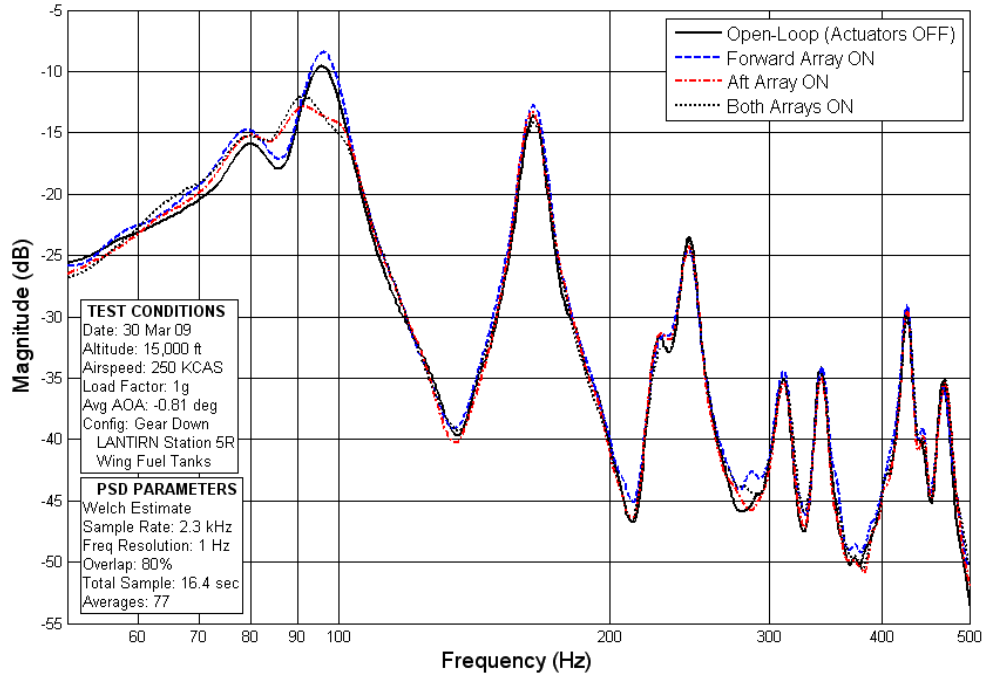


Figure 5.14: Flight Test Frequency Response, Powered Approach Configuration, 15,000 feet Pressure Altitude [4]

Test points in the PA configuration proved more successful. Figure 5.14 shows a 4 dB reduction in the mode 2 peak magnitude with the aft array powered on. Modes 1 and 3, unexpectedly, were not affected by the forward array.

The unanticipated high levels of vibration in the ventral fin seen during flight testing could have affected performance more so than anticipated. Closer inspection of amplifier output voltage for low speed, powered approach test points indicated that the amplifiers were driving the actuators near maximum capacity of 425 volts peak-to-peak, as shown in Figure 5.15. During transonic test points, like the sample shown in Figure 5.16 for 7,500 feet, 0.95 Mach, and 1g level flight, the amplifier output was saturated. This suggests that the actuators required higher drive voltages to achieve the level of control requested in the feedback loop. When the voltage signal recorded from the aft array outboard sensor from the data sample in Figure 5.16 was used in a simulation measuring the amplifier output voltage according the amplifier's transfer function, the control algorithm was calling for as much as 1900 volts peak-to-peak

drive voltage from the amplifier, as indicated in Figure 5.17. The actuators installed on the fin were limited to ± 500 volts, therefore, design factors such as actuator sizing or layering and sensor location or type may require reconsideration for better system performance. For example, actuator arrays of smaller surface area that contain more layers [20, 38] could, when located and oriented correctly, impart more strain in the areas of maximum strain energy.

The use of self-sensing actuators [23, 39, 46] would provide a true collocated design improving stability characteristics potentially allowing for higher feedback gains. Different sensor/control configurations such as acceleration feedback using accelerometers may improve the detectability of certain vibration modes aiding closed-loop algorithms.

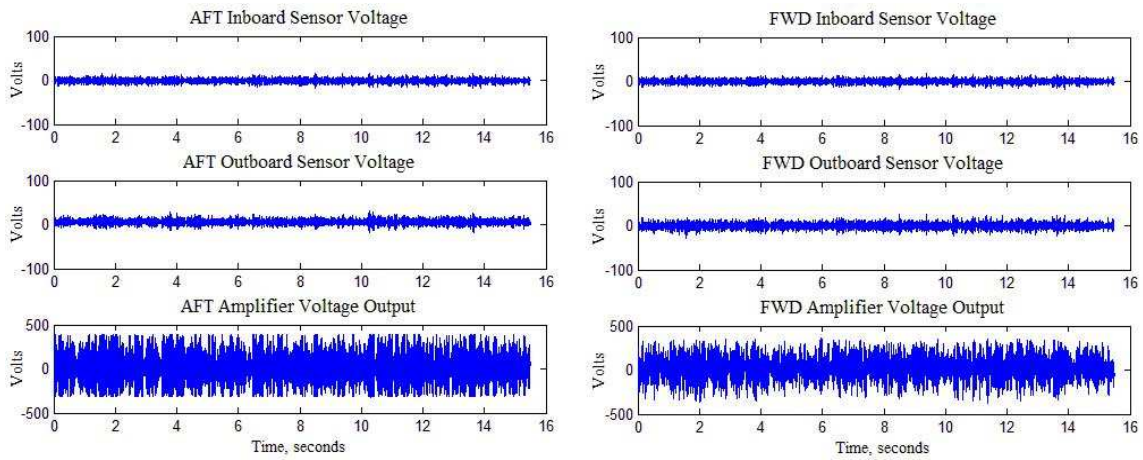


Figure 5.15: Sensor and Amplifier Output Voltage, Flight Test, 15,000 feet, 0.30 Mach, 1g Level Flight, Powered Approach

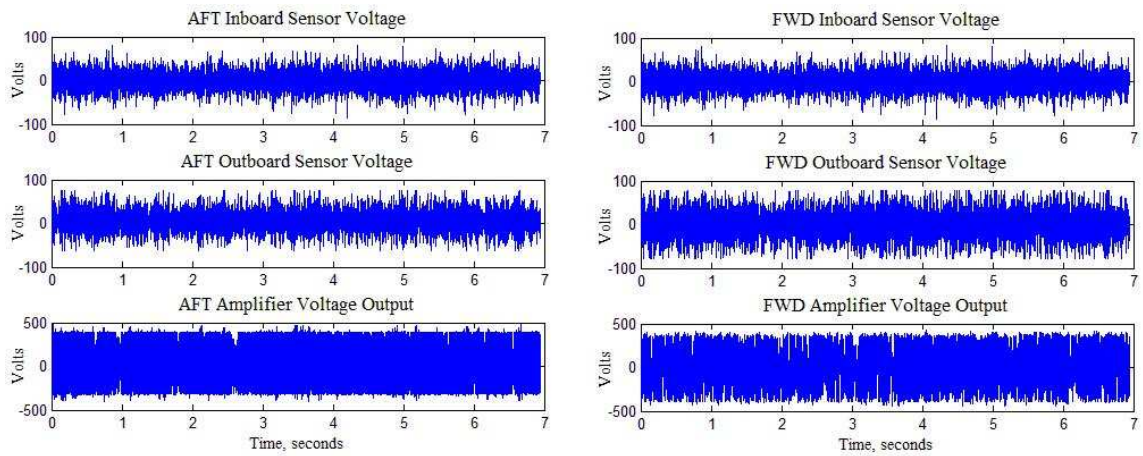


Figure 5.16: Sensor and Amplifier Output Voltage, Flight Test, 7,500 feet, 0.95 Mach, 1g Level Flight

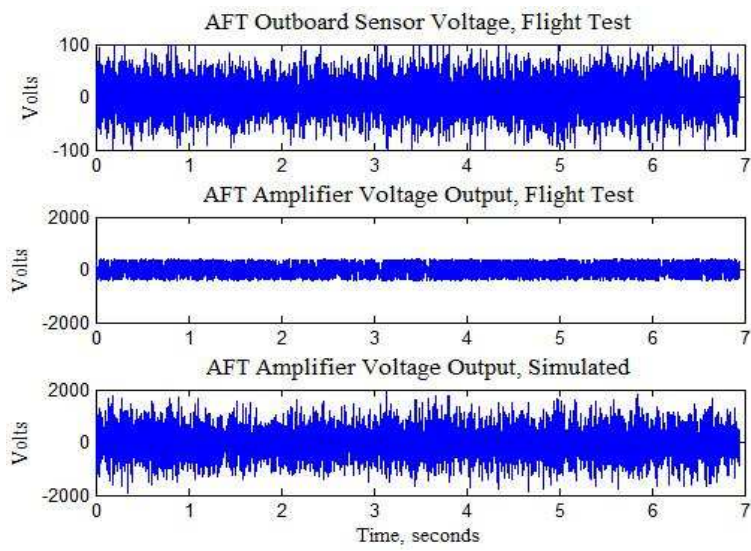


Figure 5.17: Amplifier Output Simulation Using Flight Test Sensor Input (7,500 feet, 0.95 Mach, 1g Level Flight) and Amplifier Transfer Function Model (Figure 4.10)

VI. Summary and Conclusions

The overall objective of the research presented in this thesis was to develop an autonomous active control system using collocated piezoelectric actuators and sensors to alleviate the buffet response of the first and second vibration modes of an F-16 Block 15 ventral fin during ground and flight tests. It is important to note that this research was not addressing the failure of Block 15 ventral fins, but took advantage of the susceptibility of Block 15 ventral fins to aerodynamic buffet in order to evaluate the effectiveness of closed-loop control of piezoelectric actuators. The steps accomplished to meet that objective resulted in the successful development of a buffet alleviation system including design and installation of piezoelectric actuators and sensors, construction of a custom drive amplifier, and optimization of two separate digital control techniques. Ground and flight testing demonstrated the effective, albeit to a lesser degree than desired, alleviation of buffet vibrations of the ventral fin during selected flight conditions. The results and conclusions of this research lay the foundation for further study and optimization of a piezoelectric buffet alleviation system for aerodynamic structures.

6.1 Summary

Piezoelectric actuators and sensors were designed according to recommendations made by Morgenstern [7] to alleviate buffet vibrations in the first and second modes of the ventral fin. To maximize effectiveness, the actuators were located on the fin surface in areas of maximum strain energy and oriented with their actuation fibers aligned with the direction of principle strain. The principle strain magnitudes and directions of the first four modes of the ventral fin were experimentally determined using a laser vibrometer and a central difference calculation prior to piezoelectric hardware installation. The area of maximum strain energy for mode 1 and mode 2 was located on the aft and forward sections of the ventral fin, respectively, and six total piezoelectric actuators, or patches, were placed in arrays in those areas to control each mode. Each array included three patches on the inboard side of the fin

and three on the outboard side. The center patch on each side of each array included an embedded piezoelectric sensor to provide collocated feedback for the closed-loop control system.

The hardware used in this research, aside from the Block 15 ventral fin and piezoelectric hardware, included a custom drive amplifier and the National Instruments Inc. Compact RIO digital controller. The control algorithms were implemented in the digital controller, which also served to control overall system function, using a finite difference formulation. The custom amplifier needed to drive the piezoelectric actuators on the ventral fin used a switch-mode topology because of its ability to recover stored energy during subsequent load discharges when driving the primarily reactive load of piezoelectric actuators. Two separate amplifiers were constructed to drive each actuator array independently. The amplifier electronics, designed to operate on an F-16 aircraft during flight testing, also housed signal conditioning circuits comprised of analog butterworth filters for the piezoelectric sensor signals.

Due to the non-linear effects of aerodynamic buffet, it was important for accurate frequency response measurement and modal parameter estimation throughout the testing effort. Control algorithm design required accurate system models and modal information. The Eigenstructure realization algorithm provided an efficient means of constructing state-space models that were easily implemented in control development and closed-loop stability assessments. During flight testing, the Welch frequency response estimation method was employed to generate power spectra and assess open and closed-loop performance.

Two control techniques were employed in this research: positive position feedback and Linear Quadratic Gaussian compensators. Positive position feedback algorithms, essentially second-order filter elements that act to increase damping at the targeted structural mode, were specified by filter frequency, filter damping ratio, and a scalar gain. Several PPF filters could be placed in parallel to control multiple modes simultaneously. The selection of filter characteristics, however, proved difficult and

depended heavily on the structural dynamics of the ventral fin. The final PPF design included a single filter element targeting mode 2 in the aft piezoelectric array and three filters in parallel configured to target modes 1, 2, and 3 in the forward array. Linear Quadratic Gaussian compensator designs, though less intuitive, proved easier to optimize due to its associated stability guarantees and its nature of balancing performance and control effort while accounting for process and measurement noise. The LQG compensators developed for each array were designed to target the first three modes of vibration which were within the bandwidth of the amplifiers. LQG compensators were not evaluated, however, with the Compact RIO digital control due to a limitation in programming an 8th order finite difference formulation. The LQG designs were optimized during bench testing using a non-flight worthy digital controller, but were not ground or flight tested.

Each control algorithm was optimized and evaluated during laboratory bench testing using all system hardware, ground testing with the hardware installed on the test aircraft, and flight testing at Edwards AFB as part of the ACTIVE FIN test project at Test Pilot School. The test aircraft was configured with a LANTIRN pod on station 5R directly upstream of the ventral fin in order to produce the desired level of buffet. The vibration in modes 1, 2, and 3 were successfully attenuated as much as 15 dB during bench and ground testing. However, only mode 2, attenuated 4 dB during the powered-approach test points, was affected during flight testing. Table 6.1 summarizes the results of testing.

Table 6.1: Summary of Test Results

Test	Positive Position Feedback			Linear Quadratic Gaussian ¹		
	Mode 1	Mode 2	Mode 3	Mode 1	Mode 2	Mode 3
Lab Bench Testing	15	14	18	4	15	11
Ground Testing [4]	0	14	8	-	-	-
Flight Testing [4]	0	4	0	-	-	-

¹LQG algorithms were not ground or flight tested due to a limitation in the digital controller

Several key findings were revealed during flight testing. First, with the test aircraft configured with a LANTIRN pod, the highest level of mean vibration in the ventral fin occurred at high dynamic pressure (low altitude), between 0.90 and 0.95 Mach, and a low angles of attack (level flight). Second, while in the powered-approach configuration (landing gear down) and at approach speeds (200-250 KCAS), the response of the second vibration mode increased relative to other frequencies despite lower mean vibration in the fin. Test points in the PA configuration were added to the test matrix and provided the best results of vibration attenuation during flight. Finally, fin vibration during all test points was much higher than expected. Due to this, the amplifier output was saturated during most test points suggesting that the actuators required higher drive voltages than available from the amplifier to achieve the level of control requested in the feedback loop. Further study is required to evaluate design factors such as actuator size and layering, sensor location and type, and amplifier design before efforts to improve the buffet alleviation system can begin.

6.2 Recommendations

The following recommendations are presented, in priority order, for future research concerning a buffet alleviation system for the Block 15 F-16 ventral fin.

1. Calculate the observability/controllability of the first four modes for the existing instrumentation configuration in order to assess the capability of the existing system and to highlight options for improvement.
2. Investigate the benefits/drawbacks of implementing acceleration feedback control for alleviating buffet vibrations in the ventral using the existing or modified piezoelectric actuator configuration. Accelerometers mounted near the tip of the ventral fin could potentially provide improved detectability of the first two modes.
3. Characterize the relationship between piezoelectric sensor voltage, fin displacement, and actual strain in the ventral fin to provide a baseline for future testing.

4. Define the optimal design of piezoelectric actuators in targeting specific modes of the ventral fin which may require actuators of different thickness or surface area or use an array with layered actuators in order to generate sufficient strain in the structure for a given drive voltage. Additional design effort could also lead to a configuration that is capable of employing the entire voltage range of the current MFC actuators (-500 to +1500 volts versus ± 500 volts). [2, 50]
5. Evaluate robust control techniques, like Linear Quadratic Gaussian compensators, during flight testing, which may require the use of different digital control hardware.
6. Investigate the improvements to the existing ‘Class D’ drive amplifier. There exists many ways to implement a ‘Class D’ switching topology in hardware. The method employed in this research may have not been the most optimal given the overall system design.
7. Investigate and potential benefits/drawbacks of a ‘Class AB’ (analog) amplifier topology as the piezoelectric drive amplifier. Because a ‘Class D’ amplifier, like that used in this research, is designed for a specific capacitive load and bandwidth, it is inherently inflexible and, due to its switching characteristics, generates high frequency noise which could influence performance and interfere with other system components. A ‘Class AB’ amplifier is more flexible in terms of applicable load and does not generate as much circuit noise. Theoretically, a ‘Class AB’ amplifier is less efficient than a ‘Class D’; but its uses should be explored in future work.
8. Investigate the feasibility of self-sensing piezoelectric actuators for true collocated control. [23, 39, 46]
9. Investigate the application of adaptive control algorithms for real-time stability verification and gain scheduling to combat the non-linear effects of aerodynamic buffet.

10. Investigate the benefits/drawbacks of modifications to the existing signal conditioning (band-pass filter) including a cut-off frequency closer to the desired Nyquist frequency.

Bibliography

1. Agnes, Gregory S., Stephen R. Whitehouse, and John R. Mackaman. “Vibration Attenuation of Aircraft Structures Utilizing Active Materials”. *Smart Structures and Intelligent System*, SPIE Vol. 1917:368–379, 1993.
2. Aldraihem, Osama J. et al. “Optimal Size and Location of Piezoelectric Actuator/Sensors: Practical Considerations”. *Journal of Guidance, Control, and Dynamics*, 23(3):509–515, May 2000.
3. Brennan, Matthew C. and Anna-Maria Rivas McGowan. *Piezoelectric Power Requirements for Active Vibration Control*. Technical report, NASA Langley Research Center, Hampton, VA, 1997.
4. Browning, J., S.Y. Teo, C. Buckley, C. Seager, and L. Haubelt. *ACTIVE FIN: F-16 Ventral Fin Buffet Alleviation Using Piezoelectric Actuators*. Technical Information Memorandum AFFTC-TIM-09-06, Air Force Flight Test Center, Edwards AFB, CA 93524, June 2009.
5. Burl, Jeffery B. *Linear Optimal Control*. Addison Wesley Longman, Inc., 1999.
6. Burnham, J. K., D. M. Pitt., E. V. White, D. A. Henderson, and R. W. Moses. “An Advanced Buffet Load Alleviation System”. *42nd AIAA/ASME/ASCE/AHS/ASC Structures, Structural Dynamics, and Materials Conference and Exhibit, Seattle, WA*, (AIAA-2001-1666), April 16-19 2001.
7. Canfield, Robert A., Shawn D. Morgenstern, and Donald L. Kunz. “Alleviation of Buffet-Induced Vibration using Piezoelectric Actuators”. *Computers and Structures*, 86:281–291, 2008.
8. Chaudhry, Zaffir A., T. Joseph, Fanping P. Sun, and Craig A. Rogers. “Local-Area Health Monitoring of Aircraft Via Piezoelectric Actuator/Sensor Patches”. *Smart Structures and Materials: Smart Structures and Integrated Systems*, Proc. of SPIE Vol. 2443:268–276, May 1995.
9. Chen, Yong, W. Viresh, and David Zimcik. “Development and Verification of Real-Time Controllers for F/A-18 Vertical Fin Buffet Load Alleviation”. Yuji Matsuzaki (editor), *Smart Structures and Materials*, volume Proc. of SPIE Vol. 6173. National Research Council of Canada, Ottawa, ON CANADA K1A 0R6, 2006.
10. Clingman, Dan J. and Mike Gamble. “High Voltage Switching Piezo Drive Amplifier”. *SPIE conference on industrial and Commercial Applications of Smart Structures Technologies, Newport Beach, CA*, SPIE Volume 3674:280–286, March 1999.

11. Cobb, Richard. "State-Space Model Identification Using the Eigensystem Realization Algorithm Toolbox for MATLABTM". Software User Interface, Nov 2003. Version 1.1.
12. Connolly, A. J., M. Green, J. F. Chicharo, and R. R. Bitmead. "The Design of LQG & H(infinity) Controllers for use in Active Vibration Control & Narrow Band Disturbance Rejection". *Proc. of the 34th Conference on Decision and Control, New Orleans, LA*, 2982–2987, December 1995.
13. Culshaw, Brian. *Smart Structures and Materials*. Artech House, Inc., 685 Canton Street, Norwood, MA 02062, 1996.
14. Cunningham, Atlee M. *Buzz, Buffet and LCO on Military Aircraft - The Aeroelastician's Nightmare*. Technical report, Lockheed Martin Aeronautics Company, Fort Worth, TX, 2003.
15. Daue, Thomas. "Smart-Material Inc., Macro Fiber Composites". Electronic Message, December 2007. Transmitted to Joseph Browning.
16. Dosch, J. J., D. J. Inman, and E. Garcia. "A Self-Sensing Piezoelectric Actuator for Collocated Control". *Journal of Intelligent Material System and Structure*, Vol. 3:166–185, January 1992.
17. Enriquez, Reynaldo F. and Gregory J. Burgess. *Aeroelastic Load Control Initial Phase I Flight Test Report*. Technical Information Memorandum AFFTC-TIM-05-05, Air Force Flight Test Center, Edwards AFB, CA 93524, October 2005.
18. Falangas, Eric T. et al. *Piezoceramic Actuator Active Vibration Suppression System B-1B Flight Demonstration Program*. Technical Report AFRL-VA-WP-TR-1999-3011, Air Vehicles Directorate, Air Force Research Laboratory, AFMC, Wright-Patterson AFB, Ohio, January 1998.
19. Fanson, J.L. and T.K. Caughey. "Positive Position Feedback Control for Large Space Structures". *AIAA*, 28(4):717–724, 1990.
20. Galea, Stephen C., Douglas A. Henderson, Robert W. Moses, Edward V. White, and David G. Zimcik. "Next Generation Active Buffet Supression System". *AIAA/ICAS International Air and Space Symposium and Exposition*. Dayton, Ohio, 14-17 July 2003.
21. Goh, C. J. and T. K. Caughey. "On the Stability Problem Caused by Finite Actuator Dynamics in the Collocated Control of Large Space Structures". *International Journal of Control*, Vol. 41(No. 3):787–802, 1985.
22. Hanagud, Sathyanaraya. *F-15 Tail Buffet Alleviation: A Smart Structures Approach*. Technical report, School of Aerospace Engineering, Georgia Institute of Technology, Atlanta, GA 30332, December 1998.
23. Hongsheng, Hu and Qian Suxiang. "Self-sensing Piezoelectric Actuator for Active Vibration Control Based on Adaptive Filter". 2564–2569. IEEE International Conference on Mechatronics and Automation, Harbin, China, August 2007.

24. Inman, Daniel J. *Vibration With Control*. John Wiley & Sons Ltd., The Atrium, Southern Gate, Chichester, West Sussex PO19 8SQ, England, 2006.
25. Institute of Electrical and Electronics Engineers, Inc Standards Association, New York City, New York. *ANSI/IEEE Standard 176-1987, IEEE Standard on Piezoelectricity*, 2004.
26. Juang, J. N. and R. S. Pappa. "An Eigensystem Realization Alogrithm for Modal Parameter Identification and Model Reduction". *Journal of Guidance, Control, and Dynamics*, 8(5):620–627, 1985.
27. Juang, J. N. and R. S. Pappa. "Effects of Noise on Modal Parameters Identified by the Eigensystem Realizationonn Algorithm". *Journal of Guidance, Control, and Dynamics*, 9(3):294–303, 1986.
28. Kondoh, S., C. Yatomi, and K. Inoue. "The Positioning of Sensors and Actuators in the Vibration Control of Flexible Structures". *JSME International Journal Series III*, Vol. 33:175–181, 1990.
29. Lazarus, K. B., E. Saarmaa, and G. S. Agnes. "An Active Smart Material System for Buffet Load Alleviation". *SPIE's 2nd Annual International Symposium on Smart Structures and Materials*, Vol. 2447:179–192, 1995.
30. Leo, Donald J. "Energy Analysis of Piezoelectric-Actuated Structures Drive by Linear Amplifiers". *Journal of Intelligent Material Systems and Structures*, Vol. 10:36–45, January 1999.
31. Lindner, D. K. and S. Chandrasekaran. "Power Flow Through Controlled Piezoelectric Actuators". *Journal of Intelligent Material Systems and Structures*, (JIMSS-00-033), October 2000. Revised.
32. Lindner, D. K., N. Vujic, and D. J. Leo. "Comparison of Linear and Switching Drive Amplifiers for Piezoelectric Actuators". *43rd AIAA/ASME/ASCE/AH-S/ASC Structures, Structural Dynamics, and Materials Conference, Denver CO*, (AIAA-2002-1352):1–10, April 2002.
33. Luan, Jiyuan and Fred C. Lee. "Design of a High Frequency Switching Amplifier for Smart Material Actuators with Improved Current Mode Control". *IEEE*, Volume 1:59–64, May 1998.
34. Morgenstern, Shawn D., Aaron A. Tucker, Heather C. Giebner, Aniello Violetti, and Dick Wong. *Limited Characterization of Dual Bimorph Synthetic Jet Actuators: Aeroelastic Load Control - Phase I, Project HAVE PUFF*. Technical Information Memorandum AFFTC-TIM-05-07, Air Force Flight Test Center, Edwards AFB, CA 93524, December 2005.
35. Moses, Robert W. *Active Vertical Tail Buffeting Alleviation on a Twin-Tail Figther Configuration in a Wind Tunnel*. Conference paper, Aeroelasticity Branch, NASA Langley Research Center, Hampton, VA 23681, 1997.

36. Moses, Robert W. *NASA Langley Research Center's Contributions to International Active Buffet Alleviation Programs*. Technical report, Aeroelasticity Branch, NASA Langley Research Center, Hampton, VA, 1999.
37. Nyquist, Henry. "Regeneration Theory". *Bell System Technical Journal*, 11:126–147, 1932.
38. Pitt, Dale M., Michael J. Thomas, and Salvatore L. Liquore. *Air Vehicles Technology Integration Program (AVTIP), Delivery Order 0025: Active Buffet Load Alleviation System Ground Test*. Technical Report AFRL-VA-WP-TR-2006-3005, Air Vehicles Directorate, Air Force Research Laboratory, AFMC, Wright-Patterson AFB, Ohio, September 2005.
39. Pourboghraat, Farzad et al. "Vibration Control of Flexible Structures using Self-Sensing Actuators". *SPIE Conference on Smart Structures and Integrated Systems*, volume SPIE Vol. 3668. Newport Beach, California, March 1999.
40. Preumont, Andre. *Vibration Control of Active Structures*. Kluwer Academic Publishers, 2nd edition, 2002.
41. Reid, J. Gary. *Linear System Fundamentals*. McGraw Hill Book Company, 1983.
42. Rew, Keun-Ho, Jae-Hung Han, and In Lee. "Adaptive Multi-Modal Vibration Control of Wing-Like Composite Structures Using Adaptive Positive Position Feedback". *AIAA*, April 2000.
43. Robert W. Moses, Aroan A. Bent Alessandro E. Pizzochero, Carol D. Wieseman. "Evaluation of New Actuators in a Buffet Loads Environment". *Smart Structures and Materials, 2001: Industrial and Commercial Applications of Smart Structures Technologies*, Proceedings of SPIE Vol 4332:10–21, 2001.
44. Schultz, G. and G. Hiembold. "Dislocated Actuator/Sensor Positioning and Feedback Design for Flexible Structures". *Journal of Guidance*, Vol. 6:361–367, 1983.
45. Sheta, Essam F. et al. *An Active Smart Material Control System for F/A-18 Buffet Alleviation*. Technical report, International Forum on Aeroelasticity and Structural Dynamics, Amsterdam, Netherlands, June 2003.
46. Simmers, G.E. et al. "Improved Piezoelectric Self-Sensing Actuation". *Journal of Intelligent Material Systems and Structures*, 15(12):941–953, December 2004.
47. Smart-Material, Inc. "Commercial Literature". Website: <http://www.smart-material.com>, April 2008.
48. Sodano, Henry A., Gyuahae Park, and Daniel J. Inman. "An Investigation into the Performance of Macro-Fiber Composites for Sensing and Structural Vibration Applications". *Mechanical Systems and Signal Processing*, Vol. 18:683–697, 2004.
49. Song, G., S.P. Schmidt, and B.N. Agrawal. "Experimental Robustness Study of Positive Position Feedback Control for Active Vibration Suppression". *Journal of Guidance and Control*, 25(1):179–182, 2001.

50. Steffan, V. and D.J. Inman. “Optimal Design of Piezoelectric Materials for Vibration Damping in Mechanical Systems”. *Journal of Intelligent Material Systems and Structures*, 10(12):945–955, 1999.
51. van Tongeren, J.H., C.J. Lof, J.J. Meijer, and E.G.M. Geurts. *F-16 Ventral Fins Analysis*. Technical Report NLR-CR-99366, National Aerospace Laboratory, Amsterdam, The Netherlands, August 1999.
52. United States Patent 5, 752, 264. “Amplifier for Driving Large Capacitive Loads”, November 23 1993.
53. Warkentin, David J. and Edward F. Crawley. “Power Flow and Amplifier Design for Piezoelectric Actuators in Intelligent Structures”. SPIE Vol. 2190:283–294, 1994.
54. ZONA Technology, Inc. *ZAERO Theoretical Manual, Version 7.1*. ZONA Technology, Inc., Scottsdale, AZ 85251, September 2004.

Vita

Captain Joseph S. Browning was born in Stuttgart, Arkansas graduating from Stuttgart High School in 1998. He attended the United States Air Force Academy where he graduated with distinction earning a Bachelor of Science degree in Mechanical Engineering.

Following his commission from the Air Force Academy as a 2nd Lieutenant in the United States Air Force, Captain Browning was assigned to the 36 Electronic Warfare Squadron, 53rd Wind, Eglin Air Force Base, Florida where he served as an operational test and evaluation engineer on the F-15E self-protection jammer and the B-2 defensive management system. In 2006, he was selected for the combined Air Force Institute of Technology/Test Pilot School program, and entered the Air Force Institute of Technology master's degree program. He graduated from the Test Pilot School in June of 2009 with a Master of Science in Flight Test Engineering. This thesis provides the final document required for him to earn his Master of Science Degree in Aeronautical Engineering from the Air Force Institute of Technology.

Permanent address: 2950 Hobson Way
Air Force Institute of Technology
Wright-Patterson AFB, OH 45433

REPORT DOCUMENTATION PAGE			<i>Form Approved</i> OMB No. 0704-0188	
The public reporting burden for this collection of information is estimated to average 1 hour per response, including the time for reviewing instructions, searching existing data sources, gathering and maintaining the data needed, and completing and reviewing the collection of information. Send comments regarding this burden estimate or any other aspect of this collection of information, including suggestions for reducing this burden to Department of Defense, Washington Headquarters Services, Directorate for Information Operations and Reports (0704-0188), 1215 Jefferson Davis Highway, Suite 1204, Arlington, VA 22202-4302. Respondents should be aware that notwithstanding any other provision of law, no person shall be subject to any penalty for failing to comply with a collection of information if it does not display a currently valid OMB control number. PLEASE DO NOT RETURN YOUR FORM TO THE ABOVE ADDRESS.				
1. REPORT DATE (DD-MM-YYYY) 04-09-2009		2. REPORT TYPE Master's Thesis		3. DATES COVERED (From — To) 1 Jan 07 – 4 Sep 09
4. TITLE AND SUBTITLE F-16 Ventral Fin Buffet Alleviation Using Piezoelectric Actuators			5a. CONTRACT NUMBER	
			5b. GRANT NUMBER	
			5c. PROGRAM ELEMENT NUMBER	
6. AUTHOR(S) Capt Joseph S Browning			5d. PROJECT NUMBER	
			5e. TASK NUMBER	
			5f. WORK UNIT NUMBER	
7. PERFORMING ORGANIZATION NAME(S) AND ADDRESS(ES) Air Force Institute of Technology Graduate School of Engineering and Management (AFIT/ENY) 2950 Hobson Way WPAFB OH 45433-7765			8. PERFORMING ORGANIZATION REPORT NUMBER AFIT/GAE/ENY-09-S01	
9. SPONSORING / MONITORING AGENCY NAME(S) AND ADDRESS(ES) USAF Test Pilot School LtCol Timothy Jorris (661-277-3000) 1220 South Wolfe Ave Edwards AFB, CA 93524			10. SPONSOR/MONITOR'S ACRONYM(S) TPS	
			11. SPONSOR/MONITOR'S REPORT NUMBER(S)	
12. DISTRIBUTION / AVAILABILITY STATEMENT APPROVED FOR PUBLIC RELEASE; DISTRIBUTION UNLIMITED				
13. SUPPLEMENTARY NOTES				
14. ABSTRACT Buffet-induced vibrations can have a disastrous impact on aircraft structures. Early attempts at combating buffet vibrations included passive methods such as structural enhancements and leading edge fences. Active methods have shown greater promise, including active airflow control, control surface modulation, and active structural control using piezoelectric actuators. Surface mounted piezoelectric actuators impart directional strain reducing the negative effects associated with harmful vibration. The Block-15 F-16 ventral fin represents an aircraft structure prone to failure when subjected to the buffet field from the wake of a LANTIRN pod. This research takes advantage of the susceptibility to buffet vibration of the Block 15 ventral fin in an effort to design an active control system to alleviate vibrations using piezoelectric actuators and sensors and to demonstrate its capability during flight test. It was sponsored by the United States Air Force (USAF) Test Pilot School (TPS). The development of an active control system began with the specification of piezoelectric actuators and sensors to be used in a collocated design to alleviate the vibrations of the first two modes of the ventral fin. A switching amplifier was designed and built to drive the actuators during all phases of testing. For the piezoelectric actuators to be effective, they needed to be located within the regions of highest strain energy and aligned with the principal strain vectors in those regions, the direction of principle strain was experimentally determined to ensure the proper orientation of the piezoelectric hardware on the ventral fin's surface. Two control techniques were used in this research: positive position feedback and Linear Quadratic Gaussian compensator. Both algorithms were developed and optimized during laboratory simulations and bench testing with system hardware where as much as 15 dB peak magnitude reduction was achieved in the ventral fin mode 1, 2, and 3 response. The positive position feedback algorithms were implemented during aircraft ground and flight testing at the USAF TPS, Edwards Air Force Base, California. Ground testing showed as much as 14 dB and 8 dB peak magnitude reduction in the mode 2 and mode 3 response, respectively. As much as 4 dB peak magnitude reduction was recorded in the mode 2 response during flight testing proving the potential of piezoelectric actuators in a buffet alleviation system. Still, there exists many design considerations, such as piezoelectric actuator and sensor configuration, that could lead to system improvement.				
15. SUBJECT TERMS Piezoelectric, buffet, F-16, ventral fin, active control, positive position feedback, linear quadratic Gaussian				
16. SECURITY CLASSIFICATION OF: UNCLASSIFIED		17. LIMITATION OF ABSTRACT UU	18. NUMBER OF PAGES 122	19a. NAME OF RESPONSIBLE PERSON Dr. Richard Cobb
a. REPORT U	b. ABSTRACT U	c. THIS PAGE U	19b. TELEPHONE NUMBER (Include Area Code) (937)255-3636, 4599	